



HAL
open science

Identification of the Top TESS Objects of Interest for Atmospheric Characterization of Transiting Exoplanets with JWST

Benjamin J. Hord, Eliza M. -R. Kempton, Thomas M. Evans-Soma, David W. Latham, David R. Ciardi, Diana Dragomir, Knicole D. Colón, Gabrielle Ross, Andrew Vanderburg, Zoe L. de Beurs, et al.

► To cite this version:

Benjamin J. Hord, Eliza M. -R. Kempton, Thomas M. Evans-Soma, David W. Latham, David R. Ciardi, et al.. Identification of the Top TESS Objects of Interest for Atmospheric Characterization of Transiting Exoplanets with JWST. *The Astronomical Journal*, 2024, 167, 10.3847/1538-3881/ad3068 . insu-04836870

HAL Id: insu-04836870

<https://insu.hal.science/insu-04836870v1>

Submitted on 13 Dec 2024

HAL is a multi-disciplinary open access archive for the deposit and dissemination of scientific research documents, whether they are published or not. The documents may come from teaching and research institutions in France or abroad, or from public or private research centers.

L'archive ouverte pluridisciplinaire **HAL**, est destinée au dépôt et à la diffusion de documents scientifiques de niveau recherche, publiés ou non, émanant des établissements d'enseignement et de recherche français ou étrangers, des laboratoires publics ou privés.



Distributed under a Creative Commons Attribution 4.0 International License



Identification of the Top TESS Objects of Interest for Atmospheric Characterization of Transiting Exoplanets with JWST

Benjamin J. Hord^{1,2,119} , Eliza M.-R. Kempton² , Evans-Soma Thomas M.^{3,4} , David W. Latham⁵ , David R. Ciardi⁶ ,
 Diana Dragomir⁷ , Knicole D. Colón^{1,8} , Gabrielle Ross⁹, Andrew Vanderburg¹⁰ , Zoe L. de Beurs^{10,120} ,
 Karen A. Collins⁵ , Cristilyn N. Watkins⁵ , Jacob Bean¹¹ , Nicolas B. Cowan¹² , Tansu Daylan¹³ , Caroline V. Morley¹⁴ ,
 Jegu Ih² , David Baker¹⁵ , Khalid Barkaoui^{10,16,17} , Natalie M. Batalha¹⁸ , Aida Behmar^{19,121} , Alexander Belinski²⁰ ,
 Zouhair Benkhaldoun²¹ , Paul Benni²² , Krzysztof Bernacki²³ , Allyson Bieryla⁵ , Avraham Binnenfeld²⁴ ,
 Pau Bosch-Cabot²⁵ , François Bouchy²⁶ , Valerio Bozza^{27,28} , Rafael Brahm^{29,30} , Lars A. Buchhave³¹ ,
 Michael Calkins^{5,32} , Ashley Chontos³³ , Catherine A. Clark^{6,34} , Ryan Cloutier³⁵ , Marion Cointepas^{26,36},
 Kevin I. Collins³⁷ , Dennis M. Conti³⁸ , Ian J. M. Crossfield³⁹ , Fei Dai⁴⁰ , Jerome P. de Leon⁴¹ , Georgina Dransfield⁴² ,
 Courtney Dressing⁴³ , Adam Dustor⁴⁴ , Gilbert Esquerdo⁵ , Phil Evans⁴⁵ , Sergio B. Fajardo-Acosta⁴⁶ , Jerzy Fiołka²³ ,
 Raquel Forés-Toribio^{47,48} , Antonio Frasca⁴⁹ , Akihiko Fukui^{50,51} , Benjamin Fulton⁵² , Elise Furlan⁵² , Tianjun Gan⁵³ ,
 Davide Gandolfi⁵⁴ , Mourad Ghachoui^{55,56}, Steven Giacalone⁴³ , Emily A. Gilbert³⁴ , Michaël Gillon¹⁶ , Eric Girardin⁵⁷ ,
 Erica Gonzales⁵⁸ , Ferran Grau Horta⁵⁹ , Joao Gregorio⁶⁰ , Michael Greklek-McKeon⁶¹ , Pere Guerra²⁵ ,
 J. D. Hartman⁶² , Coel Hellier⁶³, Ian Helm⁶⁴ , Krzysztof G. Helminiak⁶⁵ , Thomas Henning⁴ , Michelle L. Hill⁶⁶ ,
 Keith Horne⁶⁷ , Andrew W. Howard⁶⁸ , Steve B. Howell⁶⁹ , Daniel Huber³³ , Giovanni Isopi⁷⁰, Emmanuel Jehin⁷¹ ,
 Jon M. Jenkins⁶⁹ , Eric L. N. Jensen⁷² , Marshall C. Johnson⁷³ , Andrés Jordán^{29,30,74} , Stephen R. Kane⁶⁸ ,
 John F. Kielkopf⁷⁵ , Vadim Krushinsky⁷⁶ , Sławomir Lasota²³ , Elena Lee⁷² , Pablo Lewin⁷⁷ ,
 John H. Livingston^{78,79,80} , Jack Lubin⁸¹ , Michael B. Lund⁸² , Franco Mallia⁷⁰, Christopher R. Mann^{83,84} ,
 Giuseppi Marino^{85,86} , Nataliia Maslennikova^{20,87} , Bob Massey⁸⁸ , Rachel Matson⁸⁹ , Elisabeth Matthews⁴ ,
 Andrew W. Mayo^{90,91} , Tsevi Mazeh⁹², Kim K. McLeod⁹³ , Edward J. Michaels⁹⁴, Teo Močnik⁹⁵ , Mayuko Mori⁴¹ ,
 Georgia Mraz⁹⁶, Jose A. Muñoz⁴⁷ , Norio Narita^{50,51,78} , Krupa Natarajan⁶⁴, Louise Dyregaard Nielsen^{26,97} ,
 Hugh Osborn⁹⁸ , Enric Palle^{51,99}, Aviad Panahi⁹² , Riccardo Papini^{100,101}, Peter Plavchan⁶⁴ , Alex S. Polanski^{52,102,122} ,
 Adam Popowicz²³ , Francisco J. Pozuelos¹⁰³ , Samuel N. Quinn⁵ , Don J. Radford¹⁰⁴ , Phillip A. Reed¹⁰⁵ ,
 Howard M. Relles⁵ , Malena Rice¹⁰⁶ , Paul Robertson⁸¹ , Joseph E. Rodriguez¹⁰⁷ , Lee J. Rosenthal⁶⁸ ,
 Ryan A. Rubenzahl^{68,68} , Nicole Schanche^{1,2} , Joshua Schlieder¹ , Richard P. Schwarz⁵ , Ramotholo Sefako¹⁰⁸ ,
 Avi Shporer¹⁰⁹ , Alessandro Sozzetti¹¹⁰ , Gregor Srdoc¹¹¹, Chris Stockdale¹¹² , Alexander Tarasenkov⁸⁷ ,
 Thiam-Guan Tan^{113,114} , Mathilde Timmermans¹⁶, Eric B. Ting⁶⁹ , Judah Van Zandt¹¹⁵ , JP Vignes¹⁰¹ , Ian Waite¹¹⁶ ,
 Noriharu Watanabe⁴¹ , Lauren M. Weiss¹¹⁷ , Justin Wittrock³⁷ , George Zhou¹¹⁶ , Carl Ziegler¹¹⁸ , and Shay Zucker²⁴ 

¹ NASA Goddard Space Flight Center, 8800 Greenbelt Road, Greenbelt, MD 20771, USA; benjamin.j.hord@nasa.gov

² Department of Astronomy, University of Maryland, College Park, MD 20742, USA

³ School of Information and Physical Sciences, University of Newcastle, Callaghan, NSW 2308, Australia

⁴ Max Planck Institute for Astronomy, Königstuhl 17, D-69117 Heidelberg, Germany

⁵ Center for Astrophysics, Harvard & Smithsonian, 60 Garden Street, Cambridge, MA 02138, USA

⁶ NASA Exoplanet Science Institute, IPAC, California Institute of Technology, Pasadena, CA 91125, USA

⁷ Department of Physics and Astronomy, University of New Mexico, 210 Yale Boulevard NE, Albuquerque, NM 87106, USA

⁸ GSFC Sellers Exoplanet Environments Collaboration, USA

⁹ Princeton University, Princeton, NJ 08544, USA

¹⁰ Department of Earth, Atmospheric and Planetary Sciences, Massachusetts Institute of Technology, Cambridge, MA 02139, USA

¹¹ Department of Astronomy & Astrophysics, University of Chicago, 5640 S Ellis Avenue, Chicago, IL 60637, USA

¹² Department of Earth and Planetary Sciences and Department of Physics, McGill University, 3600 rue University, Montréal, QC, H3A 2T8, Canada

¹³ Department of Physics and McDonnell Center for the Space Sciences, Washington University, St. Louis, MO 63130, USA

¹⁴ Department of Astronomy, The University of Texas at Austin, 2515 Speedway, Stop C1400, Austin, TX 78712-1205, USA

¹⁵ Physics Department, Austin College, Sherman, TX 75090, USA

¹⁶ Astrobiology Research Unit, Université de Liège, 19C Allée du 6 Août, 4000 Liège, Belgium

¹⁷ Instituto de Astrofísica de Canarias (IAC), Calle Vía Láctea s/n, 38200, La Laguna, Tenerife, Spain

¹⁸ Department of Astronomy and Astrophysics, University of California, Santa Cruz, CA 95060, USA

¹⁹ Division of Geological and Planetary Science, California Institute of Technology, Pasadena, CA 91125, USA

²⁰ Sternberg Astronomical Institute, Lomonosov Moscow State University, Universitetskii prospekt, 13, Moscow 119992, Russia

²¹ Oukaimeden Observatory, High Energy Physics and Astrophysics Laboratory, Faculty of sciences Semlalia, Cadi Ayyad University, Marrakech, Morocco

²² Acton Sky Portal (private observatory), Acton, MA 01720, USA

²³ Department of Electronics, Electrical Engineering and Microelectronics, Silesian University of Technology, Akademicka 16, 44-100 Gliwice, Poland

²⁴ Porter School of the Environment and Earth Sciences, Tel Aviv University, Tel Aviv 6997801, Israel

²⁵ Observatori Astronòmic Albanyá, Camí de Bassegoda S/N, Albanyá 17733, Girona, Spain

²⁶ Observatoire de Genève, Département d'Astronomie, Université de Genève, Chemin Pegasi 51b, 1290 Versoix, Switzerland

²⁷ Dipartimento di Fisica "E.R. Caianiello," Università di Salerno, Via Giovanni Paolo II 132, 84084 Fisciano, Italy

²⁸ Istituto Nazionale di Fisica Nucleare, Sezione di Napoli, Via Cintia, 80126 Napoli, Italy

²⁹ Facultad de Ingeniería y Ciencias, Universidad Adolfo Ibáñez, Av. Diagonal las Torres 2640, Peñalolén, Santiago, Chile

³⁰ Millennium Institute for Astrophysics, Macul, Santiago, Chile

³¹ DTU Space, Technical University of Denmark, Elektrovej 328, DK-2800 Kgs. Lyngby, Denmark

³² Whipple Observatory, Amado, AZ 85645, USA

³³ Institute for Astronomy, University of Hawai'i, 2680 Woodlawn Drive, Honolulu, HI 96822, USA

³⁴ Jet Propulsion Laboratory, California Institute of Technology, Pasadena, CA 91109, USA

- ³⁵ Department of Physics & Astronomy, McMaster University, 1280 Main St W, Hamilton, ON, L8S 4L8, Canada
- ³⁶ Univ. Grenoble Alpes, CNRS, IPAG, F-38000 Grenoble, France
- ³⁷ George Mason University, 4400 University Drive, Fairfax, VA 22030, USA
- ³⁸ American Association of Variable Star Observers, 185 Alewife Brook Parkway, Suite 410, Cambridge, MA 02138, USA
- ³⁹ Dept. of Physics and Astronomy, Kansas University, 1082 Malott, 1251 Wescoe Hall Drive, Lawrence, KS 66045, USA
- ⁴⁰ Division of Geological and Planetary Sciences, California Institute of Technology, 1200 E California Boulevard, Pasadena, CA 91125, USA
- ⁴¹ Department of Multi-Disciplinary Sciences, Graduate School of Arts and Sciences, The University of Tokyo, 3-8-1 Komaba, Meguro, Tokyo 153-8902, Japan
- ⁴² School of Physics & Astronomy, University of Birmingham, Edgbaston, Birmingham, B15 2TT, UK
- ⁴³ Department of Astronomy, University of California Berkeley, CA 94720, USA
- ⁴⁴ Department of Telecommunications and Teleinformatics, Silesian University of Technology, Akademicka 16, 44-100 Gliwice, Poland
- ⁴⁵ Phil Evans, El Sauce Observatory, Coquimbo Province, Chile
- ⁴⁶ Caltech/IPAC, Mail Code 100-22, Pasadena, CA 91125, USA
- ⁴⁷ Departamento de Astronomía y Astrofísica, Universidad de Valencia, E-46100 Burjassot, Valencia, Spain
- ⁴⁸ Observatorio Astronómico, Universidad de Valencia, E-46980 Paterna, Valencia, Spain
- ⁴⁹ INAF—Osservatorio Astrofisico di Catania, Via S.Sofia 78, I-95123, Catania, Italy
- ⁵⁰ Komaba Institute for Science, The University of Tokyo, 3-8-1 Komaba, Meguro, Tokyo 153-8902, Japan
- ⁵¹ Instituto de Astrofísica de Canarias (IAC), 38205 La Laguna, Tenerife, Spain
- ⁵² NASA Exoplanet Science Institute, Caltech/IPAC, MC 314-6, 1200 E California Boulevard, Pasadena, CA 91125, USA
- ⁵³ Department of Astronomy, Tsinghua University, Beijing 100084, People's Republic of China
- ⁵⁴ Dipartimento di Fisica, Università degli Studi di Torino, via Pietro Giuria 1, I-10125 Torino, Italy
- ⁵⁵ Astrobiology Research Unit, Université de Liège, Allée du 6 Août 19C, B-4000 Liège, Belgium
- ⁵⁶ Oukaimeden Observatory, High Energy Physics and Astrophysics Laboratory, Cadi Ayyad University, Marrakech, Morocco
- ⁵⁷ Grand Pra Observatory, 1984 Les Haudères, Switzerland
- ⁵⁸ Department of Astronomy and Astrophysics, University of California, Santa Cruz, CA 95064, USA
- ⁵⁹ Observatori de Ca l'Ou, Carrer de dalt 18, Sant Martí Seseuioles 08282, Barcelona, Spain
- ⁶⁰ Crow Observatory, Portalegre, Portugal
- ⁶¹ Division of Geological and Planetary Sciences, California Institute of Technology, 1200 East California Boulevard, Pasadena, CA 91125, USA
- ⁶² Department of Astrophysical Sciences, Princeton University, NJ 08544, USA
- ⁶³ Astrophysics Group, Keele University, Staffordshire, ST5 5BG, UK
- ⁶⁴ Department of Physics & Astronomy, George Mason University, 4400 University Drive MS 3F3, Fairfax, VA 22030, USA
- ⁶⁵ Nicolaus Copernicus Astronomical Center, Polish Academy of Sciences, ul. Rybicka 8, 87-100 Toruń, Poland
- ⁶⁶ Department of Earth and Planetary Sciences, University of California, Riverside, CA 92521, USA
- ⁶⁷ SUPA Physics and Astronomy, University of St. Andrews, Fife, KY16 9SS, UK
- ⁶⁸ Department of Astronomy, California Institute of Technology, Pasadena, CA 91125, USA
- ⁶⁹ NASA Ames Research Center, Moffett Field, CA 94035, USA
- ⁷⁰ Campo Catino Astronomical Observatory, Regione Lazio, Guarcino (FR), 03010, Italy
- ⁷¹ Space Sciences, Technologies and Astrophysics Research (STAR) Institute, Université de Liège, Allée du 6 Août 19C, B-4000 Liège, Belgium
- ⁷² Dept. of Physics & Astronomy, Swarthmore College, Swarthmore, PA 19081, USA
- ⁷³ Department of Astronomy, The Ohio State University, 4055 McPherson Laboratory, 140 West 18th Avenue, Columbus, OH 43210 USA
- ⁷⁴ Data Observatory Foundation, Providencia, Santiago, Chile
- ⁷⁵ Department of Physics and Astronomy, University of Louisville, Louisville, KY 40292, USA
- ⁷⁶ Kourvka observatory, Ural Federal University, 19 Mira Street, Yekaterinburg, Russia
- ⁷⁷ The Maury Lewin Astronomical Observatory, Glendora, CA 91741, USA
- ⁷⁸ Astrobiology Center, 2-21-1 Osawa, Mitaka, Tokyo 181-8588, Japan
- ⁷⁹ National Astronomical Observatory of Japan, 2-21-1 Osawa, Mitaka, Tokyo 181-8588, Japan
- ⁸⁰ Astronomical Science Program, Graduate University for Advanced Studies, SOKENDAI, 2-21-1, Osawa, Mitaka, Tokyo, 181-8588, Japan
- ⁸¹ Department of Physics & Astronomy, University of California Irvine, Irvine, CA 92697, USA
- ⁸² NASA Exoplanet Science Institute—Caltech/IPAC, Pasadena, CA 91125, USA
- ⁸³ Département de physique, Université de Montréal, 1375 Avenue Thérèse-Lavoie-Roux, Montréal, Québec, H3T 1J4, Canada
- ⁸⁴ Trotter Institute for Research on Exoplanets (iREx), Université de Montréal, Montréal, QC, H3C 3J7, Canada
- ⁸⁵ Wild Boar Remote Observatory, San Casciano in val di Pesa, Firenze, Italy
- ⁸⁶ Gruppo Astrofili Catanesi, Catania, Italy
- ⁸⁷ Faculty of Physics, Moscow State University, 1 bldg. 2, Leninskie Gory, Moscow 119991, Russia
- ⁸⁸ Villa '39 Observatory, Landers, CA 92285, USA
- ⁸⁹ U.S. Naval Observatory, Washington, DC 20392, USA
- ⁹⁰ Astronomy Department, 501 Campbell Hall 3411, University of California, Berkeley, CA 94720, USA
- ⁹¹ Centre for Star and Planet Formation, Natural History Museum of Denmark & Niels Bohr Institute, University of Copenhagen, Øster Voldgade 5-7, DK-1350 Copenhagen K., Denmark
- ⁹² School of Physics and Astronomy, Tel Aviv University, Tel Aviv, 6997801, Israel
- ⁹³ Department of Astronomy, Wellesley College, Wellesley, MA 02481, USA
- ⁹⁴ Waffelow Creek Observatory, 10780 FM 1878, Nacogdoches, TX 75961, USA
- ⁹⁵ Gemini Observatory/NSF's NOIRLab, 670 N. A'ohoku Place, Hilo, HI 96720, USA
- ⁹⁶ Department of Physics and Astronomy, Union College, 807 Union Street, Schenectady, NY 12308, USA
- ⁹⁷ European Southern Observatory, Karl-Schwarzschild-Straße 2, D-85748 Garching bei München, Germany
- ⁹⁸ Physikalisches Institut, University of Bern, Gesellschaftstrasse 6, 3012 Bern, Switzerland
- ⁹⁹ Departamento de Astrofísica, Universidad de La Laguna (ULL), 38206, La Laguna, Tenerife, Spain
- ¹⁰⁰ Wild Boar Remote Observatory, San Casciano in val di Pesa, Firenze, 50026, Italy
- ¹⁰¹ American Association of Variable Star Observers, 49 Bay State Road, Cambridge, MA 02138, USA
- ¹⁰² Department of Physics and Astronomy, University of Kansas, 1251 Wescoe Hall Drive, Lawrence, KS 66045, USA
- ¹⁰³ Instituto de Astrofísica de Andalucía (IAA-CSIC), Glorieta de la Astronomía s/n, 18008 Granada, Spain
- ¹⁰⁴ Brierfield Observatory, Bowral, NSW, Australia
- ¹⁰⁵ Department of Physical Sciences, Kutztown University, Kutztown, PA 19530, USA
- ¹⁰⁶ Department of Astronomy, Yale University, New Haven, CT 06511, USA
- ¹⁰⁷ Center for Data Intensive and Time Domain Astronomy, Department of Physics and Astronomy, Michigan State University, East Lansing, MI 48824, USA
- ¹⁰⁸ South African Astronomical Observatory, P.O. Box 9, Observatory, Cape Town 7935, South Africa
- ¹⁰⁹ Department of Physics and Kavli Institute for Astrophysics and Space Research, Massachusetts Institute of Technology, Cambridge, MA 02139, USA

¹¹⁰ INAF—Osservatorio Astrofisico di Torino, via Osservatorio 20, I10025, Pino Torinese, Italy¹¹¹ Kotizarovci Observatory, Sarsoni 90, 51216 Viskovo, Croatia¹¹² Hazelwood Observatory, Churchill, VIC 3840, Australia¹¹³ Perth Exoplanet Survey Telescope, Perth, WA 6076, Australia¹¹⁴ Curtin Institute of Radio Astronomy, Curtin University, Bentley, WA 6102, Australia¹¹⁵ Department of Physics & Astronomy, University of California Los Angeles, Los Angeles, CA 90095, USA¹¹⁶ Centre for Astrophysics, University of Southern Queensland, West Street, Toowoomba, QLD 4350, Australia¹¹⁷ Department of Physics and Astronomy, University of Notre Dame, Notre Dame, IN 46556, USA¹¹⁸ Department of Physics, Engineering and Astronomy, Stephen F. Austin State University, 1936 North Street, Nacogdoches, TX 75962, USA*Received 2023 August 16; revised 2024 February 15; accepted 2024 February 29; published 2024 April 23*

Abstract

JWST has ushered in an era of unprecedented ability to characterize exoplanetary atmospheres. While there are over 5000 confirmed planets, more than 4000 Transiting Exoplanet Survey Satellite (TESS) planet candidates are still unconfirmed and many of the best planets for atmospheric characterization may remain to be identified. We present a sample of TESS planets and planet candidates that we identify as “best-in-class” for transmission and emission spectroscopy with JWST. These targets are sorted into bins across equilibrium temperature T_{eq} and planetary radius R_p and are ranked by a transmission and an emission spectroscopy metric (TSM and ESM, respectively) within each bin. We perform cuts for expected signal size and stellar brightness to remove suboptimal targets for JWST. Of the 194 targets in the resulting sample, 103 are unconfirmed TESS planet candidates, also known as TESS Objects of Interest (TOIs). We perform vetting and statistical validation analyses on these 103 targets to determine which are likely planets and which are likely false positives, incorporating ground-based follow-up from the TESS Follow-up Observation Program to aid the vetting and validation process. We statistically validate 18 TOIs, marginally validate 31 TOIs to varying levels of confidence, deem 29 TOIs likely false positives, and leave the dispositions for four TOIs as inconclusive. Twenty-one of the 103 TOIs were confirmed independently over the course of our analysis. We intend for this work to serve as a community resource and motivate formal confirmation and mass measurements of each validated planet. We encourage more detailed analysis of individual targets by the community.

Unified Astronomy Thesaurus concepts: [Exoplanet astronomy \(486\)](#); [Exoplanet atmospheres \(487\)](#); [Transit photometry \(1709\)](#); [James Webb Space Telescope \(2291\)](#); [Exoplanets \(498\)](#)

Supporting material: machine-readable tables

1. Introduction

Since the first exoplanets were discovered by Wolszczan & Frail (1992) and Mayor & Queloz (1995), over 5000 exoplanets have been confirmed, opening up a wide array of planets of varying sizes, temperatures, and masses for study. The rate of exoplanet discovery has notably accelerated over time, originating with serendipitous or targeted observations and culminating in the concerted efforts of ground-based surveys such as the Wide Angle Search for Planets (WASP; Pollacco et al. 2006), the Hungarian-made Automated Telescope Network (HATNet; Bakos et al. 2004), and HATSouth (Bakos et al. 2013), and space-based observatories such as the COncvection, ROTation and planetary Transits satellite (CoRoT; Auvergne et al. 2009; Moutou et al. 2013), Kepler (Borucki et al. 2010), K2 (Howell et al. 2014), and the Transiting Exoplanet Survey Satellite (TESS; Ricker et al. 2015).

Although the exoplanet discovery process can reveal important properties of planets like mass and radius, further observations and analysis are required to understand the conditions on the planets themselves and examine the planet’s atmospheric

composition and dynamics. The first observation of an exoplanetary atmosphere was conducted by Charbonneau et al. (2002), and since then, in a parallel to the diversity of the types of exoplanets, spectroscopic characterization has revealed a wide variety of atmospheric compositions and aerosol properties as well (e.g., Sing et al. 2016; Welbanks et al. 2019; Mansfield et al. 2021; Changeat et al. 2022; August et al. 2023).

Transmission and emission spectroscopy have proven to be the workhorses of exoplanetary atmospheric characterization. These methods utilize the absorption of stellar flux transmitted through the exoplanetary atmosphere and the thermal emission from the exoplanet to probe the atmospheric characteristics of the planet. Exoplanet atmospheric characterization and spectral modeling have greatly expanded our understanding of the formation and evolution of planets, the physical and chemical processes that shape planetary atmospheres, and atmospheric aerosol properties (e.g., Madhusudhan 2019; Mollière et al. 2022; Wordsworth & Kreidberg 2022) as well as the range of diverse conditions within each of these individual topics. As the outermost layer of a planet, the atmosphere is the easiest component of an exoplanet to probe in detail and can be used to infer other planetary properties.

Although space- and ground-based resources for atmospheric characterization have become more abundant since the first transmission spectrum was taken, these resources remain in high demand. The premier atmospheric characterization tools have largely been the Hubble Space Telescope (HST) and, until its retirement in 2020, the Spitzer Space Telescope, both of which have historically been heavily oversubscribed. High-resolution spectrographs on ground-based telescopes

¹¹⁹ NASA Postdoctoral Program Fellow.¹²⁰ NSF Graduate Research Fellow and MIT Presidential Fellow.¹²¹ NSF Graduate Research Fellow.¹²² Visiting Graduate Student Fellow.

have become increasingly important in the study of exoplanet atmospheres, but these are often limited by what is visible in the night sky and signal-to-noise ratios (S/Ns).

The highly anticipated JWST launched in 2021 (Gardner et al. 2006, 2023) with promises of greatly improved capabilities for transit and eclipse exoplanet atmospheric characterization (e.g., Deming et al. 2009; Greene et al. 2016; Stevenson et al. 2016) owing to its large aperture and infrared (IR) instrument complement. Although still early in its mission, JWST has already begun delivering on these promises with its first year of exoplanet results (e.g., Ahrer et al. 2023; Greene et al. 2023; Kempton et al. 2023; Tsai et al. 2023). This is not even to mention JWST’s capabilities for the spectroscopy of directly imaged exoplanets (e.g., Miles et al. 2023), which is impressive but outside the scope of this work. But time on JWST is in high demand, and this, coupled with the review process for general observer programs, has resulted so far in a patchwork of exoplanet atmospheric observations.

When it comes to identifying targets for atmospheric characterization observations, there is a critical synergy between JWST and TESS. Touted from the very beginning as a “finder scope for JWST,” the almost-all-sky survey strategy of TESS was intended to find a myriad of new planets around bright, nearby stars that would be amenable to atmospheric characterization with JWST (Deming et al. 2009), in contrast to the dimmer, more distant host stars of Kepler planetary systems. So far, TESS has discovered more than 300 confirmed planets, with more than 4000 planet candidates classified as unconfirmed TESS Objects of Interests (TOIs) without either a false positive or confirmed planet disposition.¹²³ There is currently no published false-positive rate for TESS, although recent work estimates that it could be somewhere between 15% and 47% depending on the mass of the planet and host star (Zhou et al. 2019; Kunimoto et al. 2022). Therefore, it is probable that many of these 4000 TOIs are false positives. However, if even a fraction of them are true planets, this would dramatically grow the sample of planets whose atmospheres may be well suited to observe and characterize with JWST.

In fact, some of the highest-quality (i.e., highest S/N) atmospheric characterization exoplanet targets likely still lie among the unconfirmed TOIs list, since TESS has unique capabilities for finding small planets orbiting bright stars in particular. The JWST-TESS synergy is demonstrated especially by the fact that $\sim 37\%$ of JWST Cycle 1 and $\sim 56\%$ of JWST Cycle 2 exoplanet targets are TESS discoveries. This high proportion of TESS-discovered JWST targets is displayed in Figure 1. With JWST already flying, it is of the utmost importance to systematically and expeditiously identify the best JWST targets to provide a uniform coverage of parameter space.

In an effort to better streamline use of JWST for atmospheric characterization and identify which targets are likely to exhibit the most clearly detectable features in their atmospheric spectra, we present a set of “best-in-class” targets for transmission and emission spectroscopy. Our aim is to produce a sample of planets (or likely planets) well suited for JWST atmospheric characterization to serve as a community resource for upcoming JWST proposal cycles and future observing programs aimed at regions of planetary parameter space where the highest S/N targets have yet to be identified. Under mass assumptions that we describe in

Section 3, these targets are expected to be well suited for JWST. In order to increase the usefulness of our prioritization scheme, we also perform vetting and validation analyses on each member of the best-in-class sample, since our initial rankings make no distinction between confirmed and candidate planets. We first describe our analysis procedure for our ranking and validation analyses in Section 2.

2. Methodology

Our analysis procedure falls into three main steps: (i) generation of the best-in-class sample and ranking of confirmed and candidate planets within each parameter space bin, (ii) vetting of each unconfirmed candidate planet that appears in the best-in-class sample using a variety of ground-based observations and results from previously published vetting software, and (iii) validation analysis of each planet candidate using multiple statistical-validation software packages. A graphical summary of this procedure can be found in Figure 2.

Our best-in-class sample consists of the targets ranked in the top five according to the transmission spectroscopy metric (TSM) and emission spectroscopy metric (ESM) from Kempton et al. (2018) within each cell of a grid spanning the planetary radius and equilibrium temperature (R_p - T_{eq}) space, which is described in Section 3. R_p - T_{eq} axes were chosen since planetary radius (R_p) is expected to be a proxy for metallicity (Baraffe et al. 1998; Fortney et al. 2013) while temperature correlates to chemistry and aerosol formation (Gao et al. 2020), and both parameters are easy to estimate for transiting exoplanets. Metallicity and atmospheric chemistry can both provide insights to the formation, physical processes, and composition of a planet’s atmosphere and are important to probe. We account for the technical capabilities of JWST’s instruments through the inclusion and calculation of various additional metrics (e.g., stellar host magnitude, expected atmospheric signal size, and observability metrics benchmarked against JWST’s instrumental capabilities) for each target and further incorporate these values into our rankings, thus tuning our best-in-class sample to JWST specifically. A further description of our methods in obtaining the sample of planets and planet candidates, generating atmospheric characterization and observability metrics and ultimately ranking the targets into our best-in-class framework, can be found in Section 3.

In our rankings, we initially make no distinction between confirmed planets and unconfirmed TOIs in order to assess how the TESS planet candidates fit in with the overall sample and to identify which TOIs might displace known planets as best-in-class atmospheric characterization targets. For each unconfirmed TOI on our best-in-class list, we perform cursory vetting and statistical validation to determine which targets are likely false positives and which are worthy of additional follow-up prior to future atmospheric characterization observations with JWST. We note that while we only statistically “validate” planets rather than label them as “confirmed,” we consider them to be planets for the purposes of our best-in-class sample (Torres et al. 2004, 2011). For our vetting analysis, we utilize a host of ground-based reconnaissance photometric, spectroscopic, and high-resolution imaging observations to inform our understanding of each unconfirmed TOI and help make determinations on the planetary status of each. Information on these ground-based observations can be found in Section 4. The ground-based observations are used in conjunction with

¹²³ https://exoplanetarchive.ipac.caltech.edu/docs/counts_detail.html

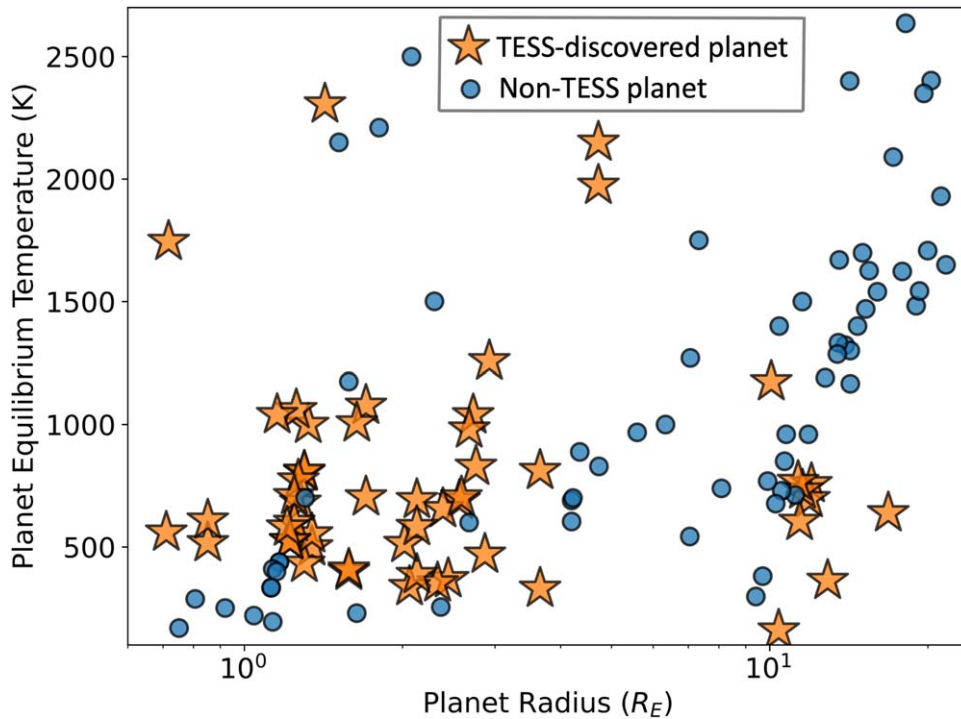


Figure 1. All of the JWST exoplanet targets that are approved for transmission or emission spectroscopy observations in Cycles 1 and 2 across planetary equilibrium temperature and radius. Yellow stars represent approved JWST targets that were discovered by TESS while those represented by blue circles represent planets not discovered by TESS. As evidenced by the plot, TESS-discovered planets constitute a large proportion of approved JWST Cycle 1 and 2 targets for transmission or emission spectroscopy and cover a wide range of parameter space.

results from automated vetting software that have already been published for a large fraction of our sample. This overall vetting process is described in Section 5. Finally, each unconfirmed planet candidate is run through statistical validation software in order to obtain a false-positive probability (FPP) that can be used to quantify the likelihood that each unconfirmed planet candidate is a true planet and further prioritize targets within the best-in-class sample. This analysis also utilizes our ground-based follow-up. Further description of this analysis can be found in Section 6.

We present the final results of our ranking, vetting, and validation analyses in Section 7. This section contains the final ranked best-in-class grids and our assessed disposition for each target (e.g., statistically validated, likely false positive, etc.).

3. Grid Generation

Identifying targets across R_p – T_{eq} space that are well suited to atmospheric characterization with JWST is critical to our understanding of exoplanet atmospheres. By sampling across this parameter space, we expect to cover a range of metallicities as well as atmospheric chemistry and aerosol regimes that would allow us to tease out trends and test models on the population level. This could include a mass–metallicity relation, an aerosol– T_{eq} relation, or a transition between planets that have CO versus CH₄ in their atmospheres as the dominant carbon carrier. To accomplish this, we have divided up the R_p – T_{eq} parameter space into a grid, sorted each planet and planet candidate into cells within this grid, and ranked each target according to its expected S/N approximated via its TSM or ESM.

3.1. Provenance of Sample Parameters and Transmission Spectroscopy Metric and Emission Spectroscopy Metric Calculation

In order to obtain a standardized list of planets and planet candidates to consider when determining which are the best-in-class for atmospheric characterization with JWST, we relied on the data tables maintained by the NASA Exoplanet Archive and the parameter values contained therein.¹²⁴ The Exoplanet Archive collates parameter sets for confirmed and unconfirmed planets and acts as a single repository for published parameter values for each target. For the confirmed planets, we downloaded the Planetary Systems table, which contains every planet that has a published validation or confirmation, and the accompanying set of parameter values, with a single parameter set labeled as the default by the archive staff for each planet. For the unconfirmed TOIs, we downloaded the TESS Candidates table from the Exoplanet Archive, which updates directly from the TESS TOI Catalog (Guerrero et al. 2021) with new targets and refined parameter values from the TESS mission. These two tables were both downloaded on 2022 November 3. The highest TOI number alerted at this time was TOI-5863.

We elected to use the parameter set denoted as the default set of values for each of the planets in the Planetary Systems table throughout our analysis. In the case that the default parameter set was incomplete and missing values for critical parameters necessary to our analysis, values were pulled from other, nondefault parameter sets for each planet, if they existed. Critical values were planetary radius (R_p), stellar radius (R_*), stellar effective temperature (T_*), semimajor axis (a), J

¹²⁴ <https://exoplanetarchive.ipac.caltech.edu/>

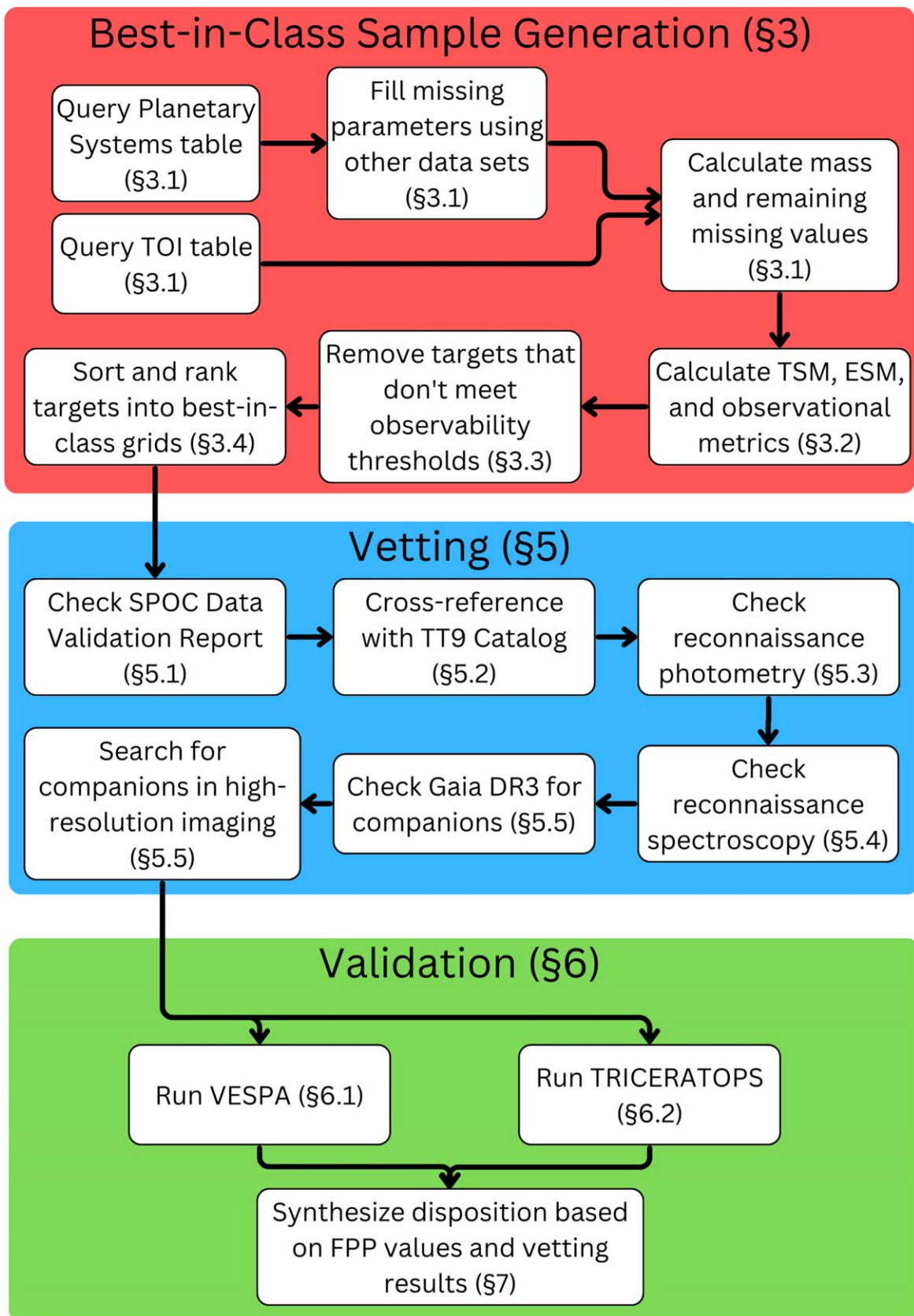


Figure 2. A schematic outline of our analysis procedure. From the initial query of the Exoplanet Archive and generation of the best-in-class sample, each target went through every step of the procedure to check for factors that could indicate a false positive to arrive at a final disposition. Not every vetting step applied to every target due to lack of follow-up, so each vetting step was applied when possible but skipped when not. The sections where each step is discussed more in-depth are listed in parentheses.

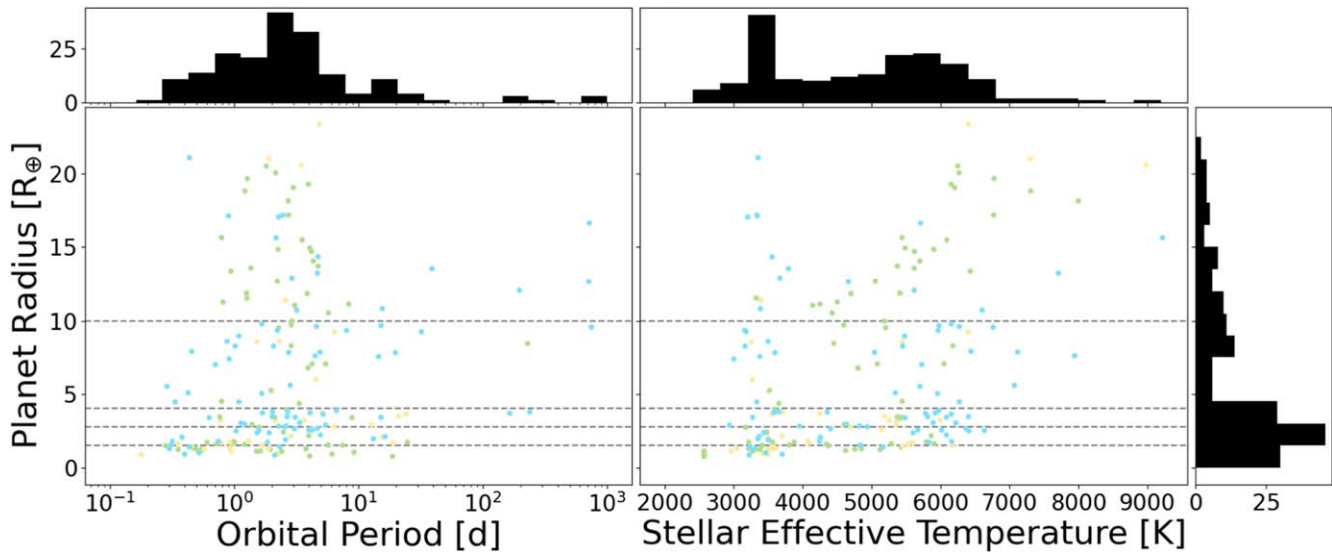


Figure 3. The spread of targets in our best-in-class samples. Left: the orbital periods and planetary radii of the combined TSM and ESM best-in-class samples. Right: the effective temperature of the host stars and the planetary radii of the same combined best-in-class sample. Also shown are the marginal distributions for each variable. The edges of the radius bins are represented by the gray dashed horizontal lines. Points are color-coded according to the mass measurement categories presented in Figure 4. Although only selected to adequately cover the planetary radius and equilibrium temperature parameter space, the best-in-class sample exhibits good coverage of multiple different parameter spaces and can be considered a representative subset of exoplanetary targets.

magnitude, and K magnitude. Values with lower uncertainties from other parameter sets were given priority for inclusion in the final parameter set. This list of critical parameters represents the bare minimum set of quantities necessary to perform our best-in-class ranking procedure. The only other quantity that is used, if available, is planet mass (M_p) and its associated uncertainties for planets that are confirmed. Taken together, the critical quantities listed above and M_p are all of the parameters used by our ranking framework.

We calculated the TSM and ESM for each planet according to the prescription outlined in Kempton et al. (2018), specifically their Equations (1) and (4). The calculation of TSM and ESM assumes cloud-free atmospheres, solar composition for planets larger than $1.5 R_\oplus$, and a pure H_2O steam atmosphere for planets smaller than $1.5 R_\oplus$. These two values represent analytical metrics that quantify the expected S/N in transmission and thermal emission spectroscopy for a given planet and can be used to identify which planets are best suited for atmospheric characterization with JWST relative to one another. We maintained two separate samples for best-in-class targets: one for transmission spectroscopy driven by TSM and the other for emission spectroscopy driven by ESM. Both of these initially started with the same overall sample of planets and planet candidates downloaded from the Exoplanet Archive, and were each shaped by the observational constraints unique to each respective sample. Figure 3 illustrates the parameter space coverage of our combined best-in-class samples.

Even after pulling values from other parameter sets, some targets did not contain finite values for all of the parameters necessary to calculate the spectroscopy metrics and the observability criteria with which we defined and ranked our sample. For targets without a value for the ratio between semimajor axis and stellar radius, a/R_* , we converted both the semimajor axis and the stellar radius to units of meters and took the ratio of the two. In the case that a was missing but a/R_* was a finite value, a/R_* was multiplied by R_* to calculate a . A similar procedure was performed for the ratio between the planet and stellar radii, R_p/R_* . We preferred to use the reported

ratios if they existed to reduce the propagation of potential errors in generating these ratios from the reported values of their individual components. Reported mass and equilibrium temperature (T_{eq}) values were used when reported, but were calculated later in the procedure if unavailable. All targets that still lacked full parameter sets to perform the necessary calculations were removed from the sample. We checked each parameter set to ensure that $R_p/R_* < 1$, and targets with values that did not conform to this criterion were replaced with a value from another parameter set, if available.

For planets from the Planetary Systems table and candidates from the TOI list that did not have published masses, we calculated masses using a mass–radius distribution adapted from the mean of the Chen & Kipping (2017) mass–radius distribution. Specifically, we altered the value of the S^3 coefficient in the power-law function that describes the mass–radius relation of the Jovian planets, $R \propto M^{S^3}$. We set this value to be 0.01 rather than -0.044 , to ensure that each radius value corresponded to a unique mass, while minimally affecting the shape of the curve as presented in Chen & Kipping (2017). We used this distribution up to planetary radii of $15 R_\oplus$, fixing the mass of planets larger than this threshold to $1 M_{Jup}$. Above this radius, the scatter of the mass–radius distribution is large and results in a mean that is nearly constant in mass across radius. This is the same procedure that is used by the Exoplanet Archive to calculate expected masses.

We divided the sample into three categories: confirmed planets with $>5\sigma$ mass measurements, planets marked as confirmed on the Exoplanet Archive with $<5\sigma$ mass measurements, and unconfirmed planet candidates without any mass measurement. Batalha et al. (2019) showed that different mass confidence levels result in different precision with which an exoplanet’s atmosphere can be characterized. A stratification of these targets based on mass measurement will also allow the community to better prioritize follow-up resources for the best-in-class targets, and allowed us to identify which targets are unconfirmed and in need of statistical validation.

Additionally, we calculated the mass of the host star for each TOI based on the star’s log g and radius because stellar mass is not included in the Exoplanet Archive’s TOI table. Using the host star’s reported effective temperature, we also assigned each host star an approximate stellar type for reference. We then calculated the T_{eq} of each planet—both TOI and confirmed—according to Equation (3) of Kempton et al. (2018). This was done to ensure a uniform data set for T_{eq} since the definition of equilibrium temperature varies with each data set on the Exoplanet Archive, with different assumptions regarding surface albedo and atmospheric heat distribution serving as variables with no set standard. Since T_{eq} is integral to our determination of the best targets for transmission and emission spectroscopy, we elected to calculate the value for each planet and planet candidate to ensure a uniform comparison. Our calculation of T_{eq} assumes zero albedo and full day–night heat redistribution.

3.2. Observability Cuts

While useful for relative comparisons between targets, the TSM and ESM only predict the S/N but do not account for other observability considerations such as the absolute signal size relative to the instrumental noise floor or the target being within an instrument’s brightness limits. To incorporate the observability of our sample with JWST into our best-in-class rankings, we also calculated the expected sizes of transmission spectral features and secondary-eclipse depth for transmission and emission spectroscopy, respectively.

3.2.1. Observability in Transmission

We again follow the prescription outlined in Kempton et al. (2018), expressing the size of expected spectral features at one scale height as

$$\frac{2R_p}{R_*^2} \times \frac{kT_{\text{eq}}}{\mu g}, \quad (1)$$

where k is the Boltzmann constant, μ is the mean molecular weight of the atmosphere, and g is the surface gravity of the planet. For planets with $R_p > 1.5 R_{\oplus}$, we assume $\mu = 2.3$ (in units of proton mass, m_p) while for planets with $R_p < 1.5 R_{\oplus}$, we assume $\mu = 18$ proton masses, following the assumption that all planets in a given radius bin have the same atmospheric composition as made by Louie et al. (2018). We calculated g using the expression $g = GM_p/R_p^2$, where G is the gravitational constant and M_p and R_p are the mass and radius of the planet, respectively. The second term of Equation (1) represents the scale height of the planetary atmosphere, H . This is used as a proxy for spectral feature size as it represents the depth into that atmosphere that is probed at a specific wavelength, which in turn determines the measured wavelength-dependent differences in transit depth.

We assumed a depth of $2H$ when calculating expected spectral feature size based off of the spread in the sizes of H_2O features observed using HST’s near-IR (NIR) WFC3 instrument (Stevenson 2016). The average size of these features was reported to be $\sim 1.5H$, but at longer wavelengths such as those probed by JWST the size of spectral features for molecules such as H_2O increases (e.g., Coulombe et al. 2023), so we elected to assume a depth slightly above the average reported by Stevenson (2016). Assuming a larger expected spectral

feature also allows for us to capture more planets for comparison within our sample as well as to account for differences in cloud cover or the mean molecular weight of exoplanet atmospheres.

In fact, for all constraints applied to our sample, we chose liberal thresholds in order to allow for more targets to appear in our best-in-class sample, especially in parameter spaces where there otherwise would be no promising targets. This was done not only for illustrative purposes but also to attempt to account for some of the variance in parameters governing exoplanet atmospheres and potentially improved observational capabilities going forward.

To ensure that all best-in-class targets would be observable with JWST, we imposed a requirement for a 2σ spectral signal size assuming a noise floor of 10 ppm for the NIRCam, NIRISS, and NIRSpec instruments on JWST. These instruments are all ideal for transmission spectroscopy since their wavelength coverage includes prominent transmission spectral features. We note the TSM was benchmarked for use with NIRISS (Kempton et al. 2018).

3.2.2. Observability in Emission

We perform a similar procedure for the secondary-eclipse depth in order to determine which targets are amenable for emission spectroscopy with the MIRI instrument on board JWST. The expected secondary-eclipse depth can be estimated using the expression

$$\frac{B_{7.5}(T_{\text{day}})}{B_{7.5}(T_*)} \times \left(\frac{R_p}{R_*}\right)^2, \quad (2)$$

where $B_{7.5}$ is the Planck function evaluated for a given temperature at a representative wavelength of $7.5 \mu\text{m}$, T_{day} is the dayside temperature of the planet as calculated by $1.1 \times T_{\text{eq}}$, and R_p/R_* is the ratio of the planetary and stellar radii. We calculate the dayside temperature as $1.1 \times T_{\text{eq}}$ to account for the dayside hotspot on the planet, following the analysis by Kempton et al. (2018) that tuned this relation according to a suite of global circulation and one-dimensional atmospheric models. The $7.5 \mu\text{m}$ was chosen as the representative wavelength since it is the center of the “conservative” MIRI Low Resolution Spectroscopy (LRS) bandpass on JWST as data beyond $10 \mu\text{m}$ are often unreliable (Bell et al. 2023; Kempton et al. 2023) and $7.5 \mu\text{m}$ is still near the peak of the MIRI LRS response function (Kendrew et al. 2015; Rieke et al. 2015). We imposed a requirement that the secondary-eclipse depth be measurable to the 3σ level assuming a noise floor of 20 ppm for the MIRI instrument on JWST. There were more small planets contained within the emission spectroscopy sample, and so we were able to adopt a more conservative 3σ threshold rather than the 2σ threshold applied to the transmission spectroscopy sample. We also imposed an ESM > 3 requirement on our emission spectroscopy sample to remove targets that would produce small secondary eclipses even under ideal observing conditions with JWST. Like TSM with NIRISS, ESM was benchmarked for use with MIRI, which is ideal for emission spectroscopy among JWST’s instruments thanks to its longer wavelength coverage that maximizes the ratio between the flux of the planet and that of the host star.

3.3. Additional Cuts and Organizing the Sample

We applied additional observability cuts to the sample to ensure that each of our best-in-class targets would be observable by JWST and would produce significant spectral detections. For transmission spectroscopy targets, we restricted the J magnitude of the host star to >6.0 , while for emission spectroscopy targets, we restricted the K magnitude of the host stars to >6.4 . These values represent the approximate maximum brightnesses at which the NIRCcam long-wavelength channel grism spectroscopy (which can observe the brightest stars of the NIR spectroscopic modes; Beichman et al. 2014) and MIRI LRS (Kendrew et al. 2016) modes will not saturate, respectively, according to v2.0 of the JWST exposure-time calculator (Pontoppidan et al. 2016). We also removed any planets or planet candidates with impact parameter $b > 0.9$ to remove grazing transits that could produce unreliable transit depths.

We then divided our full sample of targets that are observable with JWST into bins of R_p and T_{eq} to determine which targets are best for atmospheric characterization in their class. This division included both confirmed planets and unconfirmed planet candidates. The interior edges of these bins in R_p were chosen in order to match the cutoffs used in Kempton et al. (2018), setting the overall minimum and maximum radii to include the smallest and largest transiting planets at the time the Exoplanet Archive was queried. The temperature bin edges were chosen to capture the ultra-hot Jupiters at $T_{eq} > 2250$ K, the carbon equilibrium chemistry transition from CO (and CO₂) to CH₄ around 800 K (assuming an otherwise solar C/O ratio; Fortney et al. 2013), and roughly equal spacing otherwise. The coldest temperature bin in our sample was chosen to encompass the habitable zone.

3.4. Description of Best-in-class Grids

The planets contained within each bin in radius and temperature space were then sorted and ranked by TSM and ESM for the transmission spectroscopy and emission spectroscopy samples, respectively. This ranking was agnostic to confirmation status and the existence of a well-constrained mass, resulting in a combination of confirmed planets and unconfirmed planet candidates within each grid cell. The top five targets in each bin are considered the best-in-class for that portion of parameter space. Our rankings of the transmission and emission spectroscopy targets are contained within the grids shown in Figure 4.

Almost every bin for both the transmission and emission target samples has at least one unconfirmed planet candidate, with most bins dominated by unconfirmed candidates. While certainly not all of the planet candidates are true planets, if even a fraction of the them are these rankings indicate that there is a large number of TESS planet candidates that are both (i) among the best currently known targets for atmospheric characterization with JWST from a S/N perspective, and (ii) required to provide a uniform coverage of the R_p - T_{eq} space.

4. Follow-up Observations

In order to determine which of the TESS-discovered planet candidates in our best-in-class samples are true planets, we first collated all of the follow-up observations for each target. These follow-up observations provided valuable, independent information on the validity of each planet candidate as true planets. We worked closely with the TESS Follow-up Observation

Program (TFOP) subgroups (SGs) to compile available photometric, spectroscopic, and imaging follow-up observations for each target.¹²⁵ These observations were used in initial vetting to determine whether each target was a likely false positive or if it could proceed to more in-depth vetting and validation. TFOP follow-up observations and the constraints that they impose on the system were incorporated into our vetting and statistical-validation procedures where possible (see Sections 5 and 6). The follow-up resources used in vetting and validating the best-in-class planet candidates are summarized here, with a representative sample of the specific observations used for individual targets detailed in Table 5 located in Appendix B and a full, machine-readable version available from the online version of this article. An outline of where follow-up observations were used in our vetting procedures can be found in the middle panel of Figure 2.

4.1. Ground-based Photometry

TFOP's Sub Group 1 (SG1; Collins 2019) performed ground-based photometry for almost all of the targets in our best-in-class samples in order to clear the background fields of eclipsing binaries (EBs), to check if the candidate transit signal could be identified as on target, and to check the chromaticity of the transit shape and depth. This ground-based photometry was taken by a variety of observatories over a span of multiple years. The TESS Transit Finder, which is a customized version of the `Tapir` software package (Jensen 2013), was used to schedule the transit follow-up observations included here. In Table 1, we include a summary of the observatories used to obtain the ground-based photometry for our samples. Unless otherwise noted, all image data were calibrated and photometric data were extracted using `AstroImageJ` (Collins et al. 2017). Further discussion on the use of ground-based photometry in vetting and validation can be found in Sections 5.3 and 6. More in-depth descriptions of these observatories, their instruments, and data-reduction methods can be found in Appendix C.1.

4.2. Reconnaissance Spectroscopy

TFOP's SG2 performed ground-based reconnaissance spectroscopy on a subset of targets in our best-in-class samples. These observations are crucial to constraining the mass of potential stellar or planetary companions to the host star and for refining the stellar parameters to be used in future analysis. In Table 2, we include a table detailing the instruments used to obtain the reconnaissance spectroscopy used in our analysis. See Section 5.4 for further discussion on how reconnaissance spectroscopy is used in our vetting procedures. More in-depth descriptions of these observatories, their instruments, and data-reduction methods can be found in Appendix C.2.

4.3. High-resolution Imaging

As part of our standard process for validating transiting exoplanets to assess the possible contamination of bound or unbound companions on the derived planetary radii (Ciardi et al. 2015), we also observed a subset of the unconfirmed TOIs in our best-in-class sample with a combination of NIR adaptive-optics (AO) imaging and optical speckle interferometry at a variety of observatories including Gemini, Keck,

¹²⁵ <https://tess.mit.edu/followup>

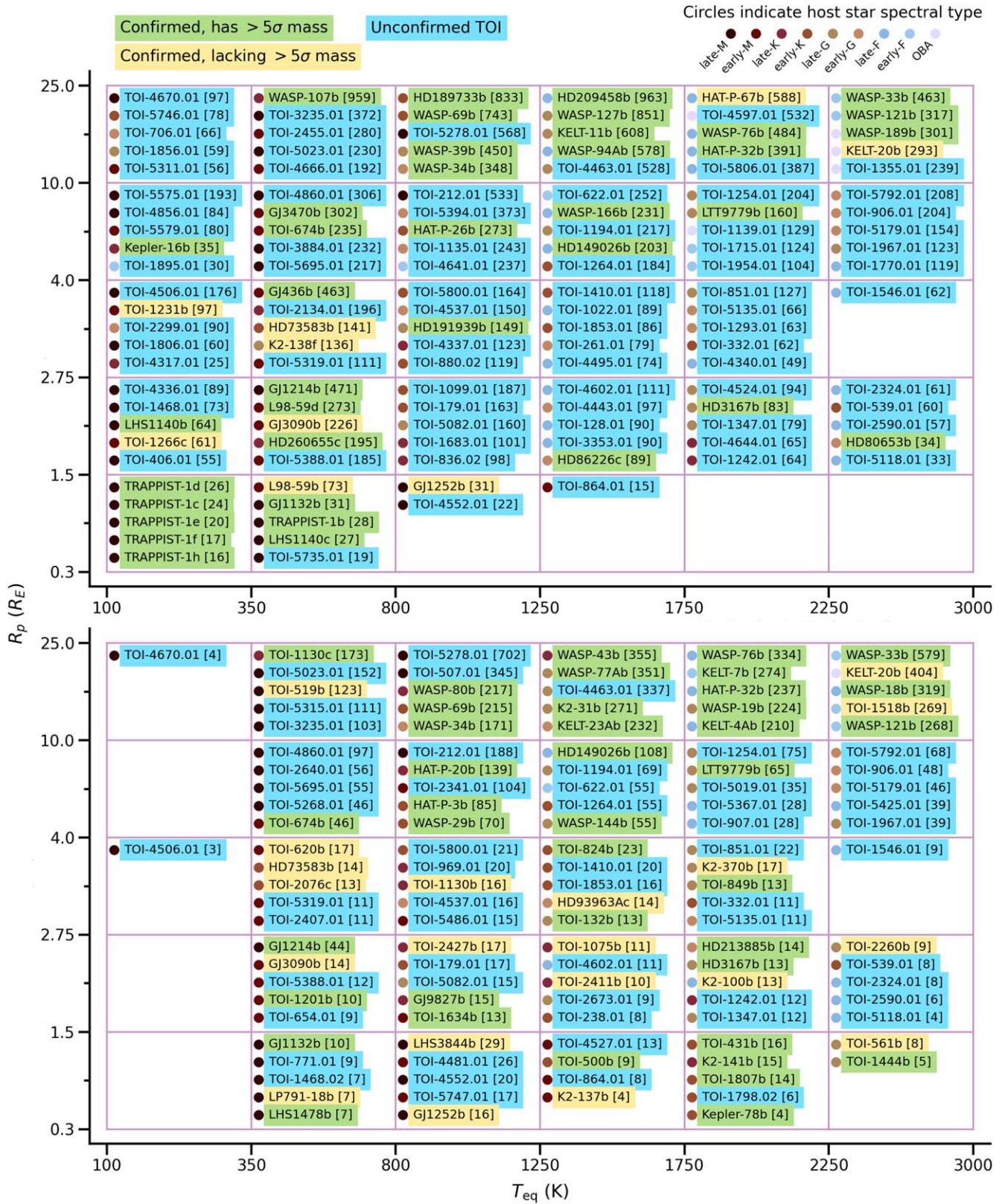


Figure 4. The initial best-in-class rankings of targets for transmission (top) and emission (bottom) spectroscopy as of 2022 November 3 sorted by equilibrium temperature T_{eq} , and planetary radius R_p . Target names are shown with the respective spectroscopy metrics (ESM or TSM) in brackets next to the name. Targets are sorted within each cell by spectroscopy metric in descending order. The approximate stellar type of the host star is denoted by the colored circle to the left of each name, determined by the reported effective temperature. Targets are color-coded by mass status: green targets are confirmed planets with mass measurements $>5\sigma$, yellow targets are confirmed planets with mass measurements $<5\sigma$, and blue targets are unconfirmed TOIs. This sample is the set of targets that we perform our vetting and validation analysis on before presenting the final best-in-class set in the Results section (Section 7).

Table 1

Summary of the TFOP Observatories Used to Obtain Ground-based Photometric Follow-up Observations

Observatory	Location	Diameter
Adams Obs.	Sherman, TX	0.6 m
ASP	Acton, MA	0.36 m
Brierfield Private Obs.	Bowral, Australia	0.36 m
Campo Catino Astron. Obs.	Siding Spring, Australia	0.43 m
Catania Astrophysical Obs.	Catania, Italy	0.91 m
Caucasian Mountain Obs.	Kislovodsk, Russia	0.6 m
CHAT	Atacama, Chile	0.7 m
CRCAO	Kutztown, PA	0.6 m
CROW Obs.	Portalegre, Portugal	0.36 m
Deep Sky West	Rowe, NM	0.5 m
Dragonfly	Mayhill, NM	1.0 m
El Sauce	Coquimbo Province, Chile	0.36 m
ExTrA	Atacama, Chile	0.6 m
Fred L. Whipple Obs.	Amado, AZ	1.2 m
George Mason University	Fairfax, VA	0.8 m
Hazelwood Obs.	Churchill, Australia	0.32 m
LCO CTIO	La Serena, Chile	1 m
LCO CTIO	La Serena, Chile	0.4 m
LCO HAI	Maui, HI	2 m
LCO HAI	Maui, HI	0.4 m
LCO McD	Fort Davis, TX	1 m
LCO McD	Fort Davis, TX	0.4 m
LCO SAAO	Sutherland, South Africa	1 m
LCO SAAO	Sutherland, South Africa	0.4 m
LCO SSO	Coonabarabran, Australia	1 m
LCO SSO	Coonabarabran, Australia	0.4 m
LCO TEID	Tenerife, Spain	1 m
LCO TEID	Tenerife, Spain	0.4 m
Lewin Obs.	Glendora, CA	0.35 m
Lookout Obs.	Colorado Springs, CO	0.5 m
MASTER-Ural	Yekaterinburg, Russia	0.4 m
MEarth-S	La Serena, Chile	0.4 m
Mt. Kent CDK700	Toowoomba, Australia	0.7 m
Mt Lemmon ULMT	Tucson, AZ	0.61 m
Mt Stuart Obs.	Dunedin, New Zealand	0.32 m
MuSCAT	Okayama, Japan	1.88 m
MuSCAT2	Tenerife, Spain	1.52 m
OAUUV	Valencia, Spain	0.3 m
Obs. Astronòmic Albanyà	Albanyà, Spain	0.4 m
Obs. de Ca l’Ou	Barcelona, Spain	0.4 m
PEST	Perth, Australia	0.3 m
Priv. Obs. Herges-Hallenberg	Steinbach-Hallenberg, Ger.	0.28 m
PvDKO	Swarthmore, PA	0.62 m
RCO	Valais Sion, Switzerland	0.4 m
SAINT-EX	San Pedro Mártir, Mexico	1.0 m
Salerno University Obs.	Fisciano, Italy	0.6 m
SPECULOOS-S	Cerro Paranal, Chile	1.0 m
Solaris SLR2	Sutherland, South Africa	0.5 m
SUTO-Otivar	Motril, Spain	0.3 m
TRAPPIST-North	Oukaimeden, Morocco	0.6 m
TRAPPIST-South	La Silla, Chile	0.6 m
Union College Obs.	Schenectady, NY	0.51 m
Villa ’39	Landers, CA	0.35 m
WCO	Nagadoches, TX	0.35 m
Wellesley College Whitin Obs.	Wellesley, MA	0.7 m

Note. Some components of observatory names were abbreviated, such as “observatory” (“obs.”).

Lick, Palomar, the Very Large Telescope (VLT), and WIYN Observatories. The combination of the observations in multiple filters enables better characterization for any companions that may be detected and improves the sensitivity to different types

Table 2

Summary of the TFOP Instruments Used to Obtain Reconnaissance Spectroscopic Follow-up Observations

Instrument	Location	Diameter
CHIRON	Coquimbo, Chile	1.5 m
CORALIE	Coquimbo, Chile	1.2 m
FEROS	Coquimbo, Chile	2.2 m
FIES	La Palma, Spain	2.56 m
HARPS-N	La Palma, Spain	3.58 m
Keck/HIRES	Maunakea, HI	10 m
MINERVA-Australis	Toowoomba, Australia	0.7 m
NRES	Coquimbo, Chile	1.0 m
NRES	Fort Davis, TX	1.0 m
NRES	Mitzpe Ramon, Israel	1.0 m
NRES	Sutherland, South Africa	1.0 m
PFS	Atacama, Chile	6.5 m
TRES	Amado, AZ	1.5 m

Note. Some components of observatory names were abbreviated, such as “observatory” (“obs.”).

of false-positive scenarios (e.g., bound low-mass companions, background stars, etc.). See Sections 5.5 and 6 for further discussion on how high-resolution imaging was incorporated into our vetting and validation analyses, respectively.

4.3.1. Near-infrared Adaptive-optics Imaging

NIR AO observations are performed with a dither pattern to enable the creation of a sky frame from a median of the science frames. All science frames are flat-fielded (which are dark subtracted) and sky subtracted. The reduced science frames are combined into a single combined image using an intra-pixel interpolation that conserves flux, shifting the individual dithered frames by the appropriate fractional pixels; the final resolution of the combined dithers was determined from the FWHM of the point-spread function. The sensitivities of the final combined AO images were determined by injecting simulated sources azimuthally around the primary target every 20° at separations of integer multiples of the central source’s FWHM (Furlan et al. 2017). The brightness of each injected source was scaled until standard aperture photometry detected it with 5σ significance. The final 5σ limit at each separation was determined from the average of all of the determined limits at that separation, and the uncertainty on the limit was set by the rms dispersion of the azimuthal slices at a given radial distance.

4.3.2. Optical Speckle Imaging

High-resolution optical speckle interferometry was performed using the ‘Alopeke and Zorro instruments mounted on the Gemini North and South telescopes, respectively (Howell et al. 2021; Scott et al. 2021). These identical instruments provide simultaneous speckle imaging in two bands (562 and 832 nm) with output data products including a reconstructed image and robust contrast limits on companion detections (Howell et al. 2011). For each observed source, the final reduced data products contain 5σ contrast curves as a function of angular separation, information on any detected stellar companions within the angular range of $\sim 0''.03$ to $1''.2$ (delta magnitude, separation, and position angle), and reconstructed speckle images in each bandpass. The angular separation sampled, from the 8 m telescope diffraction limit

(20 mas) out to $1''2$, can be used to set spatial limits in which companions were or were not detected.

5. Vetting

In order to determine the planetary nature of each target, we performed a uniform vetting procedure on each of the unconfirmed candidates. This included utilizing a mix of publicly available resources and follow-up observations obtained by TFOP. We outline our overall procedure in schematic form in the middle panel of Figure 2. We ran each target through as many steps of our vetting procedure as possible given the availability of resources at the time of analysis in early 2023 since not all targets had the resources to complete each step in our procedure.

Although our vetting procedure checked for a number of false-positive indicators, we refrained from classifying a target as a likely false positive unless multiple false-positive indicators suggested that the origin of the transit signal could not have been a planet. Our conservative approach to vetting passed most targets on to statistical validation and provided invaluable information to be used in conjunction with the results from our validation analysis to make a final determination, such as if the signal is on target and if there were any potentially contaminating sources contained in the light curve’s extraction aperture. In this way, vetting served as a complement to a more holistic determination of the planetary nature that accounts for a larger number of factors than any individual analysis alone could provide.

For all of our vetting, we used the orbital and planetary parameter values posted on ExoFOP unless follow-up observations revealed more accurate or precise values for a given parameter, in which case the parameters obtained from follow-up were used.¹²⁶ There were seven targets with ambiguous periods contained in our best-in-class samples from the query of the Exoplanet Archive (TOIs 706.01, 1856.01, 1895.01, 2299.01, 4317.01, 5575.01, and 5746.01). These targets were single transits that transited again in one or more later TESS sectors, but without measuring two or more consecutive transits the period could not be confidently determined. The orbital period of TOI-5575.01 was uniquely determined to be 32.07 days through follow-up observations over the course of our analysis.¹²⁷ We propagated this updated period throughout our analysis and report the planet’s updated parameters in our final best-in-class sample. Since we are unable to obtain the true periods of these remaining six targets without a concerted observing campaign, we analyzed them with the reported ExoFOP periods that represent upper limits to the true periods. Shorter periods would likely result in higher equilibrium temperatures, which, although this would boost the TSM, could place these targets in a different temperature bin where they may not rank in the top five targets in their R_p bin. We recognize that the periods and therefore amenability to atmospheric characterization with JWST may change for these targets, but we include them in our best-in-class samples to emphasize their potential as prime JWST targets and encourage their further study.

5.1. TESS SPOC Data Validation Report

Around 92% of the targets in our best-in-class samples were either discovered by (or at the very least run through) the TESS

Science Processing Operations Center (SPOC) pipeline (Jenkins et al. 2016) at NASA’s Ames Research Center. This SPOC pipeline performs a number of tasks on each target including light-curve extraction to generate simple aperture photometry (SAP) light curves (Twicken et al. 2010; Morris et al. 2020) and systematic error correction to generate presearch data conditioning simple aperture photometry (PDCSAP; Smith et al. 2012; Stumpe et al. 2012, 2014) light curves. The pipeline also searches for potential planets as well as performs a suite of diagnostic tests in the Data Validation (DV) module to help adjudicate the planetary nature of each signal (Twicken et al. 2018; Li et al. 2019). Upon running the pipeline, the outputs were reviewed by the TESS TOI Working Group (TOI WG) to perform initial vetting. This initial vetting has already been performed by the TOI WG for all of our targets, but we reviewed the SPOC pipeline outputs again to ensure nothing was missed.

The DV module includes a depth test of the odd and even transits, a statistical bootstrap test that accounts for the nonwhite nature of the observation noise to estimate the probability of a false alarm from random noise fluctuations, a ghost diagnostic test to compare the detection statistic of the optimal aperture against that of a halo with a 1 pixel buffer around the optimal aperture, and a difference-image centroid test. At the conclusion of these tests, the module synthesizes a summary of the results for each individual test, including assigning a pass/fail disposition for each test. We used the results of each of these tests in our vetting efforts to help determine if a target was a likely planet, likely false positive, or false alarm.

In addition to the DV module results, we also determined if the period was ambiguous for a given target due to nonconsecutive transits from gaps in the TESS data. Although not a false-positive indicator, this was flagged for future reference in downstream analyses. We also checked the light curves for significant photometric modulation indicative of stellar activity that could pose a problem in future vetting and validation analysis. In the absence of SPOC DV results, we still inspected the light curve and ephemerides for an ambiguous period or photometric modulation using available, published light curves such as those from MIT’s Quick Look Pipeline (QLP; Huang et al. 2020).

5.2. DAVE Vetting from Cacciapuoti et al. (2022)

A subset ($\sim 15\%$) of our targets had already been vetted not only by the TESS TOI WG but by an independent team using the Discovery And Vetting of Exoplanets (DAVE; Kostov et al. 2019) pipeline. The results of this vetting were collated in Cacciapuoti et al. (2022), where each of the 999 targets vetted were assigned a final disposition as to the target’s planetary nature.

DAVE is an automated vetting pipeline built upon many of the tools developed for vetting planets in Kepler data (e.g., RoboVetter; Coughlin et al. 2014) and has been used extensively in vetting planets for TESS (e.g., Gilbert et al. 2020; Hord et al. 2021; Quintana et al. 2023). DAVE performs two sets of vetting tests: (i) light-curve-based vetting tests searching for odd/even transit depth differences, secondary eclipses, and light-curve modulations; and (ii) image-based centroid tests to check the photometric motion on the TESS image during transit.

¹²⁶ <https://exofop.ipac.caltech.edu/tess/>

¹²⁷ <https://exofop.ipac.caltech.edu/tess/target.php?id=160162137>

For the targets in our best-in-class samples that were also contained in the Cacciapuoti et al. (2022) catalog, we included their dispositions in our vetting analysis. Since there is overlap between the tests performed by the TESS SPOC pipeline and DAVE, we treat the two as independent checks of one another and review the results in comparison.

5.3. Reconnaissance Photometry

Due to the large 21'' pixel size of TESS, ground-based photometry at higher spatial resolutions is crucial in determining whether a transit-like feature is occurring on-target or is the result of a background target in the star field that may have been blended within the TESS pixel. Stars nearby the target are checked for deep EBs that could cause the observed transits and are ruled out on a case-by-case basis. Any deviations from an on-time transit are also noted. These often occur due to uncertainties in the period or mid-transit time reported by ExoFOP but may be caused by gravitational interactions within the system. If the period deviates significantly from the reported period, the ephemerides are refined based on the ground-based photometric observations. This was the case for multiple targets, especially those with fewer sectors of TESS data or those with an ambiguous period.

In addition to checking which star the transit-like feature originates from, ground-based photometry uses multiple filters to check for possible chromaticity in the transit depth that would indicate an EB rather than a planet is causing the transit. A light curve is also extracted from the target star with a small aperture to mitigate the contamination from nearby stars. The transit depth is measured to ensure that it is not only consistent across wavelength bandpasses but is the right depth to cause the transit observed in the TESS data.

TFOP's SG1 synthesizes the results of the photometric observations for each target into a single disposition describing the confidence with which a signal can be considered on-target. We utilized these dispositions and observations when determining which background stars to consider as potential sources of astrophysical false positives in our vetting analysis.

In addition to the photometry gathered by SG1, we also utilized the code DEATHSTAR (Ross et al. 2024) to search archival images from the Zwicky Transient Facility (ZTF; Bellm et al. 2019) for the transit signal.

DEATHSTAR attempts to either confirm or refute exoplanet detections with already available ground-based data from ZTF by extracting light curves for each star in a 2/5 field and plotting them for manual verification of the actual signal location. In this way, we can often tell if an unconfirmed TOI is an exoplanet transiting in front of the target star or an EB on a nearby fainter star. DEATHSTAR creates plots for each extracted light curve and displays them in custom sheets for us to easily find the source of the transiting signal. We worked with SG1 in checking these results with the SG1 Observation Coordinator sheet and sending them to reduce extraneous telescope follow-up time. For deeper transit depths on-target (ranging from 1% to 3%), DEATHSTAR has been able to confirm on-target detections. Because the target stars are bright ($J < 13$ mag) and given ZTF's sensitivity, we were able to check for and rule out EBs among the surrounding stars in the TESS apertures down to the faintest stars that could account for the transit depth. Due to ZTF's multiple filters (g , r , and i bands), we can constrain the chromaticity of the transit signal, which can also indicate or help rule out false positives. In most

of the cases for these targets, the depth was much shallower than a percent, rendering the transits undetectable by DEATHSTAR on-target, but we still cleared all the surrounding stars in the field for being potential EBs, showing the transit signal must originate from the target by process of elimination.

5.4. Reconnaissance Spectroscopy

Although only a subset of the targets in our sample had ground-based spectroscopic observations available, these data provided strong constraints on the presence of bound companions in the target system that photometry is unable to capture. Spectroscopy alone is often able to determine if the stellar spectrum is composite, which would indicate the presence of a bound stellar-mass companion. The presence of a composite spectrum with orbital motion that is consistent with the TESS ephemeris was an automatic likely false-positive designation for the targets in our samples, but only applied to one target (TOI-4506.01).

For most targets, two spectroscopic observations were taken at opposite quadratures assuming a circular orbit at the photometric ephemeris and compared to the photometric ephemeris to determine if they were in phase. Spectroscopic data at opposite quadratures that are out of phase with the photometric ephemeris could indicate the presence of a large stellar-mass object instead of a planet, although this could also indicate a long-term trend in the system due to additional bodies in the system or an eccentric orbit rather than a false-positive scenario. For reconnaissance spectroscopy that was in phase with the photometric ephemeris, the semi-amplitude of the measurements at quadrature was used to constrain the mass of the object producing the transit signal, potentially ruling out stellar masses and providing evidence for the planetary nature of the body.

By virtue of modeling the stellar spectrum, reconnaissance spectroscopy also has the potential to measure parameters such as the effective temperature, metallicity, and $v \sin i$ of the host star. Where possible, we used these measured values rather than those from the TESS Input Catalog (TIC) or Gaia Data Release 3.

Similar to SG1, TFOP's SG2 also synthesizes reconnaissance spectroscopic observations into a disposition for each target. These dispositions capture the confidence that the target is a planetary-mass object and is suitable for precision radial velocity (RV) observations to determine the orbit and constrain the mass further. We broadly utilized these dispositions when vetting to determine whether a target can be safely deemed a likely false positive or should continue to statistical-validation analysis. There were multiple cases where reconnaissance spectroscopy existed but the stellar activity or rotational broadening of spectral features precluded anything but upper limits on the masses of potential companions.

5.5. Imaging Constraints

As a complement to ground-based photometry and reconnaissance spectroscopy, high-resolution imaging can provide strict constraints on the presence of stellar companions in the system or nearby background targets that could potentially contaminate the target signal. Each target was first cross-referenced with the Gaia DR3 catalog to determine if there are any resolved nearby stars within a few arcseconds of the target star. In a handful of cases, Gaia resolved nearby stars at similar

parallaxes to targets in our best-in-class samples. While not a definite indicator of a false positive, the presence of a nearby companion at a similar parallax invited further scrutiny for that particular target. In those cases, we cross-referenced the nearby star with other follow-up observations where possible to determine if the star observed by Gaia may be the cause of anomalies and potential false-positive indicators in the ground-based photometry or reconnaissance spectroscopy.

We also utilized speckle or AO imaging available on ExoFOP (see Section 4.3) that observed each planet candidate in a more targeted manner at a higher angular resolution than Gaia. These observations allowed us to search for bound companions or background stars that may contaminate the photometry or cause the observed transit signal. These observations were also cross-referenced with other follow-up observations to determine how strongly false-positive or dilution scenarios can be constrained or if the signal is likely not due to a planet. The sensitivity curves that these observations produced were also used in our statistical-validation analysis (Section 6).

6. Validation

While vetting is an integral step in determining whether a periodic signal is indeed due to the presence of a planet, it cannot alone demonstrate that a signal is not a false positive. The preferred method for determining whether a signal is a planet is a mass measurement through RV observations, however these oftentimes require a significant commitment of resources and time on targets that may not prove to be planets.

In lieu of a mass measurement, statistics can be used to validate the target rather than confirm it. Statistical validation of a target often only requires photometric and imaging observations as well as planetary and orbital parameters input into one or multiple statistical-validation software packages. Targets that are validated to a greater than 99% confidence threshold are considered planets despite not having a mass measurement (Morton 2012; Giacalone et al. 2021). Since the time and observational resources required to validate a planet are far less than required to obtain a mass measurement, statistical validation serves as an excellent intermediate step to weed out targets that are very likely not planets in order to better streamline and prioritize the RV observations required to confirm a target as a bona fide planet.

In the case of our best-in-class samples, since there are undoubtedly false positives among the unconfirmed planet candidates, we performed statistical validation on all candidate planets to not only determine which targets are most likely to be true planets but which merit follow-up with RV observations. To do this, we run the statistical-validation software *vespa* (Morton 2012, 2015) and *TRICERATOPS* (Giacalone & Dressing 2020) on each of our unconfirmed targets in both the transmission and emission spectroscopy samples.

For all of our targets, we use the orbital and planetary parameters from ExoFOP unless the follow-up observations reported refined parameters (Section 4), in which case the refined parameters were used. For *vespa*, this also included stellar parameters. The refined parameters from follow-up observations were used to recalculate the TSM and ESM values for each target. The refined parameter values were almost always similar to the ExoFOP values, and so incorporating these refinements from follow-up did not produce changes in the best-in-class rankings. TESS photometry was used to produce the phase-folded transits used in both *vespa* and

TRICERATOPS. When possible, we favored light curves produced by the TESS SPOC at the shortest cadence available since shorter-cadence TESS data have been shown to be more photometrically precise when binned than data taken at the binned cadence itself (Huber et al. 2022). A small subset of targets did not have SPOC PDCSAP light curves, in which case we used light curves produced by MIT’s QLP.

6.1. *vespa*

vespa (Morton 2012, 2015) was originally developed for use on Kepler data and compares the input orbital and planetary parameters as well as the phase-folded transit against a number of astrophysical false-positive scenarios to determine the likelihood that the signal can be produced by each false-positive population. Currently, *vespa* tests against the hypotheses that the signal is a blended background or foreground EB (BEB), the target itself is an EB, or the target is a hierarchical-triple system where two of the components form an EB (HEB). To do this, *vespa* simulates a representative population of each false-positive scenario at the observed period and calculates the priors of each scenario, accounting for the probability that the scenario is contained within the photometric aperture, the probability of an orbital alignment that would cause an observable eclipse, and the probability that the eclipse could mimic a transit.

A TRILEGAL simulation (Girardi et al. 2005, 2012) is used to simulate the background star field for each target when calculating the priors. TRILEGAL first builds a geometric model of the Milky Way calibrated using wide-area data in different filters and magnitudes before returning a predicted field of view around a specified target. The likelihoods of each *vespa* scenario are then calculated by modeling the shape of the eclipse for each instance of each false-positive population derived from TRILEGAL and fitting it to the observed light curve. The priors and likelihoods are finally combined to calculate the total FPP of the input transit signal. Signals with an FPP < 0.01 are considered statistically validated.

Beyond the phase-folded light curve and planetary and orbital parameters, *vespa* can also intake sensitivity curves from high-resolution imaging to rule out portions of the false-positive parameter space. Additionally, *vespa* takes the maximum photometric aperture radius as an input to use in calculations of the BEB prior. We set this parameter to 42", the size of two TESS pixels. This is very conservative since the difference-image centroiding results from the SPOC DV analysis often constrain the location of the target star to within a fraction of a pixel of the location of the source of the transit.

vespa assumes that the signal originates on-target, which we have attempted to show for as many targets in our sample as possible (see Section 5). We urge caution in the interpretation of the results from *vespa* in the cases where the signal was not demonstrated to be on-target.

6.2. *TRICERATOPS*

Similar to *vespa*, *TRICERATOPS* (Giacalone & Dressing 2020) compares the user-provided phase-folded transit, orbital, and stellar parameters against a set of astrophysical false-positive scenarios to rule out portions of parameter space in which the false-positive scenarios can remain viable. The methodology of *TRICERATOPS* is identical to *vespa* in many respects, however, in contrast to *vespa*, *TRICERATOPS* was developed

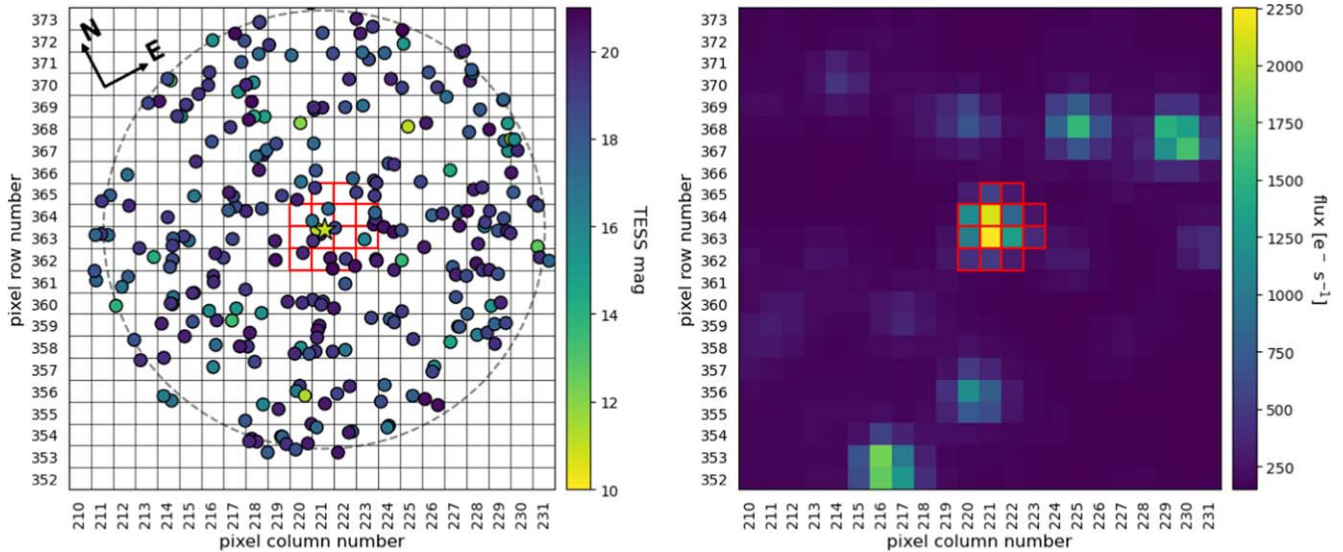


Figure 5. Star field around TOI-4336.01 in TESS Sector 38 used by TRICERATOPS in its FPP and NFPP calculations. Left: plot of the positions of each star within $2\prime.5$ centered on the target, with the color of each point representing the TESS magnitude of the star. The overlaid grid denotes the TESS pixel borders, with pixel column and row numbers labeled on the X and Y-axis, respectively. The dashed gray circle represents a distance of $2\prime.5$ and the red squares denote the extraction aperture used by the SPOC when generating the PDCSAP light curve for this TESS sector. Right: same as left but instead of displaying each background star near the target, TESS data are shown. The SPOC extraction aperture is in red and the color map represents the flux captured by each TESS pixel.

specifically for TESS and accounts for the real sky background of each target out to $2\prime.5$ as well as the TESS point-spread function and aperture used to extract the photometric light curve in each sector of TESS data. An example of what TRICERATOPS considers in this portion of its analysis is seen in Figure 5.

For each target, we used the extraction apertures produced by the TESS SPOC contained within the headers of the SPOC PDCSAP light curves queried by `lightkurve` (Lightkurve Collaboration et al. 2018) on a sector-by-sector basis. For the targets missing SPOC PDCSAP light curves from some or all TESS sectors they were observed in, we used a standard aperture of 5×5 TESS pixels. This is larger than any of the PDCSAP apertures and is the TRICERATOPS default for sectors without provided apertures.

When accounting for nearby background stars for each target, TRICERATOPS queries the TICv8 for the stellar parameters of each star. The TIC is based heavily on Gaia Data Release 2, which has since been updated by Gaia DR3. Therefore, in our analysis, we queried the R.A., decl., mass, effective temperature, parallax, and Gaia G magnitude of the host star Gaia DR3 Catalog for use in our analysis in lieu of using the values provided by the TIC. To convert the Gaia magnitude to TESS magnitude, we used Equation (1) from Stassun et al. (2019), which is valid for dwarfs, subgiants, and giants of any metallicity. We then cross-referenced each Gaia target with the Two Micron All Sky Survey catalog (Skrutskie et al. 2006) to obtain J , H , and K magnitudes where available as these magnitudes are used by TRICERATOPS in its estimation of FPP.

Additionally, we included follow-up constraints into our analysis with TRICERATOPS. When available, we included a contrast curve from high-resolution imaging to constrain the existence of additional stellar-mass companions in the system. Unlike `vespa`, TRICERATOPS accepts only a single contrast curve per target, so in the case a target possessed multiple contrast curves from follow-up observations, we included only the contrast curve that provided the greatest imaging contrast

magnitude agnostic of bandpass to most stringently constrain possible companions in the system. Furthermore, our photometric follow-up allowed us to clear individual nearby stars of potentially harboring EBs that would cause the observed transit signal on-target. Background stars that were definitively determined to not be EBs at the target period or have an eclipse depth that could cause the observed transit on-target were discarded from consideration as potential sources of a false positive. Targets whose transits were observed on-target had all background stars removed from false-positive consideration. As recommended by Giacalone et al. (2021), we ran multiple trials of the TRICERATOPS FPP calculation for each target with a minimum of 10 trials per target, and report the mean of these FPPs.

TRICERATOPS provides not only a final FPP value but also a nearby false-positive probability (NFPP) value that encapsulates the probability that the signal originates from a star other than the target. Giacalone et al. (2021) defines validated planets as signals with $FPP < 0.015$ and $NFPP < 10^{-3}$ and outlines a separate category for marginal validations when $FPP < 0.5$ and $NFPP < 10^{-3}$. We adopt these categories in our determination of the planetary nature for our best-in-class samples. We extend the marginal validations category to `vespa`, which does not explicitly have such a distinction. In the case of `vespa`, we conservatively set the marginal validation threshold to $FPP < 0.25$, lower than that of TRICERATOPS.

Morton et al. (2023) recommends the use of TRICERATOPS in favor of `vespa` since the latter is no longer maintained and has not been updated to account for the modern astronomy landscape. We present validation using both software packages as an independent check on one another in order to be as conservative as possible in any claim of validation made for a given target. Since both tools can be used in evaluating the validity of a target, that enables a more granular target prioritization within our best-in-class sample. Additionally, while TRICERATOPS was developed specifically for TESS and accounts for the actual background star field, it is only able to ingest a single contrast curve as an observational constraint

whereas *vespa* is able to utilize multiple ground-based data sets to constrain the FPP. That said, we emphasize the results of TRICERATOPS over those of *vespa* in cases where their FPP values may disagree. This means that many of the targets in our best-in-class sample that are classified as “likely planets” may actually fall within the realm of true statistical validation when considering only the results from TRICERATOPS.

We also note that our statistical-validation analysis cannot rule out the scenario in which validated planets with $R_p > 9 R_\oplus$ are actually brown dwarfs. A measured mass is required to disentangle the brown dwarf and planet scenarios, and we encourage follow-up on all validated planets to this effect.

7. Results

Of the 103 unconfirmed TESS planet candidates contained in our best-in-class samples, 19 passed vetting and were calculated to have FPP values firmly meeting the threshold for statistical validation from both *vespa* and TRICERATOPS. Additionally, 11 of the original 103 unconfirmed planet candidates reside in potential multiplanet systems (TOI-1468.01, TOI-1468.02, TOI-1798.02, TOI-1806.01, TOI-2134.01, TOI-3353.01, TOI-406.01, TOI-4443.01, TOI-4495.01, TOI-836.02, and TOI-880.02). Three of these have already been confirmed by independent teams (TOI-1468.01 and .02 and TOI-836.02). The remaining eight TOIs are able to take advantage of a “multiplicity boost” to drive their FPP values lower. It has been shown that transit-like signals in systems with multiple transit-like signals are more likely to be true planets, assuming false positives are uniformly distributed throughout the sky (Lissauer et al. 2012). This results in a decreased FPP value of up to $54\times$ depending on the size of the planets, how crowded the field is for signals detected with TESS, and the pipeline with which they were detected (Guerrero et al. 2021). Additionally, these potential multiplanet systems represent an excellent opportunity to perform comparative planetology with the other planets in their system using JWST.

We applied this multiplicity boost to each of the eight candidates listed above, resulting in FPP values below the validation threshold for each of them. Four of these eight already possessed FPP values from *vespa* and TRICERATOPS that were low enough to be statistically validated, but the FPP values of the other four targets (TOI-880.02, TOI-1798.02, TOI-1806.01, and TOI-4443.01) moved from the “marginal validation” range into the “validated planet” range. These targets are shown in Table 3. We strongly recommend these targets for additional, in-depth study and confirmation to measure their masses and model their orbits and atmospheres in preparation for potential observation with JWST.

A total of 29 targets were deemed “likely false positives” (LFPs). These targets all exhibited clear signs of a false positive in the vetting stage and/or produced FPP values from both statistical-validation software packages. A target was deemed a likely false positive if the FPP from both *vespa* and TRICERATOPS did not meet either the validation or marginal validation thresholds. For one of these likely false-positive targets, we were unable to locate the transit-like event that was flagged by the TESS SPOC during our manual inspection of the phase-folded light curve and we deemed it a false alarm (TOI-1022.01). Most of these 29 likely false-positive targets exhibited obvious V-shaped transits indicative of an EB, and a subset of them were revealed by TFOP follow-up to have a nearby ($\leq 2''$) companion star that served as the likely cause of the signal.

Table 3
All of the Statistically Validated Planets in Both the Transmission and Emission Spectroscopy Best-in-class Samples

Planet Name	T_{eq} (K)	R_p (R_\oplus)	Period (days)	TSM	ESM
TOI-128.01	1345	2.22	4.94	90	...
TOI-261.01	1722	3.04	3.36	79	...
TOI-406.01	344	1.96	13.18	55	...
TOI-654.01	749	2.37	1.53	...	9
TOI-880.02	1163	2.78	2.57	119	...
TOI-907.01	1847	9.62	4.58	...	28
TOI-1135.01	1074	9.34	8.03	243	...
TOI-1410.01	1396	2.94	1.22	118	20
TOI-1683.01	929	2.64	3.06	101	...
TOI-1798.02	2122	1.41	0.44	...	6
TOI-1806.01	337	3.41	15.15	60	...
TOI-3353.01	1264	2.67	4.67	90	...
TOI-4443.01	1639	1.72	1.85	97	...
TOI-4495.01	1383	3.63	5.18	74	...
TOI-4527.01	1363	0.91	0.40	...	13
TOI-4602.01	1380	2.55	3.98	111	11
TOI-5082.01	1165	2.55	4.24	160	15
TOI-5388.01	601	1.89	2.59	...	12

Note. Empty values for the TSM and ESM columns indicate that the target was not considered best-in-class for transmission or emission spectroscopy, respectively.

There was a subset of targets with high FPP values that could be large grazing planets or systems with a high planetary-to-stellar-radius ratio (R_p/R_*) rather than their current LFP classification. Grazing transits or high- R_p/R_* systems often produce transits that look somewhat V-shaped and can masquerade as a stellar eclipse rather than a planet transit. These scenarios are limiting cases for the validation software since the analyses rely so heavily on transit shape. Therefore, targets with high FPP values that could potentially fall under these categories warrant further follow-up. For our purposes, we keep these targets classified as LFPs not only for the sake of a uniform analysis but also because grazing transits are nonideal candidates for transit and eclipse spectroscopy. However, we flag them here for future study and as examples of the limitations of statistical validation.

A third category of validation emerged for targets with FPP values that did not quite meet the threshold for validation but also were not clear false positives. These 31 targets were deemed to be marginal validations and had at least one or both FPP values from *vespa* and TRICERATOPS that met the marginal validation criteria described in Section 6. This category was further subdivided into “likely planets” (LPs) and “potential false positives” (pFPs). LPs were targets with either both FPP values residing in the marginal validation zone or one FPP in the marginal validation zone and the other meeting the threshold for validation. pFPs were targets with one marginal validation FPP and one FPP that indicates a false positive.

The results of our vetting analysis agree with these distinctions based on FPP. Almost all of the targets in the pFP category had at least one vetting factor that could indicate a false-positive origin (e.g., V-shaped transit, possible odd-even transit depth differences, etc.) but are not definitive enough to warrant labeling the target a likely false positive. There were a total of 13 targets in the LP category and 18 in the pFP category of marginal validations. We encourage future study and follow-up of these targets to ascertain their true

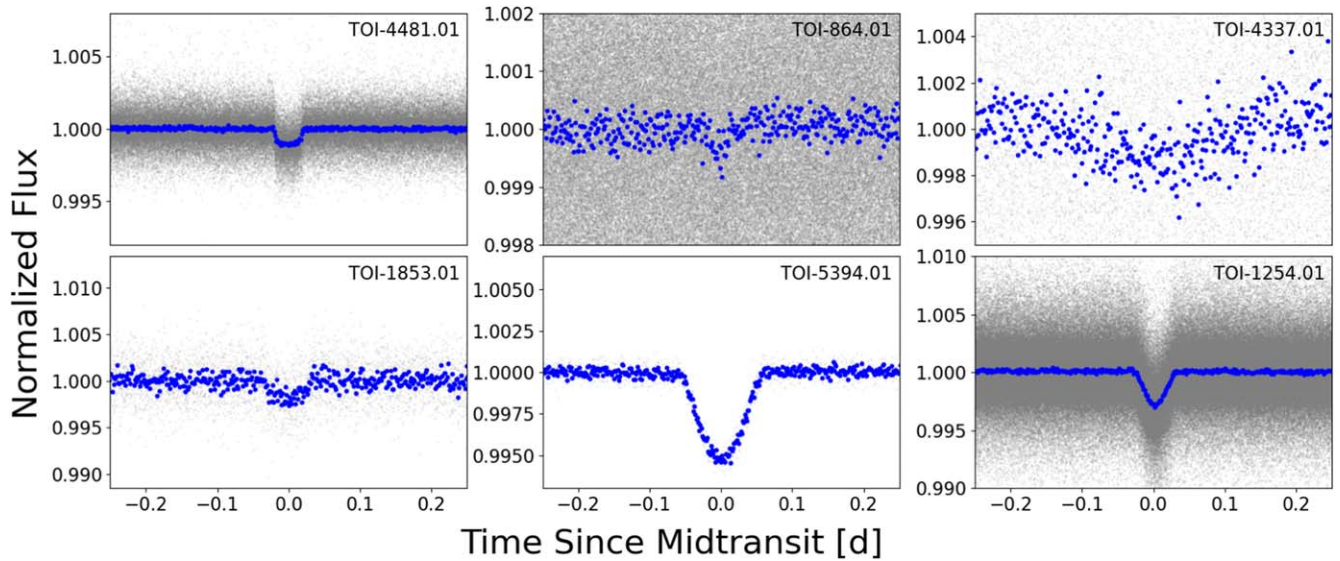


Figure 6. Examples of transits from targets in each disposition category. Left column: examples of validated planets. Both transits are well-defined with flat bottoms. Middle column: examples of marginal validations; a likely planet (top) and a potential false positive (bottom). These targets either have a low S/N or a transit shape that can be confused with an EB and cannot be validated but are also not clear false positives. Right column: examples of likely false positives. These targets either have a very obvious V-shape, otherwise non-transit-shaped feature, or have been deemed likely false positives during vetting (e.g., a large centroid offset).

nature as they could potentially be prime targets for atmospheric characterization with JWST. Examples of transits from each disposition category are shown in Figure 6.

The remaining four targets produced inconclusive vetting and validation results. This category is distinct from marginal validations in that in most of these inconclusive cases *vespa* and *TRICERATOPS* disagree significantly on the status of each target or there are additional factors precluding an adequate vetting or validation analysis. The targets TOI-1355.01, TOI-1954.01, and TOI-4552.01 were validated by one statistical-validation software while the other software produced an FPP that did not meet the threshold for even a marginal validation.

In the case of TOI-1355.01, the discrepant FPPs may be due to overly constraining photometric follow-up observations. The transit shape is slightly V-shaped, and our follow-up observations rule out a large portion of parameter EB and BEB parameter space, but those are the models that fit the phase-folded transit the best (resulting in FPP values with large uncertainties from *TRICERATOPS*). This target may be a grazing planet, which would explain the V-shape as well as the small parameter space for EBs and BEBs.

In the case of TOI-1954.01, very little follow-up exists and the target is in a crowded field, both of which likely combine to cause the discrepancy between *vespa* and *TRICERATOPS*. For TOI-4552.01, the signal is shallow and the light curve exhibits some variability, which is likely causing variability in the FPP values calculated by the different validation software packages.

The final inconclusive case is TOI-4597.01. This target was statistically validated by *vespa* but *TRICERATOPS* was unable to run on it. This is likely due to the short periodic oscillations that appear in the light curve as a result of stellar activity or variability. A clear transit exists, but we are unable to complete our vetting and validation analysis without properly modeling the variability in the light curve to produce a clean transit. This is beyond the scope of this work as it would require a physically motivated model to subtract from the light curve that our vetting and validation procedure is

incapable of. We encourage follow-up analysis of these four inconclusive targets to determine their true nature.

There were an additional 21 targets from our samples that were confirmed by independent teams over the course of our analysis. These targets are TOI-179 b (Desidera et al. 2023; de Leon et al. 2023), TOI-238 b (Mascareño et al. 2024), TOI-332 b (Osborn et al. 2023), TOI-622 b (Psaridi et al. 2023), TOI-836 b (Hawthorn et al. 2023), TOI-969 b (Lillo-Box et al. 2023), TOI-1099 b (Barros et al. 2023), TOI-1194 b (Wang et al. 2023), TOI-1347 b (Rubenzahl et al. 2024), TOI-1468 b & c (Chaturvedi et al. 2022), TOI-1853 b (Naponiello et al. 2023), TOI-2134 b (Rescigno et al. 2024), TOI-3235 b (Hobson et al. 2023), TOI-3884 b (Almenara et al. 2022), TOI-4463 A b (Yee et al. 2023), GJ 806 b (TOI-4481b; Palles et al. 2023), HD 20329 b (TOI-4524b; Murgas et al. 2022), TOI-4641 b (Bieryla et al. 2024), TOI-4860 b (Almenara et al. 2024; Triaud et al. 2023), and Wolf 327 b (TOI-5727 b; Murgas et al. 2024). This high number of targets in our best-in-class sample being confirmed in such a short period of time is very positive for the prospects for atmospheric characterization with JWST. Indeed, the goal of our synthesis of the best-in-class sample is to highlight and elevate targets potentially well suited to such observations for follow-up to measure their masses and confirm their planetary nature.

For the targets that had masses measured independently over the course of our analysis, we recalculated their TSM and ESM values according to their updated planet parameters and reranked them within their respective bins. In the cases of TOI-179 b, TOI-238 b, TOI-332 b (Osborn et al. 2023), TOI-836 b, TOI-969 b, TOI-1099 b, TOI-1194 b, TOI-1347 b, TOI-1853 b, TOI-2134 b, TOI-3235 b, TOI-4463 A b, TOI-4641 b, and TOI-4860 b, the updated parameters differed significantly from those originally listed on the NASA Exoplanet Archive, resulting in either TSM and/or ESM values much lower than originally calculated or placement into a different parameter space bin where they no longer ranked within the top five targets. In either case, this resulted in removal from either the best-in-class transmission or emission spectroscopy samples. In

the cases of TOI-238 b, TOI-836 b, TOI-969 b, TOI-1099 b, TOI-1347 b, TOI-1853 b, TOI-2134 b, TOI-4463 A b, and TOI-4641 b, this amounted to removal from the entire best-in-class sample.

Our best-in-class sample also includes seven targets with ambiguous periods: TOI-706.01, TOI-1856.01, TOI-1895.01, TOI-2299.01, TOI-4317.01, TOI-5575.01, and TOI-5746.01. These targets were originally discovered as single transits before transiting again in later sectors of TESS data. The periods reported on ExoFOP represent the upper limit on their periods since additional transits of these targets could have fallen in gaps in the TESS data and their true periods may be shorter. We performed our vetting and validation using the stated periods but knowing that future observations could reveal shorter periods that would alter the TSM and ESM values as well as their observability with JWST. We choose not to discard these targets from our best-in-class samples to emphasize their potential as ideal JWST targets and emphasize the need for additional follow-up on them. Only TOI-4317.01 had low enough FPP values to be considered statistically validated, but due to its ambiguous period we place it in the LP category, and we caution that a deeper analysis is required for this target to identify the true period and therefore its true planetary status.

We note that the planets with long or ambiguous periods in our sample should have their orbital periods further scrutinized as the TESS observing strategy makes it difficult to determine such long orbital periods and they may change depending on individual circumstances. Should these targets be shown to be true planets on shorter periods, their status in the best-in-class sample is not likely to change. This is because they are all members of the transmission spectroscopy best-in-class sample and a shorter period will increase their T_{eq} , therefore increasing their TSM value.

The final best-in-class sample is displayed in Figure 7, which mirrors Figure 4 but now includes updated dispositions for all targets in our samples, both confirmed and unconfirmed.¹²⁸ Additional information on each target can be found in Table 4 in Appendix A. An extended machine-readable version of this table is also available in the online version of this article. We also include an updated version of Figure 4 reflecting the new dispositions of the sample. This can be found in Figure 8.

There were a number of targets in our best-in-class sample that are also in the process of being validated by independent teams. These include TOI-4226.01 (M. Timmermans 2024, in preparation) and TOI-4317.01 (H. Osborn et al. 2024, in preparation). We direct the reader to these upcoming publications for a more in-depth analysis and exploration than is available here and to treat such in-depth analyses as the definitive discovery papers for these individual targets. C. Dressing et al. (2024, in preparation) is also conducting a parallel large-scale validation effort on TOIs 261.01, 4317.01, 4527.01, 4602.01, and 5082.01, as is Mistry et al. (2023) for TOI-771.01, and we direct the reader to this upcoming publication for an additional, independent vetting and validation of these targets. Additionally, independent teams are conducting confirmation and characterization of TOI-1410.01 (J. Livingston 2024, in preparation; A. S. Polanski 2024, in preparation) and TOI-880.02 (L. D. Nielsen 2024, in

preparation), and we direct the reader to these papers for an in-depth analysis of these targets.

8. Summary and Conclusion

In this paper, we present a set of best-in-class planets for atmospheric characterization with JWST through both transmission and emission spectroscopy. Our vetting, validation, and results are summarized here:

1. We queried the NASA Exoplanet Archive for all transiting confirmed planets and unconfirmed TESS candidates and calculated their TSM, ESM, and observability with JWST.
2. We divided all planets into grids with bins in equilibrium temperature from 100 to 3000 K and planetary radius from 0.3 to $25.0 R_{\oplus}$, and the top five planets and candidates were ranked by spectroscopy metric in each bin to create a best-in-class sample for each spectroscopy method.
3. The 103 unconfirmed TESS-discovered candidates from the transmission and emission spectroscopy grids were vetted using a combination of follow-up observations collected by TFOP and independent analyses such as the SPOC DV reports.
4. We used `vespa` and `TRICERATOPS` to calculate the FPPs and determine a final disposition for each target.
5. Our analysis resulted in 18 validated targets, 29 likely false positives, 31 targets that were marginally validated, and four inconclusive validations. Of our original targets, 21 were independently confirmed over the course of our analysis.
6. This final sample represents the best-in-class targets for atmospheric characterization with JWST, and deeper analysis on each target is highly encouraged.

The best-in-class sample presented in this paper is meant to represent an initial look at many of the targets with the potential to yield high-quality spectra from JWST. We hope that this work paves the way for future studies of a similar sort. We highly encourage independent analysis of each target presented here to discern the true nature of each and build a catalog of planets that can reliably provide exquisite atmospheric data from JWST.

We recognize that this best-in-class sample will undoubtedly change over time as new targets supplant previous ones in the JWST observability rankings, as targets are shown to be false positives, or as the orbital and planetary parameters of targets are refined with further observation. Since the date on which we queried the NASA Exoplanet Archive to generate our sample, ~ 750 new TESS candidates have been discovered. It is possible that anywhere from five to 10 of these new discoveries could possess TSM or ESM values that place them within the best-in-class sample. These targets primarily appear in the bins containing the largest planets and the hottest planets. As TESS probes fainter stars, new detections are even more biased toward large, hot planets as they possess a sufficient S/N to be detected around faint stars.

This sample may also change based on the assumptions used to generate it. Our analysis calculated the ESM value for planets in all portions of parameter space even though it was originally developed by Kempton et al. (2018) for terrestrial planets. Parameter values baked into the ESM quantity such as the day–night heat redistribution on a planet may be different

¹²⁸ The code used to generate this figure can be found at <https://github.com/benhord/best-in-class>.

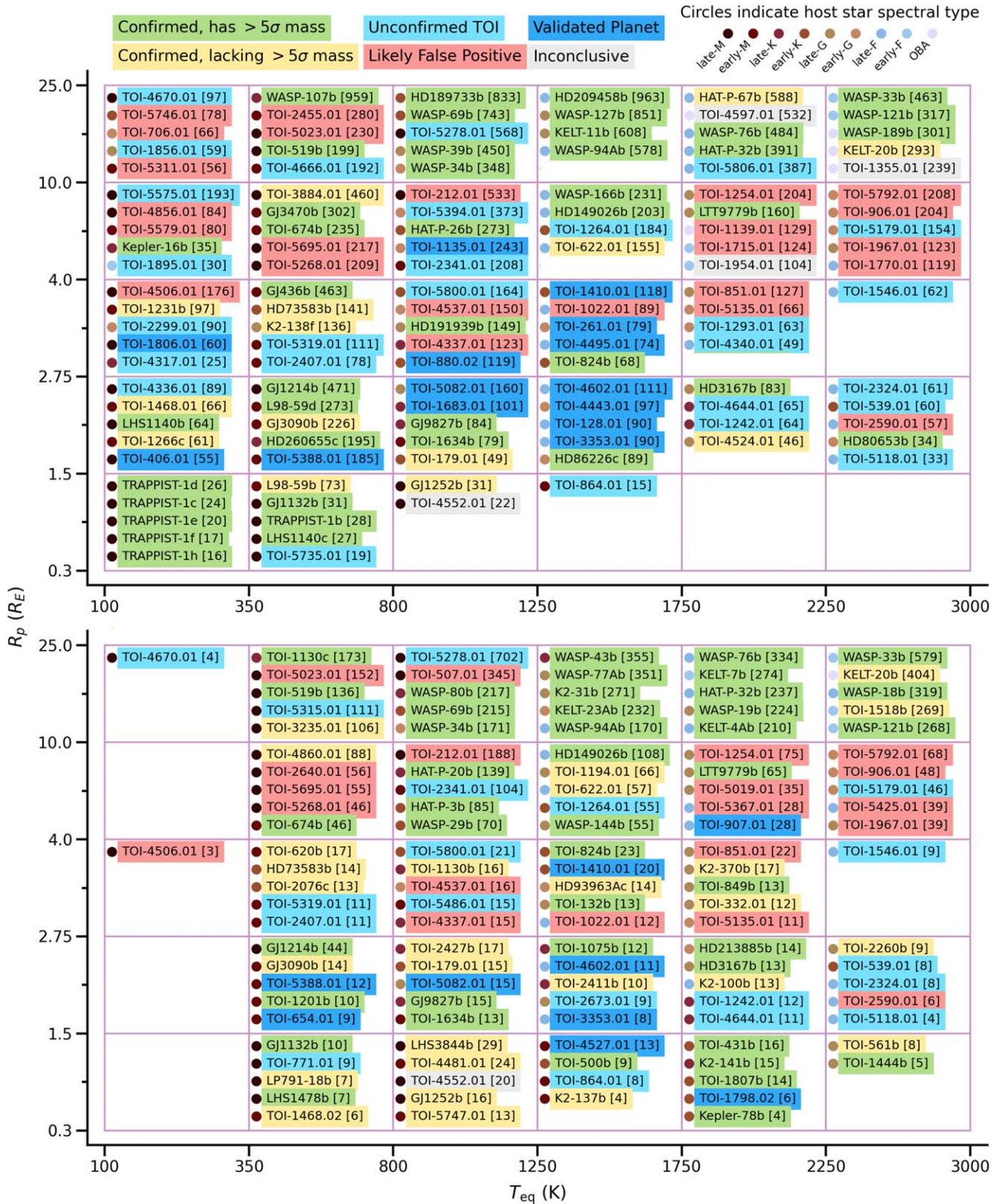


Figure 7. Our best-in-class targets for transmission (top) and emission (bottom) spectroscopy after performing our vetting and validation analysis on the sample. Similar to Figure 4, target names are displayed in the cell corresponding to the parameter space they occupy next to their TSM or ESM value in brackets, with approximate host stellar type denoted by the colored circle, as determined by reported effective temperature. Each target’s background color corresponds to its mass measurement and validation status: green targets are confirmed planets with mass measurements $>5\sigma$, yellow targets are confirmed planets with mass measurements $<5\sigma$ and TOIs that were independently confirmed over the course of our analysis, dark blue targets have been statistically validated by our analysis, light blue targets are marginal validations (LPs and pFPs), red targets were deemed likely false positives (LFPs) by our analysis, and gray targets were deemed to have an inconclusive validation. Targets with an asterisk next to their name have an ambiguous period and their TSM values are liable to change as their T_{eq} values were calculated on the reported periods not the true periods.

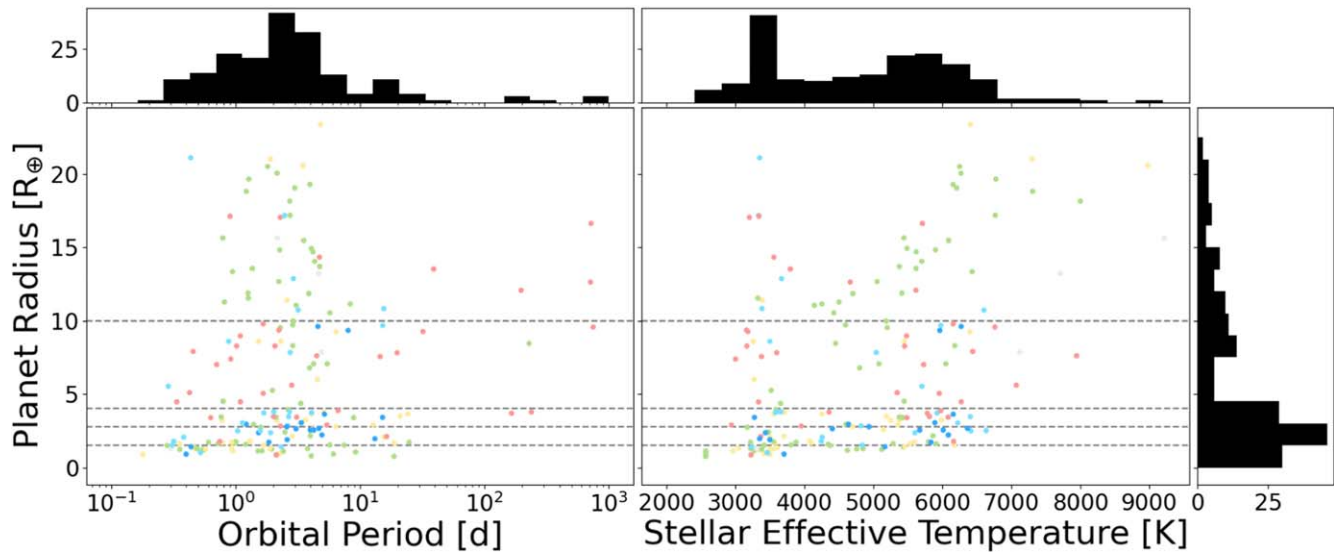


Figure 8. The distribution of targets in our best-in-class samples, similar to Figure 3 but with updated coloring to show final dispositions after our vetting and validation analysis. Left: the orbital periods and planetary radii of the combined TSM and ESM best-in-class samples. Right: the effective temperature of the host stars and the planetary radii of the same combined best-in-class sample. Also shown are the marginal distributions for each variable. The edges of the radius bins are represented by the gray dashed horizontal lines. Points are color-coded according to the categories presented in Figure 7.

from what is assumed by our calculations. However, since our rankings of best-in-class targets are relative to other planets and candidates of similar radius and equilibrium temperature, this factor can likely be ignored. Furthermore, the discrete boundaries of our bins may bias our best-in-class sample toward targets at the hot and large edges of their bins, so different binning schemes may change the specific targets that are contained within the best-in-class sample.

Additionally, it is possible that the thermal emission of planets hotter than ~ 800 K can be observed with NIR instruments rather than with MIRI, as assumed by our analysis. This would open up access to brighter stars due to the favorable ratio between the flux of the planet’s thermal emission and the flux of the star, and would allow for study of a different set of spectral features compared to those available to MIRI. The sample presented here makes parameter cuts for emission spectroscopy based on the performance of MIRI, but a blend of instruments would open up the pool of potential best-in-class targets for the hottest portions of parameter space.

This best-in-class sample may also prove useful for future missions that will study exoplanet atmospheres, such as the upcoming Ariel mission (Tinetti et al. 2018), which will conduct a survey of around one thousand exoplanetary atmospheres. A total of 69 of our best-in-class targets are contained within the Ariel target list described by Edwards & Tinetti (2022). This overlap may grow as both our best-in-class sample and the Ariel target list are updated.

To a first-order approximation, out of 103 total targets originally unconfirmed in our best-in-class sample, 52 of them were either statistically validated, marginally validated and ruled LPs, or were confirmed independently. This suggests that at least $\sim 50\%$ of the TESS candidates analyzed are true planets, although this value may be higher if any of the targets deemed “potential false positive” or “likely false positive” are actually planets.

This sample also demonstrates the power of TESS to discover planets amenable for atmospheric characterization from which we can learn a great deal about their atmospheric structure and composition. Approximately 57% of the targets in

the final best-in-class sample (excluding likely false positives) are TESS discoveries. However, TESS has surprisingly missed the detection of some small planets orbiting small stars, so planet searches beyond TESS are also required (Brady & Bean 2022). It is therefore important to continue searching for planet candidates that could turn out to be excellent targets for atmospheric study since, as shown here, many of the best planets for study with JWST are still being revealed.

Acknowledgments

We thank T. Komacek, D. Richardson, A. Boss, and C. Hartzell for their helpful discussion of this work.

Funding for the TESS mission is provided by NASA’s Science Mission Directorate.

This research has made use of the Exoplanet Follow-up Observation Program (ExoFOP) website (NExSci 2022), which is operated by the California Institute of Technology, under contract with the National Aeronautics and Space Administration under the Exoplanet Exploration Program.

This work has made use of data from the European Space Agency (ESA) mission Gaia (<https://www.cosmos.esa.int/gaia>), processed by the Gaia Data Processing and Analysis Consortium (DPAC, <https://www.cosmos.esa.int/web/gaia/dpac/consortium>). Funding for the DPAC has been provided by national institutions, in particular the institutions participating in the Gaia Multilateral Agreement.

This paper includes data collected by the TESS mission, which are publicly available from the Mikulski Archive for Space Telescopes (MAST) and produced by the Science Processing Operations Center (SPOC) at NASA Ames Research Center. This research effort made use of systematic error-corrected (PDCSAP) photometry. Funding for the TESS mission is provided by NASA’s Science Mission Directorate.

Resources supporting this work were provided by the NASA High-End Computing (HEC) Program through the NASA Advanced Supercomputing (NAS) Division at Ames Research Center for the production of the SPOC data products.

Some/all of the data presented in this paper were obtained from the Mikulski Archive for Space Telescopes (MAST) at the Space Telescope Science Institute. The specific observations analyzed can be accessed via [10.17909/rd5r-m387](https://doi.org/10.17909/rd5r-m387).

This work makes use of observations from the LCOGT network. Part of the LCOGT telescope time was granted by NOIRLab through the Mid-Scale Innovations Program (MSIP). MSIP is funded by NSF.

This paper is based on observations made with the MuSCAT3 instrument, developed by the Astrobiology Center and under financial support by JSPS KAKENHI (grant No. JP18H05439) and JST PRESTO (grant No. JPMJPR1775), at Faulkes Telescope North on Maui, HI, operated by the Las Cumbres Observatory.

This paper makes use of observations made with the MuSCAT2 instrument, developed by the Astrobiology Center, at TCS operated on the island of Tenerife by the IAC in the Spanish Observatorio del Teide.

This paper makes use of data from the MEarth Project, which is a collaboration between Harvard University and the Smithsonian Astrophysical Observatory. The MEarth Project acknowledges funding from the David and Lucile Packard Fellowship for Science and Engineering, the National Science Foundation under grant Nos. AST-0807690, AST-1109468, AST-1616624 and AST-1004488 (Alan T. Waterman Award), the National Aeronautics and Space Administration under grant No. 80NSSC18K0476 issued through the XRP Program, and the John Templeton Foundation.

C.M. would like to gratefully acknowledge the entire Dragonfly Telephoto Array team, and Bob Abraham in particular, for allowing their telescope bright time to be put to use observing exoplanets.

B.J.H. acknowledges support from the Future Investigators in NASA Earth and Space Science and Technology (FINESST) program (grant No. 80NSSC20K1551) and support by NASA under grant No. 80GSFC21M0002.

K.A.C. and C.N.W. acknowledge support from the TESS mission via subaward s3449 from MIT.

This research made use of Lightkurve, a Python package for Kepler and TESS data analysis (Lightkurve Collaboration et al. 2018).

Some of the data presented herein were obtained at the W. M. Keck Observatory, which is operated as a scientific partnership among the California Institute of Technology, the University of California, and the National Aeronautics and Space Administration. The Observatory was made possible by the generous financial support of the W. M. Keck Foundation. The authors wish to recognize and acknowledge the very significant cultural role and reverence that the summit of Maunakea has always had within the indigenous Hawaiian community. We are most fortunate to have the opportunity to conduct observations from this mountain.

D.R.C. and C.A.C. acknowledge support from NASA through the XRP grant No. 18-2XRP18_2-0007. C.A.C. acknowledges that this research was carried out at the Jet Propulsion Laboratory, California Institute of Technology, under a contract with the National Aeronautics and Space Administration (80NM0018D0004).

This research was carried out in part at the Jet Propulsion Laboratory, California Institute of Technology, under a contract with the National Aeronautics and Space Administration (80NM0018D0004).

S.Z. and A.B. acknowledge support from the Israel Ministry of Science and Technology (grant No. 3-18143).

The research leading to these results has received funding from the ARC grant for Concerted Research Actions, financed by the Wallonia-Brussels Federation. TRAPPIST is funded by the Belgian Fund for Scientific Research (Fond National de la Recherche Scientifique, FNRS) under the grant No. PDR T.0120.21. TRAPPIST-North is a project funded by the University of Liege (Belgium), in collaboration with Cadi Ayyad University of Marrakech (Morocco). M.G. is F.R.S.-FNRS Research Director and E.J. is F.R.S.-FNRS Senior Research Associate. The postdoctoral fellowship of K.B. is funded by F.R.S.-FNRS grant No. T.0109.20 and by the Francqui Foundation.

H.P.O.'s contribution has been carried out within the framework of the NCCR PlanetS supported by the Swiss National Science Foundation under grant Nos. 51NF40_182901 and 51NF40_205606.

F.J.P. acknowledges financial support from the grant No. CEX2021-001131-S funded by MCIN/AEI/ 10.13039/501100011033.

A.J. acknowledges support from ANID—Millennium Science Initiative—ICN12_009 and from FONDECYT project 1210718.

Z.L.D. acknowledges the MIT Presidential Fellowship and that this material is based upon work supported by the National Science Foundation Graduate Research Fellowship under grant No. 1745302.

P.R. acknowledges support from the National Science Foundation grant No. 1952545.

Some of the observations in this paper made use of the High-Resolution Imaging instruments ‘Alopeke and Zorro, and were obtained under Gemini LLP Proposal Number GN/S-2021A-LP-105. ‘Alopeke/Zorro were funded by the NASA Exoplanet Exploration Program and built at the NASA Ames Research Center by Steve B. Howell, Nic Scott, Elliott P. Horch, and Emmett Quigley. Alopeke/Zorro was mounted on the Gemini North/South 8 m telescopes of the international Gemini Observatory, a program of NSF’s NOIRLab, which is managed by the Association of Universities for Research in Astronomy (AURA) under a cooperative agreement with the National Science Foundation, on behalf of the Gemini partnership: the National Science Foundation (United States), National Research Council (Canada), Agencia Nacional de Investigación y Desarrollo (Chile), Ministerio de Ciencia, Tecnología e Innovación (Argentina), Ministério da Ciência, Tecnologia, Inovações e Comunicações (Brazil), and Korea Astronomy and Space Science Institute (Republic of Korea).

This work is partly supported by JSPS KAKENHI grant Nos. JP17H04574, JP18H05439, JP21K20376; JST CREST grant No. JPMJCR1761; and Astrobiology Center SATEL-LITE Research project AB022006.

This article is based on observations made with the MuSCAT2 instrument, developed by ABC, at Telescopio Carlos Sánchez operated on the island of Tenerife by the IAC in the Spanish Observatorio del Teide. This paper is based on observations made with the MuSCAT3 instrument, developed by the Astrobiology Center and under financial supports by JSPS KAKENHI (grant No. JP18H05439) and JST PRESTO (grant No. JPMJPR1775), at Faulkes Telescope North on Maui, HI, operated by the Las Cumbres Observatory.

This publication benefits from the support of the French Community of Belgium in the context of the FRIA Doctoral Grant awarded to M.T.

D.D. acknowledges support from TESS Guest Investigator Program grant Nos. 80NSSC22K1353, 80NSSC22K0185, and 80NSSC23K0769.

A.B. acknowledges the support of M.V. Lomonosov Moscow State University Program of Development.

T.D. was supported in part by the McDonnell Center for the Space Sciences.

V.K. acknowledges support from the youth scientific laboratory project, topic FEUZ-2020-0038.

Facilities: Adams Observatory, ASP, Brierfield Private Observatory, Campo Catino Astronomical Observatory, Catania Astrophysical Observatory, Caucasian Mountain Observatory, CHAT, CROW Observatory, Deep Sky West, Dragonfly, El Sauce, ExTrA, FEROS, Fred L. Whipple Observatory, Gaia, Gemini (‘Alopeke, Zorro), George Mason University, HAT-South, Hazelwood Observatory, Keck, Carlson R. Chambliss Astronomical Observatory (CRCAO) at Kutztown University, LCOGT, Lewin Observatory, Lick Observatory, Lookout Observatory, MASTER-Ural, MEarth-S, Mt. Stuart Observatory, MuSCAT, MuSCAT2, MuSCAT3, Observatori Astronòmic de la Universitat de València, Observatori Astronòmic Albanyà Observatorio del Roque de los Muchachos, Observatory de Ca

l’Ou, Palomar Observatory, PEST, Privat Observatory Herges-Hallenberg, PvDKO, RCO, SAINT-EX, Salerno University Observatory, Solaris SLR2, SPECULOOS, SUTO-Otivar, TESS, TRAPPIST, University of Louisville telescopes at the University of Southern Queensland’s Mt. Kent Observatory and at Mt. Lemmon Observatory, Union College Observatory, Villa ‘39, VLT, WASP, WCO, Wellesley College Whitin Observatory, WIYN.

Software: AstroImageJ, Astropy (Astropy Collaboration et al. 2013, 2018, 2022), astroquery (Ginsburg et al. 2019), BANZAI (McCully et al. 2018), DEATHSTAR (Ross et al. 2024), Jupyter (Kluyver et al. 2016), Lightkurve (Lightkurve Collaboration et al. 2018), matplotlib (Hunter 2007), numpy (Van Der Walt et al. 2011), pandas (McKinney 2010), TESS Transit Finder (Jensen 2013), Tescut (Brasseur et al. 2019), TRICERATOPS (Giacalone & Dressing 2020; Giacalone et al. 2021), VESPA (Morton 2012, 2015).

Appendix A

Full List of Vetted and Validated Best-in-class TOIs

Table 4 shows our final set of best-in-class targets and values for a selection of planetary and stellar parameters as well as their disposition within our sample. Targets that were removed over the course of our analysis are not included.

Table 4

Our Full Best-in-class Sample Including Both the TOIs on Which We Performed Vetting and Validation Analysis and Planets That Were Confirmed Prior to Our Study or Independent of Our Analysis

Planet Name	Period (days)	Radius (R_{\oplus})	Equilibrium Temperature (K)	Semimajor Axis (au)	Stellar Effective Temperature (K)	Stellar Mass (M_{\odot})	TSM	ESM	Disposition
GJ 436 b	2.64	3.96	684	0.029	3586	0.47	463	108	Confirmed
GJ 1132 b	1.63	1.13	578	0.015	3270	0.18	31	10	Confirmed
GJ 1214 b	1.58	2.74	582	0.015	3170	0.18	471	44	Confirmed
GJ 1252 b	0.52	1.19	1048	0.009	3325	0.38	31	16	Confirmed
GJ 3090 b	2.85	2.13	721	0.032	3703	0.52	226	14	Confirmed
GJ 3470 b	3.34	4.36	691	0.036	3652	0.54	302	38	Confirmed
GJ 9827 b	1.21	1.58	1184	0.019	4340	0.61	84	15	Confirmed
HAT-P-3 b	2.90	9.98	1157	0.039	5185	1.06	96	85	Confirmed
HAT-P-20 b	2.88	9.72	972	0.036	4595	0.76	13	139	Confirmed
HAT-P-26 b	4.23	7.06	993	0.048	5079	1.12	273	27	Confirmed
HAT-P-32 b	2.15	20.05	1918	0.034	6269	1.13	391	237	Confirmed
HAT-P-67 b	4.81	23.37	1899	0.065	6406	1.64	588	115	Confirmed
HD 3167 b	0.96	1.63	1772	0.018	5286	0.85	83	13	Confirmed
HD 73583 b	6.40	2.79	743	0.060	4695	0.73	141	14	Confirmed
HD 80653 b	0.72	1.61	2446	0.017	5910	1.18	34	6	Confirmed
HD 86226 c	3.98	2.16	1304	0.049	5863	1.02	89	11	Confirmed
HD 93963 A c	3.65	3.23	1344	0.048	5987	1.11	67	14	Confirmed
HD 149026 b	2.88	8.30	1676	0.043	6179	1.42	203	108	Confirmed
HD 189733 b	2.22	12.67	1201	0.031	5052	0.79	833	1140	Confirmed
HD 191939 b	8.88	3.39	908	0.078	5427	0.81	149	13	Confirmed
HD 209458 b	3.52	15.47	1451	0.049	6091	1.23	963	546	Confirmed
HD 213885 b	1.01	1.75	2068	0.020	5795	1.07	56	14	Confirmed
HD 260655c	5.71	1.53	556	0.047	3803	0.44	195	9	Confirmed
K2-31 b	1.26	11.88	1556	0.022	5412	0.91	120	271	Confirmed
K2-100 b	1.67	1.52	1911	0.030	6168	1.15	3	13	Confirmed
K2-137 b	0.18	0.89	1704	0.006	3492	0.46	19	4	Confirmed
K2-138 f	12.76	2.90	741	0.104	5356	0.94	136	2	Confirmed
K2-141 b	0.28	1.49	2042	0.007	4373	0.71	8	15	Confirmed
K2-370 b	2.14	3.21	1986	0.017	5372	0.98	100	17	Confirmed
KELT-4 A b	2.99	19.04	1823	0.043	6206	1.20	310	210	Confirmed
KELT-7 b	2.73	17.18	2041	0.044	6768	1.76	253	274	Confirmed
KELT-11 b	4.74	13.69	1703	0.063	5375	1.44	608	139	Confirmed
KELT-20 b	3.47	20.58	2331	0.054	8980	1.76	293	404	Confirmed
KELT-23 A b	2.26	14.83	1562	0.033	5899	0.94	283	232	Confirmed
Kepler-16 b	228.78	8.45	206	0.705	4450	0.69	35	0	Confirmed
Kepler-78 b	0.36	1.23	2220	0.009	5121	0.84	7	4	Confirmed

Table 4
(Continued)

Planet Name	Period (days)	Radius (R_{\oplus})	Equilibrium Temperature (K)	Semimajor Axis (au)	Stellar Effective Temperature (K)	Stellar Mass (M_{\odot})	TSM	ESM	Disposition
L 98-59 b	2.25	0.95	623	0.022	3412	0.27	73	5	Confirmed
L 98-59 d	7.45	1.52	416	0.049	3412	0.27	273	4	Confirmed
LHS 1140 b	24.74	1.73	232	0.096	3216	0.19	64	0	Confirmed
LHS 1140 c	3.78	1.28	433	0.027	3216	0.19	27	3	Confirmed
LHS 1478 b	1.95	1.24	595	0.018	3381	0.24	18	7	Confirmed
LHS 3844 b	0.46	1.30	807	0.006	3043	0.15	41	29	Confirmed
LP 791-18 b	0.95	1.12	631	0.010	2960	0.14	19	7	Confirmed
LTT 9779 b	0.79	4.51	1955	0.017	5443	0.77	160	65	Confirmed
TOI-128.01	4.94	2.22	1345	0.054	6086	0.85	90	8	VP
TOI-132 b	2.11	3.42	1513	0.026	5397	0.97	40	13	Confirmed
TOI-179.01	4.14	2.60	969	0.048	5145	0.86	49	15	Confirmed
TOI-212.01	0.34	4.47	1111	0.006	3332	0.29	533	188	LFP
TOI-261.01	3.36	3.04	1722	0.035	5890	0.50	79	10	VP
TOI-332.01	0.78	3.20	1946	0.016	5251	0.88	13	12	Confirmed
TOI-406.01	13.18	1.96	344	0.086	3349	0.48	55	1	VP
TOI-431 b	0.49	1.28	1879	0.011	4850	0.78	16	16	Confirmed
TOI-500 b	0.55	1.17	1683	0.012	4621	0.74	16	9	Confirmed
TOI-507.01	0.90	17.12	875	0.017	3338	0.82	291	345	LFP
TOI-519 b	1.27	11.5	751	0.016	3322	0.34	199	136	Confirmed
TOI-539.01	0.31	1.52	2370	0.008	4836	0.68	60	8	LP
TOI-561 b	0.45	1.42	2371	0.011	5455	0.79	19	8	Confirmed
TOI-620 b	5.10	3.76	604	0.048	3708	0.58	171	17	Confirmed
TOI-622.01	6.40	9.24	1388	0.071	6400	1.31	155	57	Confirmed
TOI-654.01	1.53	2.37	749	0.021	3433	0.53	78	9	VP
TOI-674 b	1.98	5.25	695	0.025	3514	0.42	235	46	Confirmed
TOI-706.01	719.04	16.63	333	1.024	5710	0.28	66	3	LFP
TOI-771.01	2.33	1.40	663	0.013	3231	0.06	18	9	pFP
TOI-824 b	1.39	2.93	1254	0.022	4600	0.71	68	23	Confirmed
TOI-849 b	0.77	3.44	1975	0.016	5374	0.93	21	13	Confirmed
TOI-851.01	0.63	3.39	1954	0.014	5485	0.94	127	22	LFP
TOI-864.01	0.52	1.00	1272	0.007	3460	0.16	15	8	LP
TOI-880.02	2.57	2.78	1163	0.034	4935	0.81	119	15	VP
TOI-906.01	1.66	5.05	2450	0.019	5955	0.36	204	48	LFP
TOI-907.01	4.58	9.62	1847	0.055	6272	1.07	91	28	VP
TOI-1022.01	3.10	3.43	1715	0.041	6084	0.98	89	12	LFP
TOI-1075 b	0.60	1.79	1325	0.012	3875	0.60	25	12	Confirmed
TOI-1130 b	4.07	3.65	810	0.044	4250	0.68	127	16	Confirmed
TOI-1130 c	8.35	11.14	638	0.071	4250	0.68	106	173	Confirmed
TOI-1135.01	8.03	9.34	1074	0.082	5963	1.16	243	51	VP
TOI-1139.01	4.48	7.61	2013	0.066	7947	1.93	129	24	LFP
TOI-1194.01	2.31	8.60	1391	0.034	5446	1.01	84	66	Confirmed
TOI-1201 b	2.49	2.42	703	0.029	3476	0.51	95	10	Confirmed
TOI-1231 b	24.25	3.65	330	0.129	3553	0.48	97	2	Confirmed
TOI-1242.01	0.38	2.06	1825	0.009	4255	0.66	64	12	LP
TOI-1254.01	1.02	8.27	1968	0.019	5451	0.95	204	75	LFP
TOI-1264.01	2.74	7.84	1260	0.036	5040	0.83	184	55	pFP
TOI-1266 c	18.80	1.67	348	0.106	3573	0.45	61	0	Confirmed
TOI-1293.01	1.68	3.71	1785	0.028	5923	1.08	63	10	pFP
TOI-1355.01	2.17	15.62	2900	0.043	9218	2.32	239	148	Inconclusive
TOI-1410.01	1.22	2.94	1396	0.020	4635	0.72	118	20	VP
TOI-1444 b	0.47	1.40	2324	0.012	5430	0.93	5	5	Confirmed
TOI-1468.01	15.53	2.64	337	0.086	3496	0.34	66	1	Confirmed
TOI-1468.02	1.28	1.45	682	0.021	3496	0.34	10	6	Confirmed
TOI-1518 b	1.90	21.02	2492	0.039	7300	1.79	197	269	Confirmed
TOI-1546.01	1.13	3.03	2357	0.023	6223	1.21	62	9	pFP
TOI-1634 b	0.99	1.75	924	0.015	3550	0.50	79	13	Confirmed
TOI-1683.01	3.06	2.64	929	0.037	4402	0.69	101	12	VP
TOI-1715.01	2.83	5.61	1962	0.046	7072	1.58	124	22	LFP
TOI-1770.01	1.09	4.47	2447	0.022	6273	1.21	119	24	LFP
TOI-1798.02	0.44	1.41	2122	0.011	5165	0.86	8	6	VP
TOI-1806.01	15.15	3.41	337	0.088	3272	0.39	60	1	VP
TOI-1807 b	0.55	1.26	2098	0.008	4757	0.75	16	14	Confirmed
TOI-1856.01	197.03	12.07	332	0.663	5616	1.00	59	1	pFP
TOI-1895.01	748.07	9.57	276	1.921	6762	1.69	30	0	LP
TOI-1954.01	4.90	7.87	1815	0.071	7120	1.97	104	23	Inconclusive
TOI-1967.01	0.43	5.09	2981	0.011	5343	1.03	123	39	LFP
TOI-2076 c	21.02	3.50	735	0.109	5187	0.82	169	13	Confirmed
TOI-2260 b	0.35	1.62	2627	0.010	5534	0.99	74	9	Confirmed
TOI-2299.01	165.02	3.69	325	0.513	5780	0.66	90	1	pFP
TOI-2324.01	1.04	2.49	2560	0.022	6413	1.30	61	8	LP

Table 4
(Continued)

Planet Name	Period (days)	Radius (R_{\oplus})	Equilibrium Temperature (K)	Semimajor Axis (au)	Stellar Effective Temperature (K)	Stellar Mass (M_{\odot})	TSM	ESM	Disposition
TOI-2341.01	0.88	8.59	1075	0.015	3495	0.61	208	104	pFP
TOI-2407.01	2.70	3.79	718	0.031	3596	0.52	78	11	LP
TOI-2411 b	0.78	1.68	1358	0.014	4099	0.65	69	10	Confirmed
TOI-2427 b	1.31	1.80	1114	0.020	4072	0.64	131	17	Confirmed
TOI-2455.01	4.72	14.33	576	0.043	3553	0.49	280	83	LFP
TOI-2590.01	0.75	1.78	2425	0.017	6162	1.17	57	6	LFP
TOI-2640.01	0.91	7.39	705	0.012	2999	0.25	179	56	LFP
TOI-2673.01	1.91	2.37	1739	0.030	5601	0.97	70	9	LP
TOI-3235.01	2.59	11.40	604	0.027	3389	0.39	162	106	Confirmed
TOI-3353.01	4.67	2.67	1264	0.060	6365	1.33	90	8	VP
TOI-3884.01	4.54	6.00	462	0.035	3269	0.28	460	24	Confirmed
TOI-4317.01	238.85	3.78	240	0.662	4354	0.68	25	0	LP
TOI-4336.01	16.34	2.11	318	0.085	3365	0.31	89	1	LP
TOI-4337.01	2.29	2.82	880	0.029	3953	0.62	123	15	LFP
TOI-4340.01	2.67	3.46	1832	0.041	6406	1.28	49	6	LP
TOI-4443.01	1.85	1.72	1639	0.030	5834	1.05	97	8	VP
TOI-4481.01	0.93	1.33	942	0.014	3600	0.41	44	24	Confirmed
TOI-4495.01	5.18	3.63	1383	0.062	6156	1.17	74	9	VP
TOI-4506.01	5.41	2.89	332	0.034	2938	0.17	176	3	LFP
TOI-4524.01	0.93	1.72	2140	0.018	5596	1.01	46	10	Confirmed
TOI-4527.01	0.40	0.91	1363	0.008	3702	0.48	32	13	VP
TOI-4537.01	6.66	3.87	1115	0.071	5975	1.10	150	16	LFP
TOI-4552.01	0.30	1.28	1128	0.006	3304	0.27	22	20	Inconclusive
TOI-4597.01	4.67	13.23	1801	0.067	7712	1.83	532	145	Inconclusive
TOI-4602.01	3.98	2.55	1380	0.051	6012	1.12	111	11	VP
TOI-4644.01	0.32	1.78	1989	0.008	4242	0.66	65	11	LP
TOI-4666.01	2.91	12.87	744	0.033	3666	0.58	192	76	LP
TOI-4670.01	15.50	10.83	334	0.086	3382	0.35	97	4	pFP
TOI-4856.01	14.49	7.56	339	0.080	3376	0.33	84	3	LFP
TOI-4860.01	1.52	8.58	695	0.018	3255	0.34	180	88	Confirmed
TOI-5019.01	1.09	8.97	1970	0.020	5479	0.97	94	35	LFP
TOI-5023.01	2.27	17.05	581	0.023	3199	0.30	230	152	LFP
TOI-5082.01	4.24	2.55	1165	0.051	5670	1.00	160	15	VP
TOI-5118.01	1.57	2.51	2331	0.030	6635	1.39	33	4	pFP
TOI-5135.01	2.02	3.47	2093	0.032	5810	1.04	66	11	LFP
TOI-5179.01	0.29	5.53	2997	0.009	5702	1.02	154	46	pFP
TOI-5268.01	2.07	8.27	585	0.021	3162	0.29	209	46	LFP
TOI-5278.01	0.44	21.09	1111	0.008	3349	0.36	568	702	pFP
TOI-5311.01	39.05	13.53	345	0.196	3793	0.66	56	3	LFP
TOI-5315.01	2.47	17.17	643	0.027	3333	0.43	162	111	pFP
TOI-5319.01	4.08	3.75	602	0.039	3580	0.49	111	11	pFP
TOI-5367.01	1.66	9.79	1792	0.029	6155	1.18	88	28	LFP
TOI-5388.01	2.59	1.89	601	0.024	3495	0.29	185	12	VP
TOI-5394.01	15.19	9.68	847	0.124	5977	1.10	373	62	pFP
TOI-5425.01	0.46	7.91	2860	0.013	6439	1.29	114	39	LFP
TOI-5486.01	2.02	3.79	818	0.026	3654	0.54	87	15	LP
TOI-5575.01	32.07	9.26	219	0.197	3176	0.21	193	0	pFP
TOI-5579.01	19.86	7.82	346	0.108	3595	0.43	80	3	LFP
TOI-5695.01	2.22	9.36	596	0.023	3157	0.35	217	55	LFP
TOI-5735.01	2.12	0.86	528	0.018	3222	0.18	19	2	pFP
TOI-5746.01	711.76	12.63	162	1.411	4662	0.74	78	0	LFP
TOI-5747.01	0.57	1.24	996	0.010	3542	0.41	13	13	Confirmed
TOI-5792.01	0.70	7.01	2327	0.016	5726	1.03	208	68	LFP
TOI-5800.01	2.63	2.83	1133	0.034	4821	0.79	164	21	pFP
TOI-5806.01	3.19	10.72	1801	0.047	6602	1.38	387	118	pFP
TRAPPIST-1 b	1.51	1.12	397	0.012	2566	0.09	28	4	Confirmed
TRAPPIST-1 c	2.42	1.10	340	0.016	2566	0.09	24	2	Confirmed
TRAPPIST-1 d	4.05	0.79	286	0.022	2566	0.09	26	0	Confirmed
TRAPPIST-1 e	6.10	0.92	250	0.029	2566	0.09	20	0	Confirmed
TRAPPIST-1 f	9.21	1.05	218	0.038	2566	0.09	17	0	Confirmed
TRAPPIST-1 h	18.77	0.76	172	0.062	2566	0.09	16	0	Confirmed
WASP-18 b	0.94	13.35	2438	0.020	6432	1.29	25	319	Confirmed
WASP-19 b	0.79	15.64	2047	0.017	5440	0.96	156	224	Confirmed
WASP-29 b	3.92	6.79	973	0.046	4800	0.77	97	70	Confirmed
WASP-33 b	1.22	18.82	2735	0.024	7308	1.50	463	579	Confirmed
WASP-34 b	4.32	14.04	1160	0.052	5700	0.96	348	171	Confirmed
WASP-39 b	4.06	14.93	1150	0.049	5485	0.93	450	98	Confirmed
WASP-43 b	0.81	11.28	1465	0.014	4500	0.58	103	355	Confirmed
WASP-69 b	3.87	11.85	959	0.045	4700	0.98	743	215	Confirmed
WASP-76 b	1.81	20.51	2182	0.033	6250	1.46	484	334	Confirmed

Table 4
(Continued)

Planet Name	Period (days)	Radius (R_{\oplus})	Equilibrium Temperature (K)	Semimajor Axis (au)	Stellar Effective Temperature (K)	Stellar Mass (M_{\odot})	TSM	ESM	Disposition
WASP-77 A b	1.36	13.56	1720	0.023	5617	0.90	188	351	Confirmed
WASP-80 b	3.07	11.05	824	0.034	4143	0.58	295	217	Confirmed
WASP-94 A b	3.95	19.28	1498	0.055	6153	1.67	578	170	Confirmed
WASP-107 b	5.72	10.54	733	0.055	4425	0.68	959	93	Confirmed
WASP-121 b	1.27	19.65	2454	0.026	6776	1.36	317	268	Confirmed
WASP-127 b	4.18	14.70	1422	0.048	5620	0.95	851	138	Confirmed
WASP-144 b	2.28	9.53	1269	0.032	5200	0.81	69	55	Confirmed
WASP-166 b	5.44	7.06	1273	0.064	6050	1.19	231	36	Confirmed
WASP-189 b	2.72	18.15	2638	0.051	8000	2.03	301	378	Confirmed

Notes. In the disposition column, VP = validated planet, LP = likely planet, pFP = possible false positive, LFP = likely false positive. See Section 7 for a further explanation of each disposition and their definitions. Bolding in the TSM and ESM columns denotes membership in the best-in-class sample for transmission and emission spectroscopy, respectively. For an extended, machine-readable version of this table with additional parameters, please see the online version of this article. (This table is available in its entirety in machine-readable form.)

Appendix B

List of TFOP Observations Used in Vetting and Validation of the Best-in-class Sample

Table 5 contains information on all of the publicly available TFOP observations that were used in the synthesis of the reconnaissance photometry and spectroscopy dispositions incorporated into our vetting and validation analysis. We note that no photometry or spectroscopy data were used directly, only the synthesized dispositions created for each target by TFOP's SG1 and SG2. Also contained in Table 5 is information on the high-resolution imaging that was used as observational constraints in our statistical-validation analysis. A further overview of how these dispositions and follow-up observations were used can be found in Sections 5 and 6.

It is important to note that not included in this table are observations that are not publicly available on ExoFOP (see footnote 127). This may be because the observations are currently within a proprietary period, contained within a private archive (e.g., an archive accessible only to members of a specific

collaboration), or the observing team decided not to post their observations publicly. However, there was a subset of observations which fall under this category that were communicated to the TFOP subgroup leads for use in the synthesis of dispositions and were therefore indirectly utilized by our analysis, but cannot be listed here as they were not made public on ExoFOP. These include observations from HARPS-N (TOI-261.01, TOI-1683.01, TOI-5082.01), PFS (TOI-261.01), MINERVA-Australis (TOI-261.01), CHIRON (TOI-1895.01), the Network of Robotic Echelle Spectrographs (NRES; TOI-3353.01, TOI-5082.01), CORALIE (TOI-3353.01), and Keck/HIRES (TOI-1683.01). We direct the reader to these teams for further information on the observations obtained by these instruments that are not publicly available on ExoFOP.

Furthermore, not every observation that is currently posted on ExoFOP was utilized in the synthesis of TFOP dispositions for each target. This is because an observer needs to submit their observations to the respective subgroup in an opt-in fashion for the observations to be used in the synthesis of TFOP dispositions.

Table 5

Follow-up Observations Used in Synthesis of TFOP Dispositions That Were Incorporated into Our Vetting and Validation Analysis

TOI	Telescope	Camera/ Instrument	Filter/ Bandpass	Observation Date
SG1 Photometry				
128.01	LCO CTIO	SBIG 0.4 m	<i>ip</i>	11/14/18
	Solaris SLR2	Andor iKon-L	<i>V</i>	9/20/18
	LCO SSO	Sinistro	<i>zs</i>	10/15/18
	LCO SSO	SBIG 0.4 m	<i>ip</i>	1/12/19
212.01	El Sauce	SBIG STT-1603-3	Unfiltered	11/16/18
	Hazelwood Observatory	STT-3200	<i>Rc</i>	11/17/18
	PEST	ST-8XME	<i>Ic</i>	11/23/18
	InfraRed Survey Facility	SIRIUS	<i>J, H, Ks</i>	11/15/18
	KELT South	Apogee Instruments AP16E	Kodak Wratten No. 8 (Rk)	4/26/10
	TRAPPIST-South	FLI ProLine PL3041-BB	<i>z</i>	11/27/18
	El Sauce	SBIG STT-1603-3	<i>Ic</i>	12/1/18
⋮				
SG2 Spectroscopy				
128.01	SMARTS	CHIRON	4500–8900 Å	2/15/19
	SMARTS	CHIRON	4500–8900 Å	4/7/19
	SMARTS	CHIRON	4500–8900 Å	1/7/21
179.01	SMARTS	CHIRON	4500–8900 Å	2/18/19
	SMARTS	CHIRON	4500–8900 Å	8/13/19
	SMARTS	CHIRON	4500–8900 Å	2/2/20
	SMARTS	CHIRON	4500–8900 Å	2/5/20
	SMARTS	CHIRON	4500–8900 Å	2/10/20
	SMARTS	CHIRON	4500–8900 Å	12/21/20
238.01	FLWO	TRES	3850–9096 Å	12/20/18
	SMARTS	CHIRON	4500–8900 Å	5/23/19
⋮				
SG3 High-resolution Imaging				
128.01	VLT	NaCo	<i>Brγ</i>	12/16/18
	Gemini	DSSI	<i>R</i>	10/31/18
179.01	Gemini	Zorro	562 nm	9/12/19
	Gemini	Zorro	832 nm	9/12/19
	Gemini	Zorro	562 nm	1/12/20
	Gemini	Zorro	832 nm	1/12/20
212.01	VLT	NaCo	<i>Ks</i>	1/25/19
	Gemini	Zorro	562 nm	10/8/22
	Gemini	Zorro	832 nm	10/8/22
	Gemini	Zorro	562 nm	7/29/22
	Gemini	Zorro	832 nm	7/29/22
⋮				

Note. A full, machine-readable version of this table is available in the online version of this article.

(This table is available in its entirety in machine-readable form.)

Appendix C

Descriptions of Select TFOP Follow-up Observatories

In this section, we include longer descriptions of some of the observatories used to obtain follow-up observations that were incorporated into our analysis. For descriptions on how the follow-up observations were used in our vetting and validation analysis of the unconfirmed TOIs in our sample, see Sections 5 and 6.

C.1. Ground-based Photometry

C.1.1. Adams Observatory

Adams Observatory is located at Austin College in Sherman, TX. The 0.6 m telescope is equipped with a FLI Proline PL16803 detector that has an image scale of $0''.38 \text{ pixel}^{-1}$, resulting in a $26' \times 26'$ field of view.

C.1.2. ASP

The Acton Sky Portal (ASP) private observatory is in Acton, MA, USA. The 0.36 m telescope is equipped with an SBIG Aluma CCD4710 camera having an image scale of $1'' \text{ pixel}^{-1}$, resulting in a $17'.1 \times 17'.1$ field of view.

C.1.3. Brierfield Private Observatory

The Brierfield Observatory is located near Bowral, New South Wales, Australia. The 0.36 m telescope is equipped with a 4096×4096 Moravian 16803 camera with an image scale of $0''.74 \text{ pixel}^{-1}$, resulting in a $50' \times 50'$ field of view.

C.1.4. Campo Catino Astronomical Observatory

The Campo Catino Astronomical Observatory (OACC) is located in Guarcino, Italy, and is equipped with a 0.8 m RC telescope and a remote 0.6 m CDK telescope located in El Sauce, Chile. In this work, iTelescope T17 was used, which is a 0.43 m CDK telescope located at Siding Spring Observatory, equipped with a FLI PL4710 CCD camera, providing a field of view of $15'.5 \times 15'.5$ and an image scale of $0''.92 \text{ pixel}^{-1}$.

C.1.5. Catania Astrophysical Observatory

The 0.91 m telescope at Catania Astrophysical Observatory is located in Catania, Italy. The custom-built 1024×1024 detector uses a KAF1001E CCD with an image scale of $0''.66 \text{ pixel}^{-1}$, resulting in a $11'.2 \times 11'.2$ field of view.

C.1.6. CMO

The Caucasian Mountain Observatory (CMO SAI MSU) houses a 0.6 m telescope (RC600) and is located near Kislovodsk, Russia (Berdnikov et al. 2020). RC600 is equipped with an Andor iKon-L BV detector that has an image scale of $0''.67 \text{ pixel}^{-1}$, resulting in a $22' \times 22'$ field of view.

C.1.7. CHAT

The 0.7 m Chilean-Hungarian Automated Telescope (CHAT) telescope is located at Las Campanas Observatory, in Atacama, Chile. Image calibration and photometric data were extracted using standard calibration and reduction steps and by a custom pipeline which implements bias, dark, and flat-field corrections.

C.1.8. CRCAO

The 0.6 m telescope at the Carlson R. Chambliss Astronomical Observatory (CRCAO) at Kutztown University is located near Kutztown, PA. The SBIG STXL-6303E detector has an image scale of $0''.76 \text{ per } 2 \times 2 \text{ binned pixel}$, resulting in a $13' \times 19'.6$ field of view.

C.1.9. CROW Observatory

The 0.36 m telescope CROW Observatory is located in Portalegre, Portugal. It is equipped with a SBIG ST-10XME (KAF3200ME) detector that has an image scale of $0''.66 \text{ pixel}^{-1}$, resulting in a $24' \times 17'$ field of view.

C.1.10. Deep Sky West

Deep Sky West is an Observatory in Rowe, NM. The 0.5 m telescope is equipped with an Apogee U16M detector that has an image scale of $1''.09 \text{ pixel}^{-1}$, resulting in a $37' \times 37'$ field of view.

C.1.11. Dragonfly

The Dragonfly Telephoto Array is a remote telescope consisting of an array of small telephoto lenses roughly equivalent to a 1.0 m refractor housed at the New Mexico Skies telescope hosting facility, near Mayhill, NM, USA. Dragonfly uses SBIG STF8300M detectors that have an image scale of $2''.85 \text{ pixel}^{-1}$, resulting in a $156' \times 114'$ field of view. The data were reduced and analyzed with a custom differential aperture photometry pipeline designed for multicamera image processing and analysis.

C.1.12. El Sauce

The Evans 0.36 m Planewave telescope is located at the El Sauce Observatory in Coquimbo Province, Chile. The telescope is equipped with a 1536×1024 pixel SBIG STT-1603-3 detector. The image scale is $1''.47$ per 2×2 binned pixel, resulting in a $18'.8 \times 12'.5$ field of view.

C.1.13. ExTrA

The Exoplanets in Transits and their Atmospheres (ExTrA) is sited at the ESO La Silla Observatory in Chile and consists of an array of three 0.6 m telescopes. Image data were calibrated and photometric data were extracted using a custom pipeline described in Bonfils et al. (2015).

C.1.14. Fred L. Whipple Observatory

The Fred Lawrence Whipple Observatory houses a 1.2 m telescope and is located on Mt. Hopkins in Amado, AZ. The Fairchild CCD 486 detector has an image scale of $0''.672$ per 2×2 binned pixel, resulting in a $23'.1 \times 23'.1$ field of view.

C.1.15. George Mason University

The George Mason University 0.8 m telescope is near Fairfax, VA. The telescope is equipped with a 4096×4096 SBIG-16803 camera having an image scale of $0''.35 \text{ pixel}^{-1}$, resulting in a $23' \times 23'$ field of view.

C.1.16. Hazelwood Observatory

The Hazelwood Observatory is located near Churchill, Victoria, Australia. The 0.32 m telescope is equipped with a SBIG STT-3200 camera with an image scale of $0''.55 \text{ pixel}^{-1}$, resulting in a $20' \times 14'$ field of view.

C.1.17. LCOGT

The Las Cumbres Observatory Global Telescope (LCOGT; Brown et al. 2013) 2.0 m, 1.0 m and 0.4 m network nodes are

located at Cerro Tololo Inter-American Observatory in Chile (CTIO), Siding Spring Observatory near Coonabarabran, Australia (SSO), South Africa Astronomical Observatory near Sutherland South Africa (SAAO), Teide Observatory on the island of Tenerife (TEID), McDonald Observatory near Fort Davis, TX, United States (McD), and Haleakala Observatory on Maui, Hawai'i (HA1). The MuSCAT3 multiband imager (Narita et al. 2020) is installed on the LCOGT 2 m Faulkes Telescope North at Haleakala Observatory. The image scale is $0''.27$ per pixel resulting in a $9'.1 \times 9'.1$ field of view. The 1 m telescopes are located at all nodes except Haleakala and are equipped with 4096×4096 SINISTRO cameras having an image scale of $0''.389$ per pixel, resulting in a $26' \times 26'$ field of view. The 0.4 m telescopes are located at all nodes and are equipped with 2048×3072 pixel SBIG STX6303 cameras having an image scale of $0''.57 \text{ pixel}^{-1}$, resulting in a $19' \times 29'$ field of view. All LCOGT images were calibrated by the standard LCOGT BANZAI pipeline (McCully et al. 2018), and differential photometric data were extracted using Astro-ImageJ (Collins et al. 2017).

C.1.18. Lewin Observatory

The Maury Lewin Astronomical Observatory is located in Glendora, CA. The 0.35 m telescope is equipped with a SBIG STF8300M detector that has an image scale of $0''.84 \text{ pixel}^{-1}$, resulting in a $23' \times 17'$ field of view.

C.1.19. Lookout Observatory

The Lookout Observatory is located in Colorado Springs, CO. The 0.5 m telescope is equipped with a ZWO ASI 1600MM Pro CMOS detector that has an image scale of $1''.46 \text{ pixel}^{-1}$, resulting in a $152' \times 101'$ field of view. The image data were calibrated and photometric data were extracted using the reduction and photometry pipeline described in Thomas & Paczkowski (2021).

C.1.20. MASTER-Ural

The Kourovka observatory of Ural Federal University houses a 0.4 m binocular MASTER-Ural telescope near Yekaterinburg, Russia. Each optical tube is equipped with an Apogee ALTA U16M detector with an image scale of $1''.85 \text{ pixel}^{-1}$, resulting in a $120' \times 120'$ field of view. The image data were calibrated and photometric data were extracted using the reduction and photometry pipeline described in Burdanov et al. (2014).

C.1.21. MEarth-S

MEarth-South (Irwin et al. 2007) consists of eight 0.4 m telescopes and observes from Cerro Tololo Inter-American Observatory, east of La Serena, Chile. Each telescope uses an Apogee U230 detector with a $29' \times 29'$ field of view and an image scale of $0''.84$ per pixel. Results were extracted using the custom pipelines described in Irwin et al. (2007).

C.1.22. Mt. Kent CDK700

The University of Louisville's MKO CDK700 telescope is located near Toowoomba, Queensland, Australia at the University of Southern Queensland's Mt. Kent Observatory. It is a remotely operated Planewave Instruments 0.7 m corrected Dall-Kirkham telescope with an Apogee U16M

camera incorporating an OnSemi KAF-16803 CCD with 4096×4096 $9 \mu\text{m}$ $0''.41$ pixels and a $28' \times 28'$ field of view.

C.1.23. Mt. Lemmon ULMT

The University of Louisville Manner telescope (ULMT) is located near Tucson, AZ, USA at Mt. Lemmon Observatory. It is a remotely operated RC Optical Systems 0.61 m Ritchie–Chrétien telescope with a focal plane scale of $43''$ mm with SBIG STX 16803 and Apogee U16M cameras incorporating OnSemi KAF-16803 CCDs with 4096×4096 $9 \mu\text{m}$ $0''.39$ pixels for a $27' \times 27'$ field of view.

C.1.24. Mt. Stuart Observatory

The Mt. Stuart Observatory is near Dunedin, New Zealand. The 0.32 m telescope is equipped with a 3072×2048 SBIG STXL-6303E camera with an image scale of $0''.88$ pixel⁻¹, resulting in a $44' \times 30'$ field of view.

C.1.25. MuSCAT

The Multicolor Simultaneous Camera for studying Atmospheres of Transiting exoplanets (MuSCAT; Narita et al. 2015) multicolor imager is installed at the 1.88 m telescope of the National Astronomical Observatory of Japan (NAOJ) in Okayama, Japan. MuSCAT is equipped with three detectors for the Sloan g' , Sloan i' , and Sloan z'_s bands. The image scale is $0''.358$ per pixel, resulting in a $6'.1 \times 6'.1$ field of view. MuSCAT data were extracted using the custom pipeline described in Fukui et al. (2011).

C.1.26. MuSCAT2

The MuSCAT2 multicolor imager (Narita et al. 2019) is installed at the 1.52 m Telescopio Carlos Sanchez (TCS) in the Teide Observatory, Spain. MuSCAT2 observes simultaneously in the Sloan g' , Sloan r' , Sloan i' , and z -short bands. The image scale is $0''.44$ per pixel, resulting in a $7'.4 \times 7'.4$ field of view. The photometry was carried out using standard aperture photometry calibration and reduction steps with a dedicated MuSCAT2 photometry pipeline, as described in Parviainen et al. (2019).

C.1.27. Observatori Astronòmic de la Universitat de València

The Observatori Astronòmic de la Universitat de València (OAUV) is located near Valencia, Spain. The 0.3 m telescope TURIA2 is equipped with a QHY600 detector that has an image scale of $0''.68$ pixel⁻¹, resulting in a $109' \times 73'$ field of view.

C.1.28. OAA

The Observatori Astronòmic Albanyà (OAA) is located in Albanyà, Girona, Spain. The 0.4 m telescope is equipped with a Moravian G4-9000 camera that has an image scale of $1''.44$ per 2×2 binned pixel, resulting in a $36' \times 36'$ field of view.

C.1.29. CALOU

Observatory de Ca l'Ou (CALOU) is a private observatory in Sant Martí Sesgueioles, near Barcelona, Spain. The 0.4 m telescope is equipped with a 1024×1024 pixel FLI PL1001 camera having an image scale of $1''.14$ pixel⁻¹, resulting in a $21' \times 21'$ field of view.

C.1.30. PEST

The Perth Exoplanet Survey Telescope (PEST) is located near Perth, Western Australia, Australia. The 0.3 m telescope is equipped with a 5544×3694 QHY183M camera. Images are binned 2×2 in software giving an image scale of $0''.7$ pixel⁻¹, resulting in a $32' \times 21'$ field of view. Prior to 2021 March 23, PEST was equipped with a 1530×1020 SBIG ST-8XME camera with an image scale of $1''.2$ pixel⁻¹, resulting in a $31' \times 21'$ field of view. A custom pipeline based on C-Munipack was used to calibrate the images and extract the differential photometry.¹²⁹

C.1.31. Privat Observatory Herges-Hallenberg

The Privat Observatory Herges-Hallenberg is a 0.28 m telescope near Steinbach-Hallenberg, Germany. It is equipped with a Moravian Instrument G2-1600 detector that has an image scale of $1''.02$ pixel⁻¹, resulting in a $27' \times 41'$ field of view.

C.1.32. PvDKO

The Peter van de Kamp Observatory is located atop the Science Center at Swarthmore College in Swarthmore, PA. The 0.62 m telescope has a QHY600 CMOS camera, which yields a $26' \times 17'$ field of view.

C.1.33. RCO

The 0.4 m RCO telescope is located at the Grand-Pra Observatory in Valais Sion, Switzerland. The telescope is equipped with a FLI 4710 detector with an image scale of $0''.73$ pixel⁻¹, resulting in a $12'.9 \times 12'.9$ field of view.

C.1.34. SAINT-EX

The SAINT-EX Observatory is located in San Pedro Mártir, Mexico. The 1.0 m telescope is equipped with an Andor detector that has an image scale of $0''.34$ per pixel, resulting in a $12' \times 12'$ field of view. The image data were calibrated and photometric data were extracted using the SAINT-EX automatic reduction and photometry pipeline (PRINCE; Demory et al. 2020).

C.1.35. Salerno University Observatory

The Salerno University Observatory houses a 0.6 m telescope and is located in Fisciano, Italy. The telescope is equipped with a FingerLakes Instrument Proline L230 that has a $21' \times 21'$ field of view with $0''.61$ pixel⁻¹.

C.1.36. SPECULOOS-S

The SPECULOOS Southern Observatory consists of four 1 m telescopes at the Paranal Observatory near Cerro Paranal, Chile (Jehin et al. 2018). The telescopes are equipped with detectors that have an image scale of $0''.35$ per pixel, resulting in a $12' \times 12'$ field of view. The image data were calibrated and photometric data were extracted using a dedicated pipeline described in Sebastian et al. (2020).

¹²⁹ <http://c-munipack.sourceforge.net>

C.1.37. Solaris SLR2

The SLR2 is one of four automated telescopes of the Solaris network, owned and operated by the N. Copernicus Astronomical Center of the Polish Academy of Sciences. SLR2 is a 0.5 m telescope located in SAAO, equipped an Andor iKon-L camera having an image scale of $0''.367 \text{ pixel}^{-1}$, resulting in a $12' \times 12'$ field of view.

C.1.38. SUTO-Otivar

The Silesian University of Technology Observatory (SUTO-Otivar) is an observatory near Motril, Spain. The 0.3 m telescope is equipped with a ZWO ASI 1600MM detector that has an image scale of $0''.685 \text{ pixel}^{-1}$, resulting in a $18' \times 13'$ field of view.

C.1.39. TRAPPIST

The TRANSiting Planets and Planetesimals Small Telescope (TRAPPIST) North 0.6 m telescope (Barkaoui et al. 2019) is located at Oukaimeden Observatory in Morocco and the TRAPPIST-South 0.6 m telescope (Gillon et al. 2011) is located at the ESO La Silla Observatory in Chile (Jehin et al. 2011). TRAPPIST-North is equipped with an Andor iKon-L BEX2 DD camera that has an image scale of $0''.6$ per pixel, resulting in a $20' \times 20'$ field of view. TRAPPIST-South is equipped with a FLI camera that has an image scale of $0''.64$ per pixel, resulting in a $22' \times 22'$ field of view. The image data were calibrated and photometric data were extracted using either *AstroImageJ* or a dedicated pipeline that uses the *prose* framework described in Garcia et al. (2022).

C.1.40. Union College Observatory

The Union College observatory houses a 0.51 m telescope and is located in Schenectady, NY. The SBIG STXL detector has an image scale of $0''.93$ per 2×2 binned pixel, resulting in a $30' \times 20'$ field of view.

C.1.41. Villa '39

The Villa '39 Observatory is located in Landers, CA. The 0.35 m telescope is equipped with a KAF-16803 detector that has an image scale of $0''.94 \text{ pixel}^{-1}$, resulting in a $32'.5 \times 32'.5$ field of view.

C.1.42. WCO

The Waffelow Creek Observatory (WCO) is located in Nacogdoches, TX. The 0.35 m telescope is equipped with a SBIG STXL-6303E detector that has an image scale of $0''.66 \text{ pixel}^{-1}$, resulting in a $34' \times 23'$ field of view.

C.1.43. Wellesley College Whitin Observatory

The Whitin observatory is a 0.7 m telescope in Wellesley, MA. The 2048×2048 FLI ProLine PL23042 detector has an image scale of $0''.68 \text{ pixel}^{-1}$, resulting in a $23'.2 \times 23'.2$ field of view.

C.1.44. Ground Survey and Space Data

We used archival ground-based survey data and related follow-up observations from HATSouth (Bakos et al. 2013) and WASP (Pollacco et al. 2006) that predated the TESS

mission to help disposition some of the planet candidates. We also used results from the Gaia-TESS collaboration (Panahi et al. 2022), which is a joint analysis of TESS photometry and unpublished Gaia time-series photometry, to disposition some planet candidates. Additionally, we used archival data taken by ZTF for a subset of the best-in-class TOIs to determine if their signals were on-target. To accomplish this, we implemented the code DEATHSTAR (Ross et al. 2024), which is further described in Section 5.3.

*C.2. Reconnaissance Spectroscopy**C.2.1. CHIRON*

We obtained high-resolution spectroscopic vetting observations with the CHIRON spectrograph for a number of the TESS planet candidates. CHIRON is a high-resolution echelle spectrograph on the SMARTS 1.5 m telescope at the Cerro Tololo Inter-American Observatory, Chile (Tokovinin et al. 2013). We typically make use of the spectrograph in its “slicer” mode, fed via a fiber through an image slicer to achieve a spectral resolving power of $R \sim 80,000$ over the wavelength range of 4100–8700 Å. Spectral extraction is performed via the official CHIRON pipeline (Paredes et al. 2021). We derive RVs and spectral line profiles via a least-squares deconvolution (Donati et al. 1997) between the observed spectra and a nonrotating synthetic spectral template that matches the atmospheric parameters of the target star. Radial and line-broadening velocities are derived by modeling the line profile as per Zhou et al. (2020). For some of the faintest host stars ($V \gtrsim 12.5$), we use CHIRON in “fiber” mode, which achieves a lower resolving power of $R \sim 28,000$, but yields similar vetting information at lower precision.

C.2.2. CORALIE

The CORALIE high-resolution echelle spectrograph is mounted on the Swiss Euler 1.2 m telescope at La Silla Observatory, Chile (Queloz et al. 2001). The spectrograph is fed by a $2''$ on-sky science fiber and a secondary B-fiber that can be used for simultaneous wavelength calibrations with a Fabry–Pérot etalon or pointed on-sky to monitor background contamination. CORALIE has a spectral resolution of $R \sim 60,000$ and reaches an RV precision of 3 m s^{-1} when photon limited. Stellar RV measurements are extracted via cross-correlation with a mask (Baranne et al. 1996; Pepe et al. 2002b), using the standard CORALIE data-reduction pipeline. TOIs are vetted using several cross-correlation function line diagnostics such as bisector span and FWHM. We also check for mask-dependent RVs, SB2, SB1, and visual binaries. False positives are routinely reported to EXOFOP-TESS and data made available through the DACE platform.¹³⁰

C.2.3. FEROS

The Fiber-fed Extended Range Optical Spectrograph (FEROS; Kaufer & Pasquini 1998) spectrograph is a high-resolution ($R \sim 48,000$) echelle spectrograph installed at the MPG2.2 m telescope at the ESO La Silla Observatory, Chile. FEROS covers the spectral range between 350 and 920 nm and has a comparison fiber to trace instrumental RV drifts during the science exposures with a thorium argon (ThAr) lamp. FEROS

¹³⁰ <https://dace.unige.ch/radialVelocities/?pattern=TOI-128>

data are processed with the automated *ceres* pipeline (Brahm et al. 2017) that generates precision RVs and bisector span measurements starting from the raw images, which are reduced, optimally extracted, and wavelength calibrated before cross-correlating the spectrum with a G2-type binary mask.

C.2.4. FIES

We used the Fibre-fed Echelle Spectrograph (FIES; Telting et al. 2014), a cross-dispersed high-resolution spectrograph mounted on the 2.56 m Nordic Optical Telescope (NOT; Djupvik & Andersen 2010), at the Observatorio del Roque de los Muchachos in La Palma, Spain. FIES has a maximum resolving power of $R \sim 67,000$, and a spectral coverage that ranges from 3760 to 8820 Å. The data were extracted as described in Buchhave et al. (2010).

C.2.5. HARPS-N

HARPS-N is a fiber-fed, cross-dispersed echelle spectrograph with a spectral resolution of 115,000 mounted at the 3.58 m Telescopio Nazionale Galileo (TNG) in La Palma island, Spain. It covers the visible wavelength range from 3830 to 6900 Å (Cosentino et al. 2012). Spectra extraction and reduction were carried out using the HARPS-N data-reduction software. RVs were obtained by cross-correlating the spectra with a numerical mask close to the stellar spectral type (e.g., Pepe et al. 2002a).

C.2.6. Keck/HIRES

We obtained RV data using the Keck Observatory HIRES spectrometer (Vogt et al. 1994) on the Keck I telescope atop Maunakea. These spectra were taken as part of the TESS-Keck Survey as described in MacDougall et al. (2023). All of them are iodine-free reconnaissance spectra with $S/N \approx 40 \text{ pixel}^{-1}$ across 3600–9000 Å and checked for rapid stellar rotation and spectroscopic false positives. Additionally, stellar effective temperature, metallicity, and surface gravity were extracted from these spectra by comparing each to spectra from both *SpecMatch-Syn* (Petigura 2015) and *SpecMatch-Emp* (Yee et al. 2017).

C.2.7. MINERVA-Australis

We carried out spectroscopic observations using the MINERVA-Australis facility (Addison et al. 2019). MINERVA-Australis consists of an array of four independently operated 0.7 m CDK700 telescopes situated at the Mount Kent Observatory in Queensland, Australia. Each telescope simultaneously feeds stellar light via fiber-optic cables to a single KiwiSpec R4-100 high-resolution ($R = 80,000$) spectrograph (Barnes et al. 2012) with wavelength coverage from 480 to 620 nm. RVs for the observations are derived for each telescope by cross-correlation, where the template being matched is the mean spectrum of each telescope. The instrumental variations are corrected by using simultaneous ThAr arc-lamp observations.

C.2.8. NRES

The NRES (Sivervd et al. 2018) is a set of four identical fiber-fed spectrographs on the 1 m telescopes of LCOGT (Brown et al. 2013). The NRES units are located at the LCOGT nodes at Cerro Tololo Inter-American Observatory, Chile; McDonald

Observatory, Texas, USA; South African Astronomical Observatory, South Africa; and Wise Observatory, Israel. The spectrographs deliver a resolving power of $R \sim 53,000$ over the wavelength range 3800–8600 Å. The data were reduced and RVs measured using the *BANZAI-NRES* pipeline (McCully et al. 2022). We measured stellar parameters from the spectra using a custom implementation of the *SpecMatch-Synth* package.¹³¹

C.2.9. PFS

The Planet Finder Spectrograph (PFS; Crane et al. 2006, 2008, 2010) is installed at the 6.5 m Magellan/Clay telescope at Las Campanas Observatory. Targets were observed with the iodine gas absorption cell of the instrument, adopting an exposure time of 1200 s and using a 3×3 CCD binning mode to minimize read noise. Targets were also observed without the iodine cell in order to generate the template for computing the RVs, which were derived following the methodology of Butler et al. (1996).

C.2.10. TRES

Reconnaissance spectra were obtained with the Tillinghast Reflector Echelle Spectrograph (TRES; Fűrész 2008), which is mounted on the 1.5 m Tillinghast Reflector telescope at the Fred Lawrence Whipple Observatory (FLWO) located on Mount Hopkins in Arizona. TRES is a fiber-fed echelle spectrograph with a wavelength range of 390–910 nm and a resolving power of $R \sim 44,000$. Typically, 2–3 spectra of each target are obtained at opposite orbital quadratures to check for large velocity variation due to a stellar companion. The spectra are also visually inspected to ensure a single-lined spectrum. The TRES spectra are extracted as described in Buchhave et al. (2010) and stellar parameters are derived using the Stellar Parameter Classification (SP) tool (Buchhave et al. 2012). SPC cross-correlates an observed spectrum against a grid of synthetic spectra based on Kurucz atmospheric models (Kurucz 1992) to derive the effective temperature, surface gravity, metallicity, and rotational velocity of the star.

ORCID iDs

Benjamin J. Hord  <https://orcid.org/0000-0001-5084-4269>

Eliza M.-R. Kempton  <https://orcid.org/0000-0002-1337-9051>

Evans-Soma Thomas M.  <https://orcid.org/0000-0001-5442-1300>

David W. Latham  <https://orcid.org/0000-0001-9911-7388>

David R. Ciardi  <https://orcid.org/0000-0002-5741-3047>

Diana Dragomir  <https://orcid.org/0000-0003-2313-467X>

Knicole D. Colón  <https://orcid.org/0000-0001-8020-7121>


Andrew Vanderburg  <https://orcid.org/0000-0001-7246-5438>


Zoe L. de Beurs  <https://orcid.org/0000-0002-7564-6047>


Karen A. Collins  <https://orcid.org/0000-0001-6588-9574>

Cristilyn N. Watkins  <https://orcid.org/0000-0001-8621-6731>

Jacob Bean  <https://orcid.org/0000-0003-4733-6532>

Nicolas B. Cowan  <https://orcid.org/0000-0001-6129-5699>

Tansu Daylan  <https://orcid.org/0000-0002-6939-9211>

Caroline V. Morley  <https://orcid.org/0000-0002-4404-0456>

¹³¹ <https://github.com/petigura/specmatch-syn>

- Jeguh Ih <https://orcid.org/0000-0003-2775-653X>
 David Baker <https://orcid.org/0000-0002-2970-0532>
 Khalid Barkaoui <https://orcid.org/0000-0003-1464-9276>
 Natalie M. Batalha <https://orcid.org/0000-0002-7030-9519>
 Aida Behrard <https://orcid.org/0000-0003-0012-9093>
 Alexander Belinski <https://orcid.org/0000-0003-3469-0989>
 Zouhair Benkhaldoun <https://orcid.org/0000-0001-6285-9847>
 Paul Benni <https://orcid.org/0000-0001-6981-8722>
 Krzysztof Bernacki <https://orcid.org/0000-0003-4647-7114>
 Allyson Bieryla <https://orcid.org/0000-0001-6637-5401>
 Avraham Binnenfeld <https://orcid.org/0000-0002-9319-3838>
 Pau Bosch-Cabot <https://orcid.org/0000-0002-1514-5558>
 François Bouchy <https://orcid.org/0000-0002-7613-393X>
 Valerio Bozza <https://orcid.org/0000-0003-4590-0136>
 Rafael Brahm <https://orcid.org/0000-0002-9158-7315>
 Lars A. Buchhave <https://orcid.org/0000-0003-1605-5666>
 Ashley Chontos <https://orcid.org/0000-0003-1125-2564>
 Catherine A. Clark <https://orcid.org/0000-0002-2361-5812>
 Ryan Cloutier <https://orcid.org/0000-0001-5383-9393>
 Kevin I. Collins <https://orcid.org/0000-0003-2781-3207>
 Dennis M. Conti <https://orcid.org/0000-0003-2239-0567>
 Ian J. M. Crossfield <https://orcid.org/0000-0002-1835-1891>
 Fei Dai <https://orcid.org/0000-0002-8958-0683>
 Jerome P. de Leon <https://orcid.org/0000-0002-6424-3410>
 Georgina Dransfield <https://orcid.org/0000-0002-3937-630X>
 Courtney Dressing <https://orcid.org/0000-0001-8189-0233>
 Adam Dustor <https://orcid.org/0000-0001-5516-9733>
 Gilbert Esquerdo <https://orcid.org/0000-0002-9789-5474>
 Phil Evans <https://orcid.org/0000-0002-5674-2404>
 Sergio B. Fajardo-Acosta <https://orcid.org/0000-0001-9309-0102>
 Jerzy Fiołka <https://orcid.org/0000-0003-0551-6746>
 Raquel Forés-Toribio <https://orcid.org/0000-0002-6482-2180>
 Antonio Frasca <https://orcid.org/0000-0002-0474-0896>
 Akihiko Fukui <https://orcid.org/0000-0002-4909-5763>
 Benjamin Fulton <https://orcid.org/0000-0003-3504-5316>
 Elise Furlan <https://orcid.org/0000-0001-9800-6248>
 Tianjun Gan <https://orcid.org/0000-0002-4503-9705>
 Davide Gandolfi <https://orcid.org/0000-0001-8627-9628>
 Steven Giacalone <https://orcid.org/0000-0002-8965-3969>
 Emily A. Gilbert <https://orcid.org/0000-0002-0388-8004>
 Michaël Gillon <https://orcid.org/0000-0003-1462-7739>
 Eric Girardin <https://orcid.org/0000-0002-5443-3640>
 Erica Gonzales <https://orcid.org/0000-0002-9329-2190>
 Ferran Grau Horta <https://orcid.org/0000-0001-9927-7269>
 Joao Gregorio <https://orcid.org/0000-0002-0145-5248>
 Michael Greklek-McKeon <https://orcid.org/0000-0002-0371-1647>
 Pere Guerra <https://orcid.org/0000-0002-4308-2339>
 J. D. Hartman <https://orcid.org/0000-0001-8732-6166>
 Ian Helm <https://orcid.org/0000-0002-0473-4437>
 Krzysztof G. Helminiak <https://orcid.org/0000-0002-7650-3603>
 Thomas Henning <https://orcid.org/0000-0002-1493-300X>
 Michelle L. Hill <https://orcid.org/0000-0002-0139-4756>
 Keith Horne <https://orcid.org/0000-0003-1728-0304>
 Andrew W. Howard <https://orcid.org/0000-0001-8638-0320>
 Steve B. Howell <https://orcid.org/0000-0002-2532-2853>
 Daniel Huber <https://orcid.org/0000-0001-8832-4488>
 Emmanuel Jehin <https://orcid.org/0000-0001-8923-488X>
 Jon M. Jenkins <https://orcid.org/0000-0002-4715-9460>
 Eric L. N. Jensen <https://orcid.org/0000-0002-4625-7333>
 Marshall C. Johnson <https://orcid.org/0000-0002-5099-8185>
 Andrés Jordán <https://orcid.org/0000-0002-5389-3944>
 Stephen R. Kane <https://orcid.org/0000-0002-7084-0529>
 John F. Kielkopf <https://orcid.org/0000-0003-0497-2651>
 Vadim Krushinsky <https://orcid.org/0000-0001-9388-691X>
 Sławomir Lasota <https://orcid.org/0000-0001-8179-7653>
 Elena Lee <https://orcid.org/0000-0001-9312-8596>
 Pablo Lewin <https://orcid.org/0000-0003-0828-6368>
 John H. Livingston <https://orcid.org/0000-0002-4881-3620>
 Jack Lubin <https://orcid.org/0000-0001-8342-7736>
 Michael B. Lund <https://orcid.org/0000-0003-2527-1598>
 Christopher R. Mann <https://orcid.org/0000-0002-9312-0073>
 Giuseppi Marino <https://orcid.org/0000-0001-8134-0389>
 Nataliia Maslennikova <https://orcid.org/0000-0003-4147-5195>
 Bob Massey <https://orcid.org/0000-0001-8879-7138>
 Rachel Matson <https://orcid.org/0000-0001-7233-7508>
 Elisabeth Matthews <https://orcid.org/0000-0003-0593-1560>
 Andrew W. Mayo <https://orcid.org/0000-0002-7216-2135>
 Kim K. McLeod <https://orcid.org/0000-0001-9504-1486>
 Teo Močnik <https://orcid.org/0000-0003-4603-556X>
 Mayuko Mori <https://orcid.org/0000-0003-1368-6593>
 Jose A. Muñoz <https://orcid.org/0000-0001-9833-2959>
 Norio Narita <https://orcid.org/0000-0001-8511-2981>
 Louise Dyregaard Nielsen <https://orcid.org/0000-0002-5254-2499>
 Hugh Osborn <https://orcid.org/0000-0002-4047-4724>
 Aviad Panahi <https://orcid.org/0000-0001-5850-4373>
 Peter Plavchan <https://orcid.org/0000-0002-8864-1667>
 Alex S. Polanski <https://orcid.org/0000-0001-7047-8681>
 Adam Popowicz <https://orcid.org/0000-0003-3184-5228>
 Francisco J. Pozuelos <https://orcid.org/0000-0003-1572-7707>
 Samuel N. Quinn <https://orcid.org/0000-0002-8964-8377>
 Don J. Radford <https://orcid.org/0000-0002-3940-2360>
 Phillip A. Reed <https://orcid.org/0000-0002-5005-1215>
 Howard M. Relles <https://orcid.org/0009-0009-5132-9520>
 Malena Rice <https://orcid.org/0000-0002-7670-670X>
 Paul Robertson <https://orcid.org/0000-0003-0149-9678>
 Joseph E. Rodriguez <https://orcid.org/0000-0001-8812-0565>
 Lee J. Rosenthal <https://orcid.org/0000-0001-8391-5182>
 Ryan A. Rubenzahl <https://orcid.org/0000-0003-3856-3143>
 Nicole Schanche <https://orcid.org/0000-0002-9526-3780>
 Joshua Schlieder <https://orcid.org/0000-0001-5347-7062>
 Richard P. Schwarz <https://orcid.org/0000-0001-8227-1020>
 Ramotholo Sefako <https://orcid.org/0000-0003-3904-6754>
 Avi Shporer <https://orcid.org/0000-0002-1836-3120>
 Alessandro Sozzetti <https://orcid.org/0000-0002-7504-365X>
 Chris Stockdale <https://orcid.org/0000-0003-2163-1437>
 Alexander Tarasenkov <https://orcid.org/0009-0005-0534-9812>
 Thiam-Guan Tan <https://orcid.org/0000-0001-5603-6895>
 Eric B. Ting <https://orcid.org/0000-0002-8219-9505>

Judah Van Zandt  <https://orcid.org/0000-0002-4290-6826>
 Ian Waite  <https://orcid.org/0000-0002-3249-3538>
 Noriharu Watanabe  <https://orcid.org/0000-0002-7522-8195>
 Lauren M. Weiss  <https://orcid.org/0000-0002-3725-3058>
 Justin Wittrock  <https://orcid.org/0000-0002-7424-9891>
 George Zhou  <https://orcid.org/0000-0002-4891-3517>
 Carl Ziegler  <https://orcid.org/0000-0002-0619-7639>
 Shay Zucker  <https://orcid.org/0000-0003-3173-3138>

References

- Addison, B., Wright, D. J., Wittenmyer, R. A., et al. 2019, *PASP*, **131**, 115003
 Ahner, E.-M., Stevenson, K. B., Mansfield, M., et al. 2023, *Natur*, **614**, 653
 Almenara, J., Bonfils, X., Bryant, E., et al. 2024, *A&A*, **683**, A166
 Almenara, J. M., Bonfils, X., Forveille, T., et al. 2022, *A&A*, **667**, L11
 Astropy Collaboration, Price-Whelan, A. M., Lim, P. L., et al. 2022, *ApJ*, **935**, 167
 Astropy Collaboration, Price-Whelan, A. M., Sipőcz, B. M., et al. 2018, *AJ*, **156**, 123
 Astropy Collaboration, Robitaille, T. P., Tollerud, E. J., et al. 2013, *A&A*, **558**, A33
 August, P. C., Bean, J. L., Zhang, M., et al. 2023, *ApJL*, **953**, L24
 Auvergne, M., Bodin, P., Boisnard, L., et al. 2009, *A&A*, **506**, 411
 Bakos, G., Noyes, R., Kovács, G., et al. 2004, *PASP*, **116**, 266
 Baraffe, I., Chabrier, G., Allard, F., & Hauschildt, P. H. 1998, *A&A*, **337**, 403
 Baranne, A., Queloz, D., Mayor, M., et al. 1996, *A&AS*, **119**, 373
 Barkaoui, K., Burdanov, A., Hellier, C., et al. 2019, *AJ*, **157**, 43
 Barnes, S. I., Gibson, S., Nield, K., & Cochrane, D. 2012, *Proc. SPIE*, **8446**, 1053
 Barros, S. C. C., Demangeon, O. D. S., Armstrong, D. J., et al. 2023, *A&A*, **673**, A4
 Batalha, N. E., Lewis, T., Fortney, J. J., et al. 2019, *ApJL*, **885**, L25
 Beichman, C., Benneke, B., Knutson, H., et al. 2014, *PASP*, **126**, 1134
 Bell, T. J., Kreidberg, L., Kendrew, S., et al. 2023, arXiv:2301.06350
 Bellm, E. C., Kulkarni, S. R., Graham, M. J., et al. 2019, *PASP*, **131**, 018002
 Berdnikov, L. N., Belinskii, A. A., Shatskii, N. I., et al. 2020, *ARep*, **64**, 310
 Bieryla, A., Zhou, G., García-Mejía, J., et al. 2024, *MNRAS*, **527**, 10955
 Bonfils, X., Almenara, J. M., Jocu, L., et al. 2015, *Proc. SPIE*, **9605**, 96051L
 Borucki, W. J., Koch, D., Basri, G., et al. 2010, *Sci*, **327**, 977
 Brady, M. T., & Bean, J. L. 2022, *AJ*, **163**, 255
 Brahm, R., Jordán, A., & Espinoza, N. 2017, *PASP*, **129**, 034002
 Brasseur, C. E., Phillip, C., Fleming, S. W., Mullally, S. E., & White, R. L., 2019 *Astrocute: Tools for Creating Cutouts of TESS Images*, Astrophysics Source Code Library, ascl:1905.007
 Brown, T. M., Baliber, N., Bianco, F. B., et al. 2013, *PASP*, **125**, 1031
 Buchhave, L. A., Bakos, G. Á., Hartman, J. D., et al. 2010, *ApJ*, **720**, 1118
 Buchhave, L. A., Latham, D., Johansen, A., et al. 2012, *Natur*, **486**, 375
 Burdanov, A. Y., Krushinsky, V. V., & Popov, A. A. 2014, *AstBu*, **69**, 368
 Butler, R. P., Marcy, G. W., Williams, E., et al. 1996, *PASP*, **108**, 500
 Cacciapuoti, L., Kostov, V. B., Kuchner, M., et al. 2022, *MNRAS*, **513**, 102
 Changeat, Q., Edwards, B., Al-Refaie, A. F., et al. 2022, *ApJS*, **260**, 3
 Charbonneau, D., Brown, T. M., Noyes, R. W., & Gilliland, R. L. 2002, *ApJ*, **568**, 377
 Chaturvedi, P., Bluhm, P., Nagel, E., et al. 2022, *A&A*, **666**, A155
 Chen, J., & Kipping, D. 2017, *ApJ*, **834**, 17
 Ciardi, D. R., Beichman, C. A., Horch, E. P., & Howell, S. B. 2015, *ApJ*, **805**, 16
 Collins, K. 2019, AAS Meeting Abstracts, **233**, 140.05
 Collins, K. A., Kielkopf, J. F., Stassun, K. G., & Hessman, F. V. 2017, *AJ*, **153**, 77
 Cosentino, R., Lovis, C., Pepe, F., et al. 2012, *Proc. SPIE*, **8446**, 84461V
 Coughlin, J. L., Thompson, S. E., Bryson, S. T., et al. 2014, *AJ*, **147**, 119
 Coulombe, L.-P., Benneke, B., Challener, R., et al. 2023, *Natur*, **620**, 292
 Crane, J. D., Shtetman, S. A., Butler, R. P., Thompson, I. B., & Burley, G. S. 2008, *Proc. SPIE*, **7014**, 2484
 Crane, J. D., Shtetman, S. A., & Butler, R. P. 2006, *Proc. SPIE*, **6269**, 972
 Crane, J. D., Shtetman, S. A., Butler, R. P., et al. 2010, *Proc. SPIE*, **7735**, 1909
 Bakos, G. Á., Csabry, Z., Penev, K., et al. 2013, *PASP*, **125**, 154
 de Leon, J. P., Livingston, J. H., Jenkins, J. S., et al. 2023, *MNRAS*, **522**, 750
 Deming, D., Seager, S., Winn, J., et al. 2009, *PASP*, **121**, 952
 Demory, B. O., Pozuelos, F. J., Gómez Maqueo Chew, Y., et al. 2020, *A&A*, **642**, A49
 Desidera, S., Damasso, M., Gratton, R., et al. 2023, *A&A*, **675**, A158
 Djupvik, A. A., & Andersen, J. 2010, *ASSP*, **14**, 211
 Donati, J. F., Semel, M., Carter, B. D., Rees, D. E., & Collier Cameron, A. 1997, *MNRAS*, **291**, 658
 Edwards, B., & Tinetti, G. 2022, *AJ*, **164**, 15
 Fűrész, G. 2008, PhD thesis, University of Szeged, Hungary
 Fortney, J. J., Mordasini, C., Nettelmann, N., et al. 2013, *ApJ*, **775**, 80
 Fukui, A., Narita, N., Tristram, P. J., et al. 2011, *PASJ*, **63**, 287
 Furlan, E., Ciardi, D. R., Everett, M. E., et al. 2017, *AJ*, **153**, 71
 Gao, P., Thorngren, D. P., Lee, E. K., et al. 2020, *NatAs*, **4**, 951
 Garcia, L. J., Timmermans, M., Pozuelos, F. J., et al. 2022, *MNRAS*, **509**, 4817
 Gardner, J. P., Mather, J. C., Abbott, R., et al. 2023, *PASP*, **135**, 24
 Gardner, J. P., Mather, J. C., Clampin, M., et al. 2006, *SSRv*, **123**, 485
 Giacalone, S., & Dressing, C. D., 2020 *triceratops: Candidate Exoplanet Rating Tool*, Astrophysics Source Code Library, ascl:2002.004
 Giacalone, S., Dressing, C. D., Jensen, E. L. N., et al. 2021, *AJ*, **161**, 24
 Gilbert, E. A., Barclay, T., Schlieder, J. E., et al. 2020, *AJ*, **160**, 116
 Gillon, M., Jehin, E., Magain, P., et al. 2011, *EPJ Web Conf.*, **11**, 06002
 Ginsburg, A., Sipőcz, B. M., Brasseur, C. E., et al. 2019, *AJ*, **157**, 98
 Girardi, L., Barbieri, M., Groenewegen, M. A., et al. 2012, *Red Giants as Probes of the Structure and Evolution of the Milky Way* (Berlin: Springer), 165
 Girardi, L., Groenewegen, M., Hatziminaoglou, E., & Da Costa, L. 2005, *A&A*, **436**, 895
 Greene, T. P., Bell, T. J., Ducrot, E., et al. 2023, *Natur*, **618**, 39
 Greene, T. P., Line, M. R., Montero, C., et al. 2016, *ApJ*, **817**, 17
 Guerrero, N. M., Seager, S., Huang, C. X., et al. 2021, *ApJS*, **254**, 39
 Hawthorn, F., Bayliss, D., Wilson, T. G., et al. 2023, *MNRAS*, **520**, 3649
 Hobson, M. J., Jordán, A., Bryant, E. M., et al. 2023, *ApJL*, **946**, L4
 Hord, B. J., Colón, K. D., Kostov, V., et al. 2021, *AJ*, **162**, 263
 Howell, S. B., Everett, M. E., Sherry, W., Horch, E., & Ciardi, D. R. 2011, *AJ*, **142**, 19
 Howell, S. B., Scott, N. J., Matson, R. A., et al. 2021, *FrASS*, **8**, 635864
 Howell, S. B., Sobek, C., Haas, M., et al. 2014, *PASP*, **126**, 398
 Huang, C. X., Vanderburg, A., Pál, A., et al. 2020, *RNAAS*, **4**, 204
 Huber, D., White, T. R., Metcalfe, T. S., et al. 2022, *AJ*, **163**, 79
 Hunter, J. D. 2007, *CSE*, **9**, 90
 Irwin, J., Irwin, M., Aigrain, S., et al. 2007, *MNRAS*, **375**, 1449
 Jehin, E., Gillon, M., Queloz, D., et al. 2011, *Msngr*, **145**, 2
 Jehin, E., Gillon, M., Queloz, D., et al. 2018, *Msngr*, **174**, 2
 Jenkins, J. M., Twicken, J. D., McCauliff, S., et al. 2016, *Proc. SPIE*, **9913**, 99133E
 Jensen, E., 2013 *Tapir: A Web Interface for Transit/eclipse Observability*, Astrophysics Source Code Library, ascl:1306.007
 Kaufer, A., & Pasquini, L. 1998, *Proc. SPIE*, **3355**, 844
 Kempton, E. M. R., Bean, J. L., Louie, D. R., et al. 2018, *PASP*, **130**, 114401
 Kempton, E. M. R., Zhang, M., Bean, J. L., et al. 2023, *Natur*, **620**, 67
 Kendrew, S., Scheithauer, S., Bouchet, P., et al. 2015, *PASP*, **127**, 623
 Kendrew, S., Scheithauer, S., Bouchet, P., et al. 2016, *Proc. SPIE*, **9904**, 990443
 Kluyver, T., Ragan-Kelley, B., Pérez, F., et al. 2016, in *Positioning and Power in Academic Publishing: Players, Agents and Agendas*, ed. F. Loizides & B. Schmidt (Amsterdam: IOS Press), 87
 Kostov, V. B., Mullally, S. E., Quintana, E. V., et al. 2019, *AJ*, **157**, 124
 Kunimoto, M., Winn, J., Ricker, G. R., & Vanderspek, R. K. 2022, *AJ*, **163**, 290
 Kurucz, R. L. 1992, in *IAU Symp. 149, The Stellar Populations of Galaxies*, ed. B. Barbuy & A. Renzini (Dordrecht: Kluwer), 225
 Li, J., Tenenbaum, P., Twicken, J. D., et al. 2019, *PASP*, **131**, 024506
 Lightcurve Collaboration, Cardoso, J. V. d. M., Hedges, C., et al., 2018 *Lightkurve: Kepler and TESS Time Series Analysis in Python*, Astrophysics Source Code Library, ascl:1812.013
 Lillo-Box, J., Gandolfi, D., Armstrong, D. J., et al. 2023, *A&A*, **669**, A109
 Lissauer, J. J., Marcy, G. W., Rowe, J. F., et al. 2012, *ApJ*, **750**, 112
 Louie, D. R., Deming, D., Albert, L., et al. 2018, *PASP*, **130**, 044401
 MacDougall, M. G., Petigura, E. A., Gilbert, G. J., et al. 2023, *AJ*, **166**, 33
 Madhusudhan, N. 2019, *ARA&A*, **57**, 617
 Mansfield, M., Line, M. R., Bean, J. L., et al. 2021, *NatAs*, **5**, 1224
 Mascareño, A. S., Passegger, V., Hernández, J., et al. 2024, arXiv:2402.04113
 Mayor, M., & Queloz, D. 1995, *Natur*, **378**, 355
 McCully, C., Daily, M., Brandt, G. M., et al. 2022, *Proc. SPIE*, **12189**, 1218914
 McCully, C., Volgenau, N. H., Harbeck, D.-R., et al. 2018, *Proc. SPIE*, **10707**, 107070K
 McKinney, W. 2010, in *Proc. 9th Python in Science Conf.*, ed. S. van der Walt & J. Millman (Austin, TX: SciPy), 51
 Miles, B. E., Biller, B. A., Patapis, P., et al. 2023, *ApJL*, **946**, L6

- Mistry, P., Prasad, A., Maity, M., et al. 2023, arXiv:2311.00688
- Mollière, P., Molyarova, T., Bitsch, B., et al. 2022, *ApJ*, 934, 74
- Morris, R. L., Twicken, J. D., Smith, J. C., et al. 2020, Kepler Data Processing Handbook: Photometric Analysis [KSCI-19081-003](#), Kepler Science Document
- Morton, T. D. 2012, *ApJ*, 761, 6
- Morton, T. D., 2015 VESPA: False Positive Probabilities Calculator, Astrophysics Source Code Library, ascl:1503.011
- Morton, T. D., Giacalone, S., & Bryson, S. 2023, *RNAAS*, 7, 107
- Moutou, C., Deleuil, M., Guillot, T., et al. 2013, *Icar*, 226, 1625
- Murgas, F., Nowak, G., Masseron, T., et al. 2022, *A&A*, 668, A158
- Murgas, F., Pallé, E., Orell-Miquel, J., et al. 2024, *A&A*, 684, A83
- Naponiello, L., Mancini, L., Sozzetti, A., et al. 2023, *Natur*, 623, E6
- Narita, N., Fukui, A., Kusakabe, N., et al. 2015, *JATIS*, 1, 045001
- Narita, N., Fukui, A., Kusakabe, N., et al. 2019, *JATIS*, 5, 015001
- Narita, N., Fukui, A., Yamamuro, T., et al. 2020, *Proc. SPIE*, 11447, 114475K
- NExSci 2022, Exoplanet Follow-up Observing Program Web Service, IPAC, doi:10.26134/EXOFOF5
- Osborn, A., Armstrong, D. J., Fernández Fernández, J., et al. 2023, *MNRAS*, 526, 548
- Palle, E., Orell-Miquel, J., Brady, M., et al. 2023, *A&A*, 678, 28
- Panahi, A., Mazeh, T., Zucker, S., et al. 2022, *A&A*, 667, A14
- Paredes, L. A., Henry, T. J., Quinn, S. N., et al. 2021, *AJ*, 162, 176
- Parviainen, H., Tingley, B., Deeg, H. J., et al. 2019, *A&A*, 630, A89
- Pepe, F., Mayor, M., Galland, F., et al. 2002a, *A&A*, 388, 632
- Pepe, F., Mayor, M., Rupprecht, G., et al. 2002b, *Msngr*, 110, 9
- Petigura, E. 2015, PhD thesis, University of California
- Pollacco, D. L., Skillen, I., Cameron, A. C., et al. 2006, *PASP*, 118, 1407
- Pontoppidan, K. M., Pickering, T. E., Laidler, V. G., et al. 2016, *Proc. SPIE*, 9910, 991016
- Psaridi, A., Bouchy, F., Lendl, M., et al. 2023, *A&A*, 675, A39
- Queloz, D., Mayor, M., Udry, S., et al. 2001, *Msngr*, 105, 1
- Quintana, E. V., Gilbert, E. A., Barclay, T., et al. 2023, *AJ*, 166, 15
- Rescigno, F., Hébrard, G., Vanderburg, A., et al. 2024, *MNRAS*, 527, 5385
- Ricker, G. R., Winn, J. N., Vanderspek, R., et al. 2015, *JATIS*, 1, 014003
- Rieke, G. H., Wright, G., Böker, T., et al. 2015, *PASP*, 127, 584
- Ross, G., Vanderburg, A., de Beurs, Z. L., et al. 2024, *MNRAS*, 528, 5160
- Rubenzahl, R. A., Dai, F., Howard, A. W., et al. 2024, *AJ*, 167, 16
- Scott, N. J., Howell, S. B., Gnilka, C. L., et al. 2021, *FrASS*, 8, 138
- Sebastian, D., Pedersen, P. P., Murray, C. A., et al. 2020, *Proc. SPIE*, 11445, 1144521
- Sing, D. K., Fortney, J. J., Nikolov, N., et al. 2016, *Natur*, 529, 59
- Siverd, R. J., Brown, T. M., Barnes, S., et al. 2018, *Proc. SPIE*, 10702, 107026C
- Skrutskie, M. F., Cutri, R. M., Stiening, R., et al. 2006, *AJ*, 131, 1163
- Smith, J. C., Stumpe, M. C., Van Cleve, J. E., et al. 2012, *PASP*, 124, 1000
- Stassun, K. G., Oelkers, R. J., Paegert, M., et al. 2019, *AJ*, 158, 138
- Stevenson, K. B. 2016, *ApJL*, 817, L16
- Stevenson, K. B., Lewis, N. K., Bean, J. L., et al. 2016, *PASP*, 128, 094401
- Stumpe, M. C., Smith, J. C., Catanzarite, J. H., et al. 2014, *PASP*, 126, 100
- Stumpe, M. C., Smith, J. C., Van Cleve, J. E., et al. 2012, *PASP*, 124, 985
- Telting, J. H., Avila, G., Buchhave, L., et al. 2014, *AN*, 335, 41
- Thomas, N., & Paczkowski, M. 2021, *JAAVSO*, 49, 12
- Tinetti, G., Drossart, P., Eccleston, P., et al. 2018, *ExA*, 46, 135
- Tokovinin, A., Fischer, D. A., Bonati, M., et al. 2013, *PASP*, 125, 1336
- Torres, G., Fressin, F., Batalha, N. M., et al. 2011, *ApJ*, 727, 24
- Torres, G., Konacki, M., Sasselov, D. D., & Jha, S. 2004, *ApJ*, 614, 979
- Triaud, A. H., Dransfield, G., Kagetani, T., et al. 2023, *MNRAS: Letters*, 525, L98
- Tsai, S.-M., Lee, E. K. H., Powell, D., et al. 2023, *Natur*, 617, 483
- Twicken, J. D., Catanzarite, J. H., Clarke, B. D., et al. 2018, *PASP*, 130, 064502
- Twicken, J. D., Clarke, B. D., Bryson, S. T., et al. 2010, *Proc. SPIE*, 7740, 774023
- Van Der Walt, S., Colbert, S. C., & Varoquaux, G. 2011, *CSE*, 13, 22
- Vogt, S., Allen, Steven, Bigelow, Bruce, Bresee, L., Brown, William, Cantrall, T., Conrad, Albert, et al. 1994, *Proc. SPIE*, 2198, 362
- Wang, J., Jiang, X., Zheng, J., et al. 2023, *RAA*, 24 (3) 15
- Welbanks, L., Madhusudhan, N., Allard, N. F., et al. 2019, *ApJL*, 887, L20
- Wolszczan, A., & Frail, D. A. 1992, *Natur*, 355, 145
- Wordsworth, R., & Kreidberg, L. 2022, *ARA&A*, 60, 159
- Yee, S. W., Petigura, E. A., & Von Braun, K. 2017, *ApJ*, 836, 77
- Yee, S. W., Winn, J. N., Hartman, J. D., et al. 2023, *ApJS*, 265, 1
- Zhou, G., Huang, C. X., Bakos, G. Á., et al. 2019, *AJ*, 158, 141
- Zhou, G., Winn, J. N., Newton, E. R., et al. 2020, *ApJL*, 892, L21